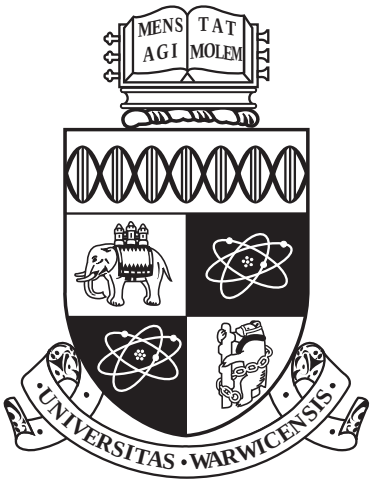

Characterisation and control of the dynamical properties of swimming microorganisms under confinement

by

Matteo Contino

Thesis

Submitted to the University of Warwick

for the degree of

Doctor of Philosophy

Department of physics

August 2017

THE UNIVERSITY OF
WARWICK

Contents

Acknowledgments

I would like to thank my supervisor Marco Polin for his guidance and support, and the others members of the biofluids group, especially Vasily Kantsler, for teaching me how to handle microfluidics and Matthew Turner and Gareth Alexander for advice and useful discussions. I would also like to thanks the collaborators that gave their contributions to the work presented in this thesis: Idan Tuval, Enkeleida Lushi, Emiliano Perez Ipina, and Fernando Peruani. My special thanks goes to my partner Marta and to our families, without whom I would have never been able to make it to the end of my PhD: thanks for all the love and support you have given and continues to give me every day.

Declarations

This Thesis is submitted to the University of Warwick in support of my application for the degree of Doctor of Philosophy. I have read and understood the rules on cheating, plagiarism and appropriate referencing as outlined in my handbook and I declare that the work contained in this assignment is my own. No substantial part of the work submitted here has also been submitted by me in other assessments for this or previous degree courses, and I acknowledge that if this has been done an appropriate reduction in the mark I might otherwise have received will be made. The work presented in this thesis is the product of collaboration with other researchers:

- In chapter 3 the simulation code has been written by Enkeleida Lushi, a researcher at Brown University.
- In chapter 4 the simulation code has been written by Emiliano Perez, a Postdoc at the University of Nice.
- In chapter 5 the simulation code has been written by Idal Tuvan, assistant professor at EMEA.

Work contributing to this thesis has appeared in the peer-reviewed publication:

- M. Contino, E.Lushi,I.Tuval,V.Kantsler,M.Polin. Microalgae Scatter off Solid Surfaces by Hydrodynamic and Contact Forces. *Physical Review Letters*, Volume 115, Issue 25, id.258102. [1]
- R. Jeanneret,M.Contino,M.Polin.A brief introduction to the model microswimmer Chlamydomonas reinhardtii. *The European Physical Journal Special Topics* November 2016, Volume 225, Issue 11âĂŞ12, pp 2141âĂŞ2156. [2]

Abstract

Due to their importance for scientific and technological purposes, interactions between swimming microorganisms and solid boundaries is raising a growing interest in the scientific community but, despite recent efforts, many of their aspects are still unknown. In this thesis we investigate through experiments carried out in PDMS microfluidic devices and simulations the effect that the presence of solid walls produce on the motility of a well known puller-type microswimmer *Chlamydomonas reinhardtii* (CR). We present the study of the scattering of CR against circular pillars in a microfluidic device. Exploiting the curvature of the pillar surface, we are able to determine the contribution of hydrodynamic and contact forces to the scattering interaction. We find that lubrication forces tend to make algae swim parallel to the pillar surface and flagellar contact break this entrapment, making CR to scatter away at a fixed angle determined by the ratio between flagellar and body length independently of their original swimming direction. We also report the existence of random scattering, which, as the name suggests, results in an outgoing trajectory probability uniformly distributed across all possible directions. We find that these interaction rules also apply flat and concave surfaces. Through these results we are able to describe the effect of geometrical confinement in narrow straight channels and circular pools. We find that in channels it is possible to change the cellular transport efficiency simply by varying the distance between channel walls and we discover the existence of an optimal width for the transport of wild type CR. We also describe the escape dynamics of cells from circular pools through narrow apertures; once again we find that the attraction to solid boundaries is essential in describing the results, as cells can find the exit on the perimeter by sliding out of the pools while

swimming along its perimeter.

Chapter 1

Introduction

Charles Darwin, in his 1859 book, "On the origin of Species", define the process of natural selection as "the principle by which each slight variation, if useful is preserved" [3], suggesting that individuals with "useful" traits in a given environment are more likely to survive and reproduce, transmitting them to the next generation. Through this process, the great majority of a population would present such traits after a few generations; due to their fast life cycle and to their long presence on planet Earth, bacteria and other microorganisms became the undisputed champions of survivability and adaptation to their habitat, which can be as challenging as arctic snow[4] or geysers[5] and, under certain condition, they can even survive in outer space [6]. Every microbe is a masterpiece of engineering (and “a nanotechnology dream” [7]) having capacity of moving, implementing search pattern, responding to stimuli and communicating in a body of just few microns. Motility is arguably one of the most striking feature of microorganisms, and allow them to find food [8, 9], colonise protected surfaces [10], and even increase the intake of nutrients by stirring the surrounding fluid [11]. Microswimmers do not live in completely unrestrained fluid, and most of their characteristics must be understood considering the interface with solid or gaseous domain of their habitat, which they exploit to enhance their survivability. One clear example is the formation of biofilms, an aggregation of bacteria adhering to a surface usually contained in a matrix of a polymeric substance[12]; such configuration, among other things, makes bacteria more resistant to environmental threat [13] and allows inter cellular communication through chemical signalling [14, 15]. Despite being favourable to microbial survival, the formation of biofilms can cause severe health issues. Microbial biofilms are more resistant than isolated cells to antimicrobials agents [16, 17], and, when forming on prostethic implants or damaged tissues, are able to resist inside a patient body to repeated antibiotics somministration cycles[18, 19] in a non-viral, quiescent state and, although rarely fatal, they can

persist for months or even years. Another sector where avoiding the formation biofilm is desirable is marine engineering: microbiofouling is the accumulation of algae, bacteria and other microorganisms on submerged surfaces that, in the case of ships' hulls for examples, result in a enhanced drag and reduced fuel efficiency. To prevent biofouling, ship hulls are usually coated with biocides but, with the ban of toxic coatings such as tributyltin (TBT) based paint [20], and copper-based compounds raising concerns about their environmental impact [21] novel methods are required. A novel possibility is represented by the micropatterning of submerged surfaces, where recent experiments [22, 23] showed a decrease in microbial adhesion to biologically inspired microstructures. To design engineered micropatterns the scientific community needs to shed further light on the interaction mechanisms between microorganisms and solid surfaces which, despite their scientific and technological importance, are not yet fully understood. Due to the development of microfluidic technologies, the efforts in the field have dramatically increased, with a vast community of researchers working on the topic. Recent experiments showed that biological and artificial microswimmers can turn microgears [7, 24] or deliver cargoes [25], paving the way for new technological applications. The work presented in this thesis will address some of the open questions in the field of interactions between microswimmers and solid objects, defining the role of hydrodynamics and contact forces in the scattering against surfaces of different geometries, and will explore some possibilities of exploiting the results to control the motility of swimming in microorganisms. The thesis is structured as follows:

- In Chapter 2, we will introduce the basics of low Reynolds number hydrodynamics, briefly describing singularity solutions to the Stokes equation and illustrating the method of images to build a solution to for the flow field in the vicinity of a no slip surface. Later in the chapter we will take an in depth look to microfluidics as the most relevant experimental technique used, and we will present in depth the unicellular green alga *Chlamydomonas reinhardtii*: a microorganism commonly used as a model puller type swimmer in motility and hydrodynamics studies.

- Chapter 3 explores to a fine level of detail, through a large dataset, the first reported experimental study of the interactions between CR and a curved surface, namely a cylindrical shaped obstacle, in a microfluidic circuit.

- In Chapter 4, we we will present and characterise the behaviour of CR in straight narrow channels, showing how confinement highly affects the motility of the algae and presenting new opportunities of controlling microorganismal motility.

- Chapter 5 will present another example of application of the results in Chapter 3,

studying algal motility inside small circular pools and characterising the escape dynamics through narrow apertures on the pool external perimeter.

- In chapter 6, we will present a critical discussion of the work presented in the thesis analysing possible future directions in the field.

Chapter 2

Background and previous works

2.1 Hydrodynamics at low Reynolds number

The flow field $\mathbf{u}$ and pressure p generated by a swimming organism in an incompressible, Newtonian fluid must satisfy the Navier-Stokes equation:

$$\rho\left(\frac{\partial}{\partial t}+\mathbf{u}\cdot\nabla\right)\mathbf{u}=-\mu p+\mu\nabla^2\mathbf{u}+\mathbf{f},\qquad\nabla\cdot\mathbf{u}=0 \tag{2.1}$$

where ρ is the fluid density and μ is the viscosity. By rescaling Eq.2.1 by opportune quantities [26], one obtains the non dimensional Navier-Stokes equations:

$$Re\left(\frac{\partial}{\partial t'}+\mathbf{u}'\cdot\nabla\right)\mathbf{u}'=-\nabla p'+\mu^2\mathbf{u}'+\mathbf{f}',\qquad\nabla\cdot\mathbf{u}'=0 \tag{2.2}$$

where:

$$Re=\frac{\rho UL}{\mu} \tag{2.3}$$

is called the Reynolds number, with U and L being representative values of the flow velocity magnitude and the body size respectively, and represents the ratio between inertial and viscous forces. Typical values of Re for a swimming micro organism ranges between $Re\sim10^{-5}$ for a bacterium to $Re\sim10^{-1}$ for a *Paramecium* [27]. In these cases we can approximate $Re=0$, simplifying Eq.2.1 to:

$$-\nabla p+\mu\nabla^2\mathbf{u}+\mathbf{f}=0\qquad,\nabla\cdot\mathbf{u}=0 \tag{2.4}$$

called the Stokes equation which are linear and time independent. A common approach to solve linear equations is to derive a fundamental solution, also called Green function or impulse response, due to a point force; notice that any derivative of a fundamental solution, is also a solution to the initial equation. In the next section we will present the most common Green functions used in literature as presented in [28, 29].

2.1.1 Flow singularities

Consider a point force acting in $\mathbf{x}'$ of the form $\delta(\mathbf{x}-\mathbf{x}')\mathbf{f}$: the solution to Eq.2.4 for the flow and pressure field generated by such force is called a Stokeslet[30], and is equal to (using [29] notation):

$$\mathbf{u}^{Sto}(\mathbf{r};\mathbf{f}) = \frac{1}{8\pi\mu}\left[\frac{\mathbf{f}}{r} + \frac{(\mathbf{f}\cdot\mathbf{r})\mathbf{r}}{r^3}\right] \qquad p(\mathbf{r})^{Sto} = \frac{\mathbf{r}}{4\pi r^3}\cdot\mathbf{f} \tag{2.5}$$

where $\mathbf{r} = \mathbf{x}-\mathbf{x}'$ and $r = |\mathbf{r}|$. Due to linearity, as mentioned, every derivative of Eq.2.5 is also a solution to the Stokes equations. The first order spatial derivative, obtained through multipole expansion[31], is called a *Stokes Doublet*:

$$\mathbf{u}^{SD}(\mathbf{r};\mathbf{f},\mathbf{g}) = \frac{1}{8\pi\mu}\frac{\mathbf{f}\times\mathbf{g}\times\mathbf{r}}{r^3} + \frac{1}{8\pi\mu}\left[-\frac{\mathbf{f}\cdot\mathbf{g}}{r^3} + 3\frac{(\mathbf{f}\cdot\mathbf{r})(\mathbf{g}\cdot\mathbf{r})\mathbf{r}}{r^5}\right] \tag{2.6}$$

$$p^{SD}(\mathbf{r};\mathbf{f},\mathbf{g}) = \frac{1}{4\pi}\left[-\frac{\mathbf{f}\cdot\mathbf{g}}{r^3} + 3\frac{(\mathbf{f}\cdot\mathbf{r})(\mathbf{g}\cdot\mathbf{r})\mathbf{r}}{r^5}\right], \tag{2.7}$$

where $\mathbf{g}$ is a vector called the dipole moment. Note that the velocity field is a sum of two components: the first one is antisymmetric respect to the inversion of $\mathbf{f}$ and $\mathbf{g}$ and is called a *Rotlet* while the second is symmetric and goes under the name of *Stresslet*.

Another important class of solutions is obtained when we consider a system with no force applied and constant (or null) pressure:

$$\nabla^2\mathbf{u} = \mathbf{0} \tag{2.8}$$

This class of solutions represents the injection of fluid at point $\mathbf{x}'$ with unit rate and has the form:

$$\mathbf{u}^{\mathrm{Sou}}(\mathbf{r}) = \frac{1}{4\pi}\frac{\mathbf{r}}{r^3} \tag{2.9}$$

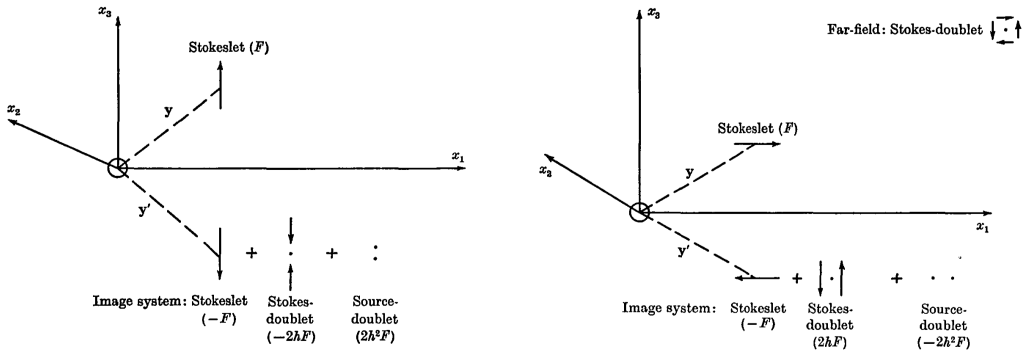

Figure 2.1: Stokeslet perpenicular (left) and parallel (right) to a no slip surface and corresponding image system. Figure adapted from [32].

while its first order derivative, obtained as for Stokes doublet:

$$\mathbf{u}^{\mathrm{Sou}}(\mathbf{r};\mathbf{g}) = \frac{1}{4\pi}\left[-\frac{\mathbf{g}}{r^3} + 3\frac{(\mathbf{g}\cdot\mathbf{r})\mathbf{r}}{r^5}\right] \tag{2.10}$$

is called a *Source Dipole* (doublet) or *Potential Dipole*. It is worth noting the relationship between a source dipole and a Stokeslet:

$$\mathbf{u}^{\mathrm{Sou}}(\mathbf{r};\mathbf{g}) = -\frac{1}{2}\nabla^2\mathbf{u}^{Sto}(\mathbf{x};\mathbf{g}) \tag{2.11}$$

$$p^{\mathrm{Sou}}(\mathbf{r};\mathbf{g}) = -\frac{1}{2}\nabla^2\mathbf{p}^{Sto}(\mathbf{x};\mathbf{g}) = 0 \tag{2.12}$$

as shown in [28].

2.1.2 Stokeslet near a no slip plane

The solutions obtained in the previous sections are valid for an unbounded, infinite viscous fluid which has no equivalent in the real world. In reality, fluids are always found in the presence of a solid or gaseous boundary, which heavily affects the fluid flow created by swimming object. Expressions for confined flow fields have been known since the end of the 19th century [33], but J.R.Blake [32] suggested a method to construct a solution starting from an "image" singularity placed on the other side of the surface as commonly used in the method of images for electrostatic charges near a conducting surface [34]. While in electrostatics there are scalar boundary conditions, in the field of fluid dynamics the no slip conditions forces all components of the velocity vector to be equal to zero on the surface. If we consider a Stokeslet at a point $\mathbf{y}$, at a distance h from the

wall, placing a corresponding singularity at $\mathbf{y}'$ a distance $2h\mathbf{m}$, where $\mathbf{m}$ is the unit vector pointing in a direction perpendicular to the wall, placed at $x_3 = 0$, will only cancel the tangential or normal components of the velocity depending on which direction the original Stokeslet is pointing. A solution that satisfies the no slip boundary condition must be more complex, including additional singularities to the image system. Using Einstein notation, the fluid velocity and pressure value at a point $\mathbf{x}$ [29], can be written as:

$$u_i = \frac{F_j}{8\pi\mu}\left[\left(\frac{\delta_{ij}}{r} + \frac{r_i r_j}{r^3}\right) - \left(\frac{\delta_{ij}}{R} + \frac{R_i R_j}{R^3}\right) + 2h(\delta_{j\alpha}\delta_{\alpha k} - \delta_{j3}\delta_{3k})\frac{\partial}{\partial R_k}\left\{\frac{hR_i}{R^3} - \left(\frac{\delta_{i3}}{R} + \frac{R_i R_3}{R^3}\right)\right\}\right], \tag{2.13}$$

$$p = \frac{F_j}{4\pi}\left[\frac{r_j}{r^3} - \frac{R_j}{R^3} - 2h(\delta_{j\alpha}\delta_{\alpha k} - \delta_{j3}\delta_{3k})\frac{\partial}{\partial R_k}\left\{\frac{R_3}{R^3}\right\}\right]. \tag{2.14}$$

where $\boldsymbol{F}$ is the Stokeslet vector intensity, $\mathbf{r} = \mathbf{x} - \mathbf{y}$ and $\mathbf{R} = \mathbf{x} - \mathbf{y}'$. The first two term are easily recognisable as infinite space Stokeslet while the rest is a combination of a Stokes doublet and a source dipole, as shown in Figure 2.1.

2.1.3 Regularised Stokeslet

Although very convenient analytically, the singularity approach can be problematic to implement numerically. As visible from Eq. 2.5, a Stokeslet is singular in $\mathbf{x}'$, which can complicate the numerical implementation: to avoid complications, an approach that gives a regular flow everywhere has been introduced. First introduced by Cortez [35, 36] in the early 2000s, the method of regularised Stokeslet has been vastly used in numerical simulations of Stokes flows. Conceptually, it consists in obtaining the solution to Eq.2.4 when the force has the form $\mathbf{f}\phi_\epsilon(\mathbf{r})$, where $\phi_\epsilon(\mathbf{r})$ is called a *cut-off function* [36] and is a smooth, radially symmetric function so that $\int_0^\infty \phi_\epsilon(\mathbf{r})dr = 1$. Introducing ϕ_ϵ allow to spread the force over a small area (a blob) where the parameter ϵ controls the area of the spread, so that $\phi_\epsilon \to \delta(\mathbf{r})$ for $\epsilon \to 0$. The mathematical derivation is described in [35, 36, 37]. The regularised Stokeslet given a cut-off function ϕ_ϵ can be written, using Einstein notation, as:

$$S^\epsilon_{kj}(\mathbf{r}) = 8\pi\left[\frac{\partial^2 \mathbf{B}^\epsilon(\mathbf{r})}{\partial x_k \partial x_j} - \delta_{kj}\mathbf{G}^\epsilon(\mathbf{r})\right] \tag{2.15}$$

$$P^\epsilon_j(\mathbf{r}) = 8\pi\frac{\partial G^\epsilon(\mathbf{r})}{\partial x_j}, \tag{2.16}$$

where the functions G^ϵ and B^ϵ are defined so that:

$$\nabla^2 \mathbf{G}^\epsilon(\mathbf{r}) = \phi_\epsilon(\mathbf{r}), \qquad \nabla^2 \mathbf{B}^\epsilon(\mathbf{r}) = \mathbf{G}^\epsilon(\mathbf{r}). \tag{2.17}$$

To build a normalised Stokeslet, usually a cut-off function is selected (examples available in [36]), then $\mathbf{B}^\epsilon$ and $\mathbf{G}^\epsilon$ are calculated and finally the two functions shown in Eq. 2.16 are built. In [37], other fundamental regularised solutions are shown. Since Stokes equations are linear, a solution can be constructed as a linear combination of regularised singularities: in particular, when studying biological fluids in the presence of no-slip surfaces, the method of images can still be used to build the image system of regularised singularities [37].

2.1.4 Microorganisms flow field

Microorganisms swimming is "force free" as the thrust generated by flagella or cilia is steadily balanced by the viscous drag on their body, and their flow field for $r \to \infty$, is well described by a force dipole or stresslet and decays as r^{-2}. The dipole moment $\mathbf{p}$ is usually oriented along the swimming direction $\mathbf{e}$ of the cell and, depending on its sign, we usually distinguish two categories: pusher, when $\mathbf{p} < 0$, and puller when $\mathbf{p} > 0$. This simple picture has been tested experimentally in [39, 38] with excellent agreement to the theoretical prediction: in Figure 2.2 are shown two examples of measured flow field for *Chlamydomonas reinhardtii* and *E. coli* and the comparison with theoretical models. The representation of *Chlamydomonas reinhardtii* flow field as three Stokeslets placed at the body and flagella positions will be used in the simulations discussed in Chapter 3. In [27], the interactions between two microswimmers are analysed; the flow induced by a dipole $\mathbf{p} = p\mathbf{e}$ at distance $\mathbf{r}$ is:

$$\mathbf{u}(\mathbf{r}) = \frac{p}{8\pi\eta r^3}\left[3\cos^2\theta - 1\right]\mathbf{r} \tag{2.18}$$

where θ is the angle between the considered position $\mathbf{r}$ and the dipole direction $\mathbf{e}$. Hydrodynamic interactions between two cells can lead to attraction or repulsion depending on their relative positions and dipole signs. A more interesting (at least in the context of this thesis) effect of the hydrodynamic interactions, is the reorientation due to velocity gradients. To find an expression for the hydrodynamics induced rotation, we must start from the expression for the vorticity field:

$$\omega = \nabla \times \mathbf{u} = \frac{3p}{4\pi\eta}\frac{(\mathbf{e}\cdot\mathbf{r})(\mathbf{e}\times\mathbf{e})}{r^3}. \tag{2.19}$$

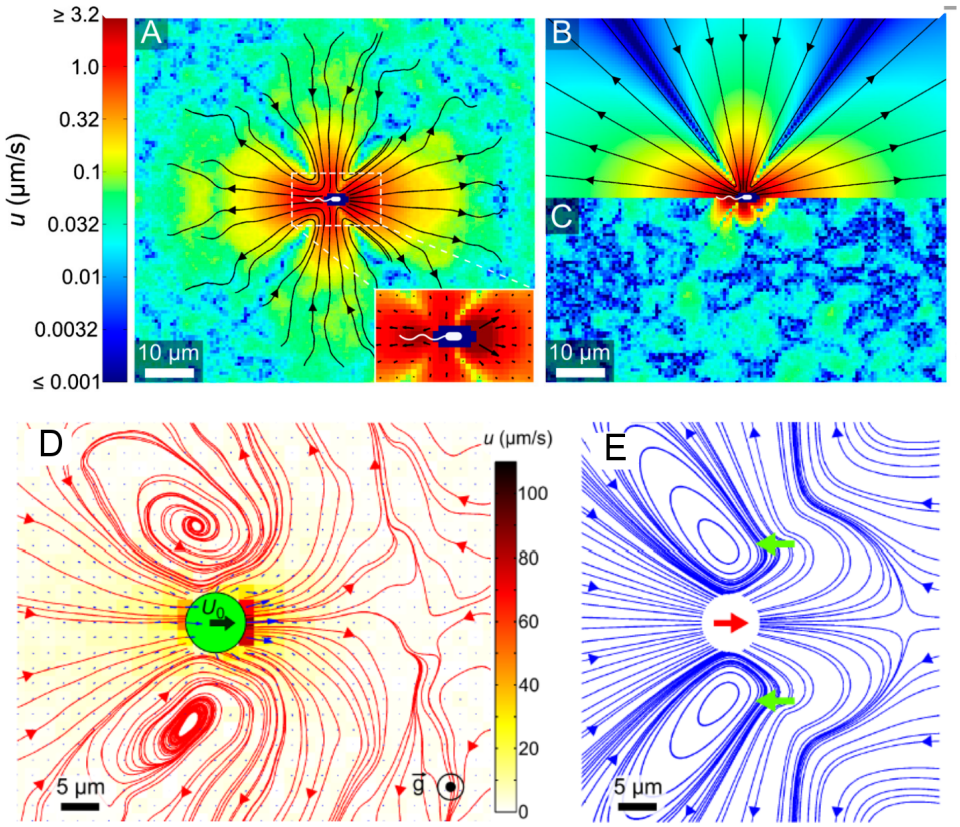

Figure 2.2: Experimentally measured flow fields of a pusher and a puller-type swimmer and comparison with theoretical model. A) Average flow field created by a freely swimming *E. coli*: logarithmic color map indicates the velocity modulus. B) Fit of the measured flow field with a force dipole. C) Difference between measured and theoretically predicted flow field obtained by subtracting the fit results of B) to the experimentally observed flow field shown in A). D) Time and azimuthally averaged flow field created by a freely swimming *Chlamydomonas reinhardtii*. E) Flow field resulting from a three-Stokeslet model (not fitted): red arrow indicates the direction of the singularity placed at the body position, two more Stokeslets of opposite sign are placed approximately at flagellar position. A-C fom [38], D-E from [39].

A cell subject to this field rotates with rate equal to half the vorticity $\Omega = \omega/2$, which sign depends on the sign of $\mathbf{e}$ [27]. As a result, for pullers separated by a distance h and oriented at an angle θ with respect to the distance perpendicular to their separation (see Figure 2.3), the rotation rate is $\Omega \sim -p\theta/\eta h^3$. Two pushers will tend to reorient towards a configuration where they swim parallel while pullers will swim towards or away from each other. As discussed in the previous section, in a leading order approximation, we can suppose that a cell near to a wall is interacting with a phantom mirror cell placed on the other side of the surface. As a result, the equilibrium configuration for a pusher will be swimming at an angle of $\theta = 0$ with respect to the local tangent to the wall, while a puller will swim at an angle $\theta = \pm\pi/2$. In other words, pushers will tend to align and

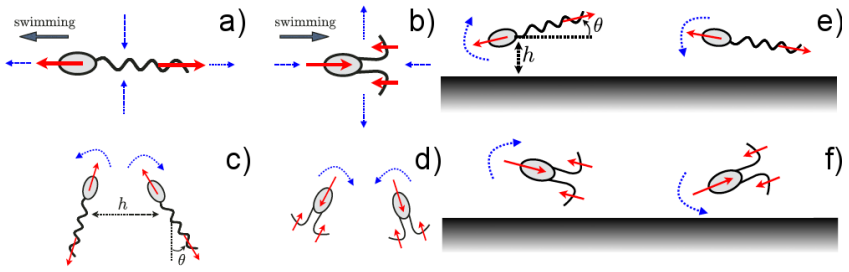

Figure 2.3: Schematic representation of microorganisms' flow field and cell-cell and cell-surface interactions. a,b) Schematic representation of a pusher and puller swimmer. A pusher swimmer, like a *E. coli*, draws fluid from the sides and drives it out from the front and back while a puller swimmer, represented by a *Chlamydomonas reinhardtii*, draws fluid from the front and back and expels it from the sides. c,d) Scheme of cell-cell interaction: blue dotted arrows represents the torque exerted by hydrodynamic forces, the gray dotted line is the distance h between the two swimmers and θ is the angle between the cell swimming direction and a vector perpendicular to h. In case of two pusher swimmers (c), the equilibrium configuration would be two cells swimming parallel to each other ($\theta = 0$ for both cells), while two puller swimmers would be reoriented towards or away from each other ($\theta = \pm\pi/2$) depending on the initial angle between the swimming directions of the cells. e,f) Hydrodynamic interactions between swimmers and solid surfaces: similarly to cell-cell interactions (see text) pushers are steered in a direction parallel to surface tangent ($\theta = 0$) while pullers are reoriented perpendicularly to the wall ($\theta = \pm\pi/2$). Figure modified with permission from [27].

swim parallel to solid surfaces, while pullers will swim head on into them. Since pullers have front mounted flagella (and usually a rather complicated beating pattern), their equilibrium direction will not be stable, leading to an interesting interaction dynamic. The next section will be a brief introduction of microfluidics, an experimental technique vastly used to study the motion of microswimmers.

2.2 Microfluidics

In the words of G. Whitesides, microfluidics "is the science and technology of systems that process or manipulate small (10^{-9} to 10^{-18}) amounts of fluids, using channels with dimensions of tens to hundreds of micrometers"[40]. Although the typical size of a microfluidic channel is indeed in the order of hundreds of microns, it is currently possible to realise features in the order of microns and even nanometers. Microfluidics is the key experimental technique used during the work presented in this thesis: we used the possibilities offered by the technology to realise circuits with complex geometries, which allowed us to gain insights on the interactions between biological microswimmers and solid surfaces. Arguably, the main field of application of microfluidics is the biomedical research where in the last decade the uptake of microfluidic technologies drastically increased largely due to development of soft litography techniques and the use of

poly-dimethilsiloxane (PDMS) [41]: a transparent, biocompatible silicon elastomer that is permeable to air and chemically inert. Thanks to its properties, PDMS devices can be used to image and culture living cells [42, 43]. Building a planar microfluidic device is relatively easy (3D multilayer devices are feasible although more complicated [44]); the procedure is shown in Figure 2.4. The first step towards a microfluidic circuit is the realisation of a mould through standard lithographic techniques: this procedure is usually carried out in a clean room or in a laminar flow cabinet. To fabricate a mould, a silicon wafer previously covered with a uniform layer of photoresistent material (SU8) through spin coating is irradiated with patterned UV light shining through a mask (usually printed on acetate). A chemical agent successively removes the non illuminated parts on the wafer, leaving a replica of the mask pattern on the wafer. The second phase, is the realisation of the actual microfluidic device. A mixture of PDMS and crosslinker is then poured onto the mould and baked for 10 minutes at 75°; once PDMS is hardened, it presents a replica of the mould on its lower face and can be detached from the mould by simply peeling it off. After punching inlet holes on the channels using a biopsy puncher, it can be bonded to a substrate (usually glass or PDMS) through plasma surface treatment, completing the device fabrication. Although microfluidics present numerous advantages, its current usage is mostly restricted to research and, even in the research environment, it requires some degree of expertise not always present in all labs. As a result, the vast majority of papers in the field are a proof of concept (POC) published in engineering journals and aimed at demonstrating that traditional laboratory assays can be performed on microfluidic devices, as shown in [45]. In the next section we present some key studies in microfluidic devices in the field of microswimmer motility which has also been reviewed in [46, 47].

2.2.1 Microfluidics-based studies of microswimmer motility

In this section we will present some examples of experimental works in the field of swimming cell motility in microfluidic circuits. We selected, among the vast literature on the topic, some representative works where the solid boundaries play a crucial role in the description of swimmers' behaviour. We will also introduce some examples of studies where microfluidic devices have been used as model system for porous materials, as closely related to the work presented in this thesis.

Motility and collective motion

Swimming microorganisms represent a perfect model for systems intrinsically out of equilibrium; as such, a bacterial suspension can provide work without an external drive

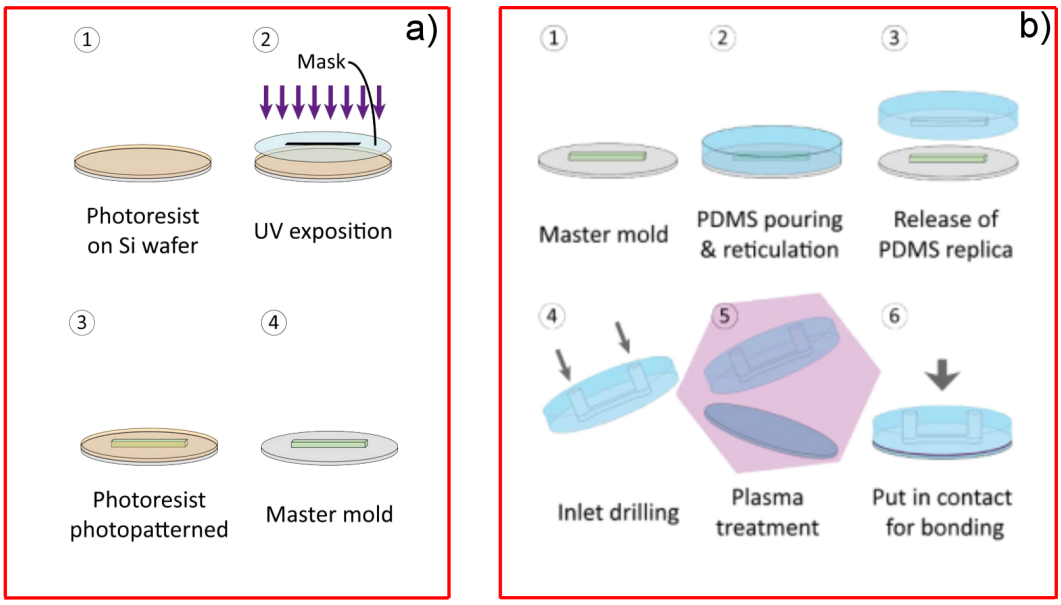

Figure 2.4: Realisation of a microfluidic mould and circuit. a) Procedures to build a microfluidic mould: first, a silicone wafer is coated with a homogenous layer of photoresist. The wafer is illuminated with UV light through a patterned mask; the illuminated area is more resistant to chemicals, so, after chemical etching, the non illuminated pattern is removed, leaving a photoresist mould on the wafer. b) A mixture of PDMS and its crosslinker is poured on top of the photoresist mould; after baking at high temperature (> 75°) the PDMS circuit solidifies, maintaining the mould shape and can be detached from the mould. After punching the inlet holes, both the circuit and a substrate (usually glass or PDMS) are exposed to plasma and subsequently put in contact, so that a covalent bond is formed between the two. The circuit is usually baked for a few more minutes and is finally ready for use. Figure from [48].

or force. Arguably the most famous experimental proof of this concept is presented in [7], where collisions with cells in a bacterial bath are able to continuously rotate a microgear in a version of Feynman ratchet and paddle machine (see Figure 2.5b). The same result has been obtained using artificial swimmers [51]: in this configuration, although the microgear rotation is slower, artificial swimmers are stably found on the microgear edges. This out of equilibrium condition, also suggests that microswimmers can be accumulated on one side of an antisymmetric circuit or trapped inside a properly designed chamber. One of the first experimental examples was made by Galajda et al [49] where they showed it is possible to concentrate *E.coli* on one side of a channel cut in half by a walls of funnels (see Figure 2.5a): the accumulation mechanism is still unclear, but it has been shown that upon interactions with solid surfaces bacteria are reoriented to swim parallel to the obstacle surfaces, leading to a net migration towards the "large" end of the funnel, as shown in Figure 2.5a. The accumulation has been observed even for a puller-type swimmer like *Chlamydomonas reinhardtii* in [52] but the accumula-

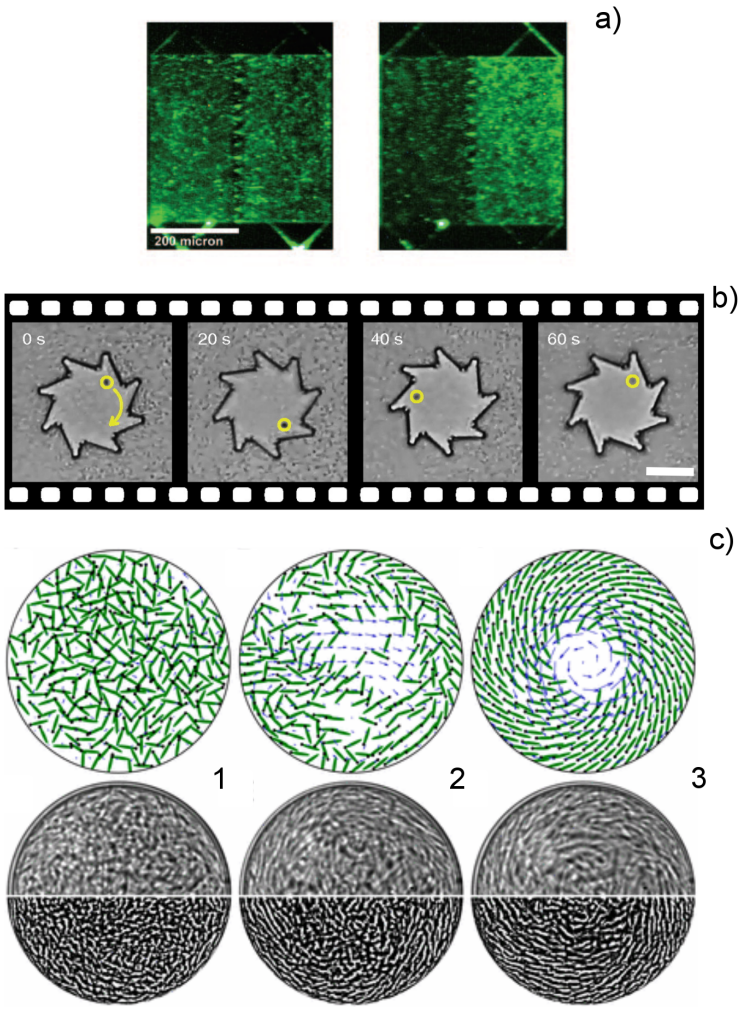

Figure 2.5: Examples of motility study in microfluidics. a) Experimental images from [49]. In a microfluidic device consisting of two chambers separated by a wall of asymmetric funnels, a suspension of fluorescent bacteria (green) is injected. The system evolves from an initial uniform concentration (left) to a net accumulation on the right side of the device (right) at steady state (~ 80min). Figure from [49]. b) Microgear suspended in a dense suspension of *E.coli* completes a revolution around its center in about a minute. Figure from [7] c) Suspension of *B.subtilis* confined in a drop of growth medium, simulations (top) and experiments (bottom). The black dot in simulation figures indicate the direction of swimming of the cells. Starting from 1, where no directional order is noticeable, the suspension develops a stable vortex starting from the boundary (see 2) and develops a stable vortex in 3. At steady state a central vortex rotating clockwise and a boundary layer counter rotating are present. Figure from [50].

tion is much weaker. Others examples of swimmer accumulation through obstacles or specifically designed boundaries are [53] where $E.coli$ cells are accumulated in arrow shaped chambers. Microfluidics also favoured recent development in the understanding of collective motion in microswimmer suspensions. Wioland et al. showed how con-

finement orders the system in a vortex-like state both in circular pools [54] and channels [50] (see Figure 2.5c). Pusher-type swimmers, as mentioned in a previous section, are known to align with solid surfaces and with other swimmers of the same kind. As a consequence, a self reinforcing mechanism that forces cells to swim in circles takes place. The final ordered state consists of a central vortex and a counter rotating layer at the domain boundary. More complicated geometries showed how neighbouring vortices are able to synchronise through hydrodynamics [55]. Alignment among swimmers and with channel boundaries in microfluidic circuits has also been shown to cause artificial micro rotors to self organise in a comet-like flock [56].

Porous materials

In the last decade, researchers exploited the fine geometric control offered by lithographic techniques to create simplified model system of porous environments. In recent years, the locomotion of soil organisms has been studied in microfluidic devices with structured or random dispositions of cylindrical posts to model the porous structure of soil. For example in 2008, Park et al. [57] studied the undulatory locomotion of soil worm *C. elegans* in an agar shallow microstructured microfluidic chamber, with a number of pillars placed in a square lattice (see Figure 2.6d) with different lattice parameters. Surprisingly, they found that when the chamber lattice parameter matched the wavelength of worm oscillation, its velocity increased up to ten times when compared to swimming in an empty circuit; this increase in speed was explained by a combination of swimming and crawling on the circuit lower surface. These results were confirmed by [58], where they observed an increase in *C. elegans* motion efficiency in a saturated granular medium. Two years later, [59] performed the experiments in a PDMS device whose depth did not allow worms to crawl and still observed an increase in moving speed; through a purely mechanical model they were able to relate the increased performance to the use of posts as pivoting points during the swimming oscillation, exploiting the increased drag caused by the presence of posts. The same research group later measured the forces exerted on posts by *C. elegans* [60], confirming their model. These studies proved how soil organisms adapted to their environment, showing a greater locomotion efficiency in a complex medium. *C. elegans* is a complex organism, provided with a brain, and its ability to adapt may not seem surprising, but even at the microscale, in the study of bacterial motility, swimming cells proved to be able to exploit the presence of obstacles. In [61, 62] authors studied the unbiased diffusion of bacteria in random or structured landscape of pillars. In these studies, the authors found that bacteria adhere to obstacles for short length, hopping from one obstacle to the next, as shown in Figure 2.6a. Interestingly, a particle with this kind of behaviour explores the domain far more efficiently

than a billiard particle in the same geometry. A similar behaviour has been observed in [63], where artificial swimmers in a colloidal crystal follow the outer surface of colloidal beads and hop between neighbouring beads' surface. In [64], the authors studied the bacterial diffusivity in random medium with increasing porosity: in this case the diffusivity of bacteria decreases as the obstacle density grows larger. Another interesting phenomenon which has been studied in porous environment is chemotaxis. Microfluidics revolutionised the way chemotaxis was studied, offering the opportunity to create steady, precise gradients of chemical concentrations and the possibility to track single cells from video recordings of the experiments. The earliest example of study of chemotaxis in microfluidics was proposed by Mao et al. [65]: the autors realised a microfluidic circuit where three streams are flowing in parallel. The central stream contained a suspension of bacteria while the two neighbouring streams contained respectively a chemoattractant and a buffer solution; they measured the relative migration of bacteria towards the stream containing the chemicals they were attracted to, proving that the chemotactic sensibility of *E. Coli* was strikingly higher than measured previously (1000 times higher). Another notable advance in the study of chemotaxis is [66], where using particle tracking, the authors reconstructed a chemotactic velocity map of *E. Coli*. In nature, chemotactic microorganisms are usually found in rather complex environments: to see how the surrounding environment affected the chemotactic behaviour of bacteria, [67] used a T-junction channel to inject two streams, one containing bacteria and one containing a chemoattractant, inside a porous-like channel, containing a densely packed hexagonal lattice of circular pillars. They showed that flow enhanced the chemotactic response of the cells in such a complex medium, suggesting that even chemotaxis must be understood in relation to the habitat of cells. To further prove this point, Singh et al. [68] built a dual porosity microfluidic channel for the study of chemotaxis: they first placed a lattice of large pillars in a microfluidic chamber and then placed some smaller pillars inbetween the larger ones in a portion of the channel (see 2.6b) to recreate a low permeability zone. They observed that in a steady gradient, bacteria migrate from high to low permeability zones of the circuit. This result, theoretically predicted by Olson in 2006 [69] may prove useful for bioremediation purposes, where contaminants are likely to accumulate in "clay lenses" (area of low porosity) and are more difficult to be removed through other methods. Finally it is worth mentioning the study of biofilm formation in porous materials. In [70], a nutrient stream has been flowed inside a porous like device where bacterial cells were present (see Figure 2.6c). It has been observed how in this device, the nutrient flow follows preferential paths and biofilms tends to grow in patches: it has also been reported that biofilm patches in contact with the nutrient stream gave a stronger fluorescence signal, indicating a higher respiration rate.

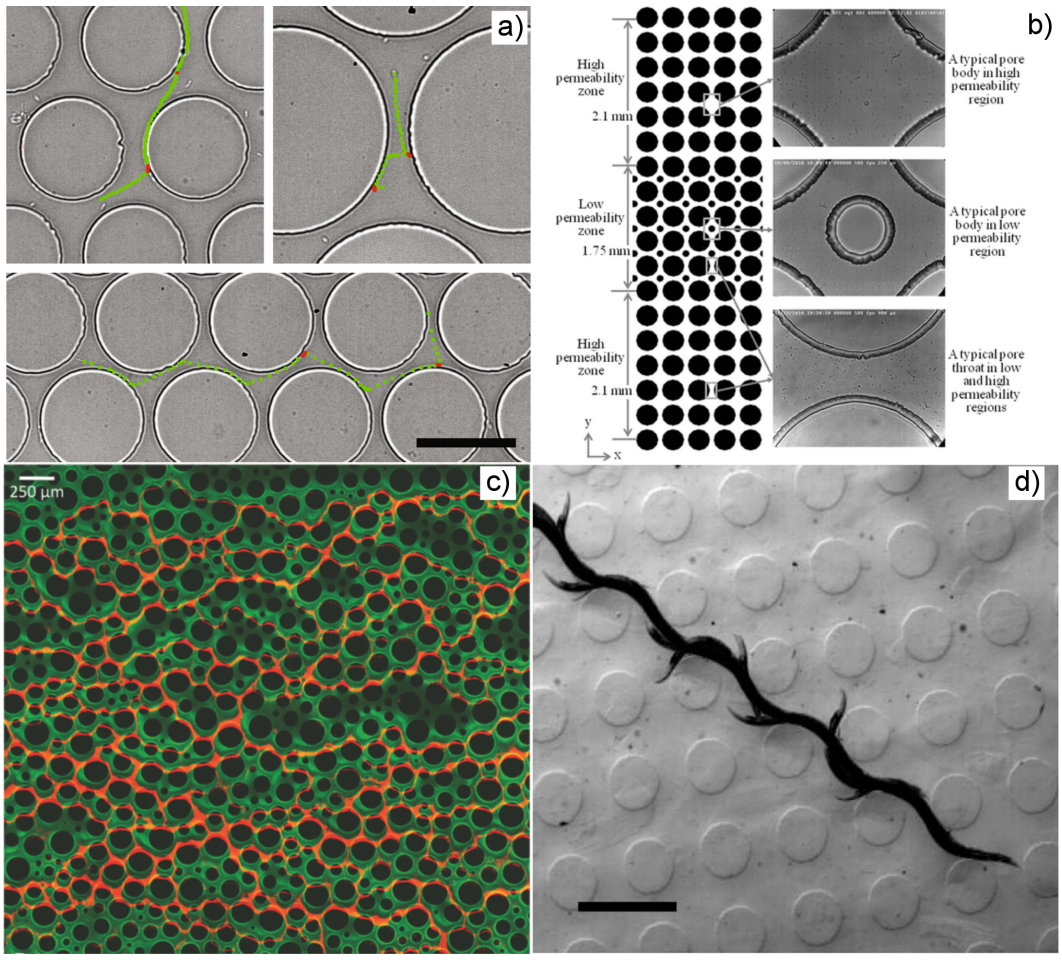

Figure 2.6: Porous media model in microfluidic devices. a) Study of *E.coli* motility in a hexagonal lattice of PDMS pillars that mimics a porous material. Bacteria tend to adhere to surfaces for short length and hop from one post to the next, enhancing their run time. Figure from [62]. b) Microfluidic device with dual porosity to study chemotaxis of *E.coli*. Two high permeability zones, on top and bottom, consisting of a square lattice of circular pillars are separated by an area of low permeability in the middle. The low permeability zone presents the same pillar disposition with the addition of smaller pillars inbetween. Figure from [68] c) Bacterial biofilms (green) in a porous like microfluidic devices consisting of a random disposition of pillars of different sizes where flow of nutrients (red) is present. In certain flow conditions, preferential channels of flow in the biofilm and pillars matrix are observed and biofilm patches in contact with these flow channels emit a brighter fluorescence signal. Figure from [71]. d) Time lapse images of Soil worm *C.elegans* swimming in an agar matrix of pillars. Scale bar is equal to 1 mm. Figure from [57].

2.3 *Chlamydomonas reinhardtii*

Chlamydomonas reinhardtii (who will be referred as CR in the rest of the thesis) order *Volvocales*, family *Chlamydomonadaceae*) is a unicellular green alga which has emerged in the last 60 years as a premier model system within a large variety of areas in molecular

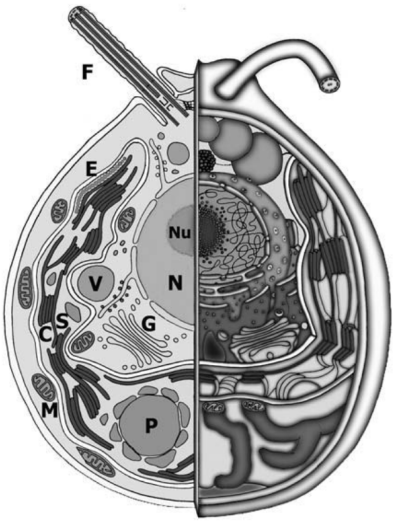

Figure 2.7: Schematic layout of a vegetative *Chlamydomonas* cell. *F*: flagella; *E*: eyespot; *M*: mitochondria; *C*: chloroplast; *S*: stroma; *P*: pyrenoid; *V*: vacuole; *N*: nucleus; *Nu*: nucleolus; *G*: Golgi. (Reprinted with permission from [81].)

and cell biology, including structure and function of eukaryotic flagella, biology of basal bodies/microtubule organising centres, organelle biogenesis [72, 73, 74], photosynthesis [75, 76], cell cycle control [77, 78], and cell-cell recognition [79]. The complete genome has been sequenced relatively recently [80]. There are arguably at least three main reasons leading to this development: i) the relative easy culturing techniques ii) its cell cycle can easily be entrained to the day/night cycle of the diurnal chambers where it is usually grown, offering a very straightforward way to generate macroscopic suspensions of cells whose progression through the cell cycle is synchronised iii) it has proven relatively easy to isolate and characterise mutants.

All this has ushered, in the last ~ 10 years, a new interest for CR on the biophysics front -although "visionary pioneers" were working on it already over 20 years ago [82]. Physicists, mathematicians and engineers have engaged primarily with two areas: photosynthesis and motility. The interest in this organism is testified by the existence of "*The Chlamydomonas Sourcebook*" [81], a detailed 3 volume review of the state-of-the-art knowledge on CR. The species *Chlamydomonas reinhardtii* was first described by Dangeard in 1888, who named it in honour of the Ukranian botanist Ludwig Reinhardt. There are currently three principal strains used for research: the Sager line; the Cambridge line; and the Ebersold/Levine 137c line. The main wild type strains used in the literature, 21 gr, (UTEX 89, UTEX90), (CC124, CC125), come from each of these three lines respectively. They are all supposedly descendant from a single mating pair (*plus* and *minus*,

akin to male and female) derived from the third (c) zygospore in isolate 137 collected by GM Smith in 1945 in a potato field near Amherst, Massachussetts. Figure 2.7 illustrates the basic cellular architecture in CR. The cell body is approximately a 10 μm diameter spheroid, containing all the standard eukaryotic organelles (nucleus/nucleolus, mitochondria, rough and smooth endoplasmic reticulum, Golgi apparatus etc.). The basal 2/3 of the cell are occupied by a single cup-shaped chloroplast, where light capture and photosynthesis happen. The chloroplast contains a single pyrenoid located towards the base of the cell, where CO_2 is fixed, and most of the starch accumulates. This front-back asymmetric architecture causes the centre of mass to be displaced towards the bottom of the cell (bottom-heavy) which causes the cells to have a slight upward swimming bias, through a so-called gravitactic torque [82, 71]. Towards the cellular equator we find the eyespot, a rudimentary light-sensitive organelle that the cell uses to perform phototaxis (motion towards/away from light). The eyespot is composed of two main parts. One is a specialised region of the plasma membrane containing channelrhodopsin, a light-gated ion channel protein with good sensitivity in the $450-700$ nm spectral range. The other is the stigma, a specialised region of the chloroplast containing several stacks of carotenoid-rich granules acting as a dielectric mirror [83]. This mirror has a dual role: it concentrates the light on the rhodopsins when the eyespot is facing the light source; and it screens the rhodopsins when the eyespot is facing away from the light source. This results in a ~ 80-fold increase in the light signal detected by the cell and hence a more accurate motile response to light [84]. The carotenoids also give the eyespot its characteristic bright orange-red colour. Towards the cell apex we find two contractile vacuoles. These organelles are common in freshwater protists, where they regulate intracellular pressure by periodically ejecting excess water that entered the cell by osmosis [81]. In CR they swell (diastole) reaching $\sim 2\,\mu$m diameter, and quickly contract (systole, ~ 0.2 s) with a period of $10-15$ s. The precise mechanism leading to water ejection is unclear [85]. Close to the contractile vacuoles are two basal bodies, from which the two flagellax originate. Basal bodies have a cylindrical shape and are composed of 9 microtubule triplets. They not only act as flagellar bases, but during cell division double up as centrioles. As such they are essential organelles. The two basal bodies are directly connected by the distal striated fibre, containing the contractile protein centrin. Additional fibres (rhizoplast), also centrin-based, connect basal bodies to the nucleus. There is evidence that centrin-based fibres can contract *in vivo* in response to changes of Ca^{2+} concentration in the cell [86]. Changing the tension of the distal striated fibre might have an impact on flagellar dynamics and synchronisation (personal opinion) but the link has never been studied. Additional sets of fibres connect the basal bodies to four microtubule rootlets, which extend deep within the cell body and are responsible for a precise and reproducible ar-

rangement of cellular organelles (e.g. the correct orientation of the eyespot relative to the flagellar plane, which is essential for phototaxis) (see also [81], Vol. 3, Ch. 2). CR cell body is enclosed in a $\sim 200\,\text{nm}$-thick cell-wall composed of 7 distinct layers consisting primarily of glycoproteins, with no trace of cellulose. The ultrastructure of the wall is well characterised, but its synthesis and assembly is not understood as well. From each basal body a single flagellum extends outwards for $\sim 10-12\,\mu\text{m}$. The flagella are motile and usually beat in a characteristic breaststroke fashion at $\sim 50\,\text{Hz}$. These will be described in more detail in the next section. Vegetative *Chlamydomonas* cells are haploid (i.e. the nucleus contains the same number of gene copies as that of a gamete: 1 copy of each gene), and can reproduce indefinitely in this state. This asexual reproduction has a cycle of approximately one day, and can be entrained to be exactly one day if the cells are grown within a diurnal chamber set to a day/night cycle of 24hr. This is (necessarily) a clonal reproduction, whereby the mother cell undergoes n subsequent cell divisions during the night, producing 2^n daughter cells. These then hatch from the mother and the cycle repeats. The number of divisions n depends on the cellular volume reached by the mother cell as it commits to cell division (size checkpoints),usually it is at most 3 (i.e. 8 daughter cells). This fascinating process, including the control possibilities afforded by light, has been studied extensively (see also [81], Vol. 1, Ch. 2). CR can also undergo sexual reproduction, whereby a pair of cells of opposite mating types (*plus* and *minus*) fuse together to form a temporary quadriflagellate zygote (diploid) which remains motile for $\sim 2\,\text{hr}$ and then forms a zygospore with a tough external wall. In this state the cell has available proteins from each of the two original haploid cells, and thus mutations carried by only one of these can be recovered in the zygote by the proteins of the other. Upon maturation (only a few days under lab conditions) the zygospore germinates and gives rise to four vegetative cells by meiosis. These can be separated manually using a standard cell biology technique called tetrad dissection, and the subsequent progeny from the asexual reproduction of each of the four cells can be picked and cultured independently. This is a powerful and quite straightforward technique to combine genes from different strains.

Plus and *minus* cells can only mate after becoming competent for sexual reproduction. The process is called gametogenesis, and in the lab it can be induced easily by moving the cells to a medium without N-sources. The cells will then generally undergo a final round of cell division and then become gametes: they swim well and do not grow and divide. In principle, this produces a population of cells with very uniform properties, and in fact it has been used in several occasions in the past to study CR motility. Gametes' properties should remain constant for several days, but eventually they will die unless they mate or N is added back to the medium (in which case they revert to the

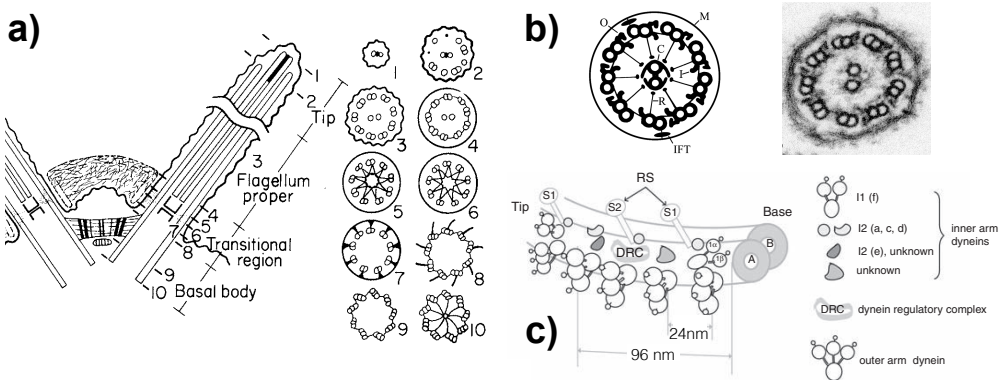

Figure 2.8: *Chlamydomonas* flagellar schematics. a) Spatial organisation of basal bodies, transition region and axoneme proper. Notice the drawing of the striated fibers connecting the basal bodies. b) Schematics and electron micrograph of axonemal cross section. *O*: outer dynein arms; *I*: inner dynein arms; *C*: central pair; *R*: radial spokes; *M*: flagellar membrane; IFT: IFT trains. Notice the microtubule doublet (# 1) without the central pair. c) Closeup of the basic 96 nm repeat unit on the outer doublets. *RS*: radial spokes (*S*1 and *S*2). (a,c) from [81]; b) from [87])

vegetative state).

Cells grow easily at a temperature of $20° - 24°$C and under "white" illumination of $\sim 100\,\mu$E/m^{2}s (1E = 1 mole of photons). The medium can be completely inorganic, forcing phototrophic growth (i.e. they need to photosynthesise to survive) or it can have acetate as organic carbon source. The latter is called myxotrophic growth and it is much faster (larger n on average), but cell synchronisation is non ideal.

2.3.1 The flagellar apparatus

The two front flagella are arguably the most evident organelles in *Chlamydomonas* (see Fig. 2.8a). These are remarkably complex structures, composed by more than 500 different *types* of proteins [87]. Flagella are used not just for motility but also for sensing (chemical and mechanical) and mating. An astounding amount of work has poured into understanding CR flagella both at the molecular and dynamical levels, especially after it was discovered that much has been conserved throughout evolution and as a result several human ciliopathies can be studied successfully in CR [88]. *Chlamydomonas* flagella are slender, whip-like objects $\sim 12\,\mu$m long and $\sim 0.25\,\mu$m thick, which exit the cell wall through specialised regions known as "flagellar collars" (see [81] Vol. 1, Ch. 2). They are completely enclosed by the flagellar membrane, a domain of the cell's plasma membrane whose composition is highly regulated also by a diffusion barrier at the flagellar base (possibly realised by two structures known as the flagellar "necklace" and "bracelet"). This membrane domain contains, among others, several types of voltage-gated and mechanosensitive ion channels involved in phototaxis and perception of mechanical stimuli. Ap-

proximately 16 nm outside the flagellar membrane there is an extra "fuzzy" layer termed glycocalyx, a seemingly compact layer of carbohydrates connected to the most abundant flagellar membrane protein (FMG-1B). Two opposite rows of 0.9 μm-long, 16 nm-thick flexible filaments spaced 20 nm apart, protrude from the distal 2/3 of the flagellum. These so-called mastigonemes are exclusively found on the flagella of protists, where they are thought to increase hydrodynamic drag. It is not clear whether mastigonemes are anchored just to the flagellar membrane or directly to the internal scaffold. They are completely replaced every $\sim$ 4 hr. This is also the estimated turnover time for the flagellar membrane, which is continuously shed from the flagellar tip through ectosomes possibly involved in cell-cell signalling [89].

The core structure within the flagellum is the axoneme, which is based on the standard 9+2 configuration: 9 microtubule doublets surrounding a central pair. The doublets, composed of microtubules A and B (13 and 11 protofilaments respectively) stem directly from the basal body triplets mentioned earlier, through a characteristic transition region (Fig. 2.8a) displaying a "stellate" structure (sections 5,6 in Fig. 2.8a) typical of algae and sperm cells of land plants (e.g. ferns), but absent in protozoa or animals. Along the flagellum proper, the doublets are linked by nexins, $\sim$ 40 nm-long polymers of a currently unknown protein. Notice that nexins are longer than the shortest distance between adjacent doublets ($\sim$ 30 nm in straight axonemes). The central pair of microtubules is not connected to the basal body. It nucleates within the transition region just above the stellate structure, which is thought to prevent the pair from sliding into the basal body itself. The two microtubules of the central pair are held together by bridges, and host a variety of proteins likely involved in flagellar metabolism, as well as kinesin motor proteins of unknown function. Along the portion of the central pair within the flagellum proper (see Fig. 2.8a), projections emerge at regular intervals based on (multiples of) a basic unit length of 16 nm. The projections interact with the head processes of the radial spokes, 30 nm-long rod-like structures attached to the A-tubules and extending towards the central pair. There is strong evidence that this interaction is a key component in regulating the generation of bending moments within the axoneme (see below). The central pair is spontaneously twisted, a characteristic *not* shared by animals, making a left-handed helix with $\sim$ 2 full turns along its length, and rotates during flagellar motion being driven by bend propagation along the axoneme [90]. All axonemal microtubules are identically oriented with their plus-end towards the distal portion of the flagellum. While the central pair terminates precisely at the flagellar tip, the outer microtubules end $\sim$ 0.5 μm earlier, first with the B and then the A tubules (sections 1,2 in Fig. 2.8a). The central pair and the A-microtubules terminate with different capping structures, all of which include plugs entering directly into the microtubule's lumen. The caps' function(s) is

still unclear. Altogether, these passive components make for a pretty stiff axoneme, with an estimated bending rigidity $\kappa \simeq 4 \times 10^{-22}\,\mathrm{N\,m^2}$ [91], which translates to a persistence length $\kappa/k_BT \sim 10^5\,\mu$m ($\sim 10^4\times$ flagellar length). The bending moments leading to flagellar motion are generated by axonemal dyneins, which localise on the A-microtubules and extend towards the B-microtubule of the nearest doublet (Fig. 2.8b). They are organised in two rows, the outer and inner dynein arms ("oda" and "ida"), depending on their position along the radius of the axoneme. Oda's and ida's are structurally different dyneins. They are organised following the basic axonemal 96 nm repeat unit (Fig. 2.8c). This comprises 4 oda's, 24 nm apart, in the outer section; while in the inner section we have: a variety of ida's not yet completely characterised; two radial spokes; one dynein regulatory complex (DRC) which localises at the base radial spoke 2, plus several other regulatory proteins (mainly protein kinases and phosphatases). Linker proteins provide a direct physical connection between neighbouring oda's, between oda's and ida's, and between oda's and the DRC. This is a complex machine! One of the outer doublets lacks oda's: this is doublet 1 (Fig. 2.8b). The other doublets are numbered following the direction in which the dyneins extend. CR flagella are oriented with their doublets #1 facing each other, and beat almost exactly along a plane determined by doublets 1, 5, and 6.

The process leading to microtubule bending is reasonably well understood [92]: dyneins bridge between neighbouring doublets and use ATP hydrolysis to generate an inter-doublet sliding force which is converted to bending by the presence of geometric constraints to relative sliding of doublets (nexin links and basal body are the main suspects here). However, we currently do not have a clear understanding of either the basic mechanism leading to active oscillations (i.e. how do you alternate the bending direction?) or how such basic oscillation is then refined to give the observed waveforms. A solid body of experimental evidence shows that in *Chlamydomonas* the latter is achieved through active regulation of dynein activity by at least DRC and ida I1, which in turn are regulated by phosphorylation/dephosphorylation under the control of radial spokes/central pair. This active regulation adds a level of complexity which I believe will not be easy to model convincingly. In this context, high quality experimental characterisation of flagellar dynamics in CR will certainly be very useful. Experimental investigations based on analysis of flagellar dynamics in CR date back at least to the mid 80's [93], and have been recently refined by (semi)automated methods [94, 95, 96]. They have provided tests for microhydrodynamics of cell locomotion (slender body vs. resistive force theory), achieved direct measurements of bend propagation along the axoneme, and characterised differences between wild type, *ida* and *oda* mutants. Comparing wild type and mutants' flagellar dynamics and swimming behaviour [97] revealed that ida's and oda's contribute differently to flagellar beating. Oda's provide most of the internal power,

while ida's are mostly responsible for the establishment of the correct waveform. As a consequence, *oda* mutants mostly have an altered waveform but close to normal beating frequency ($\sim 50\,\mathrm{Hz}$), while *ida* mutants have close to normal waveform but altered beating frequency ($\sim 20\,\mathrm{Hz}$). The basic mechanism leading to flagellar oscillations is still not completely understood. Currently, there are three alternative hypotheses [92, 98]: geometric clutch (GC), curvature control, and sliding control. These differ in the way dynein activity is periodically inhibited on opposite sides of the axoneme, a necessary condition for the emergence of oscillations. Ultrastructural analysis of quickly-frozen beating flagella in CR [99] shows that when axonemes bend their cross section along the bending plane expands by $\sim 25\%$. This observation would support the geometric clutch idea of oscillations caused by dyneins detachment induced by diverging transversal stresses within the axoneme. More recently the analysis of the most unstable beating modes in the three models also supported GC as a plausible basic mechanism for flagellar oscillation [98]. However, despite some evidence in support for GC, no definitive consensus has emerged yet.

2.3.2 Flagellar motility

CR flagella follow mostly a so-called "ciliary" type of beating, with bending waves which propagate along the axonemes [95, 96] and cause the continuous alternation of well defined power and recovery strokes. A characteristic feature of this dynamics is the pronounced synchrony of the two flagella, which usually phase lock for seconds on end, although the exact average duration depends strongly on flagellar length [100]. This is most often "in-phase" locking, but the phototaxis mutant *ptx1* was recently shown to display also extended periods of anti-phase synchronisation, which are however associated with a slightly different waveform [101]. It is not known whether there is a causal connection between the type of phase-locking and flagellar waveform.

What causes phase locking? In the last few years, this problem has stimulated quite a lot of work, both experimental and theoretical. Experimental investigations have been based mainly on long-time high-speed recordings of flagellar motion in pipette-held cells [100, 101, 102]. Following the lead of pioneering studies by U. Rüffer and W. Nultsch in the mid 80's [93], these studies have revealed that normal phase synchrony is noisy, and that noise can occasionally lead to phase slips: brief lapses of synchrony lasting a few beats ($\lesssim 100\,\mathrm{ms}$) whereby one flagellum accumulates one or more full extra cycles with respect to the other. Either flagellum can slip ahead, although the probability is usually biased to a cell-dependent-degree towards a specific flagellum. These observations can be recapitulated very well using a simple effective model, where the flagellar difference $\Delta(t)$ evolves according to $\dot{\Delta}(t) = \delta\nu - 2\pi\epsilon\sin(2\pi\Delta) + \xi(t)$. Here $\delta\nu$ is

the intrinsic frequency difference between the flagella (responsible for the slip bias), ϵ is their effective coupling, and ξ is an effective noise term responsible for the slips. For $|\delta\nu| < 2\pi\epsilon$ the system has two fixed points, one stable and one unstable, the stable one representing the observed state of phase locking. This stochastic Adler equation can actually be derived as the first order description of the generic dynamics of weakly coupled self sustained phase oscillators [103], so in a sense it is not completely surprising to find it here. However, different coupling mechanisms will produce ϵ's of different magnitude and which depend differently on parameters of the system, and so experiments that change ϵ can in principle be used to determine what is the origin of the observed coupling. Two main models have been proposed: 1) the coupling comes from the interplay between direct hydrodynamic interaction and elasticity intrinsic in the waveform [91]; 2) the coupling results from modulations of flagellar driving force within a beating cycle [104]. Although the relative strength of coupling from these two effects can in fact be tuned within colloidal systems of rotors [105], experimental tests with either CR [100] or the related species *Volvox carteri* [106] support quite clearly an elasto-hydrodynamic origin for the synchronisation observed. An alternative model based on cell-body rocking has been proposed by B. Friedrich and coworkers [107], and we refer the reader to his lecture notes for more information. Still, the observation of prolonged alternate periods of both in-phase and anti-phase synchronisation in *ptx1* poses new challenges to our understanding of flagellar synchronisation, currently not solved. The key to understanding the problem will come perhaps from experiments specifically characterising flagellar beating noise [108]. Besides normal flagellar movement, *Chlamydomonas* can also display a characteristic "shock" response, where the flagella undulate in front of the cell in a "flagellar" type motion (snake-like). This shock lasts $\sim 500\,\mathrm{ms}$, and is triggered by a massive Ca^{2+} influx within the flagellum [109] in response to intense stimuli. Interestingly, during shock dynamics flagella hop between periods of in-phase and anti-phase synchronisation, but this aspect has not been studied in detail yet. Hydrodynamic models of flagellar waveforms suggest a reason for evolving a separate shock response: this seems to be optimised for fast escape, while normal beating is optimised for feeding [110]. However, during shock response the cell does slow down noticeably ($20\,\mu\mathrm{m/s}$ vs. $100\,\mu\mathrm{m/s}$), so the connection with a more efficient escape is not immediately clear.

Swimming is not only the way CR can move: looking under the microscope at a drop of *Chlamydomonas* culture deposited on a coverslip, it is common to see at the bottom surface many cells with their flagella spread wide apart and not beating. What is perhaps a bit more unexpected is that these cells, whose flagella adhere to the coverslip, move. This movement is called gliding. During gliding the cells slide at $\sim 1.5\,\mu\mathrm{m/s}$ [111] with the leading flagellum in front determining the direction of motion, and the

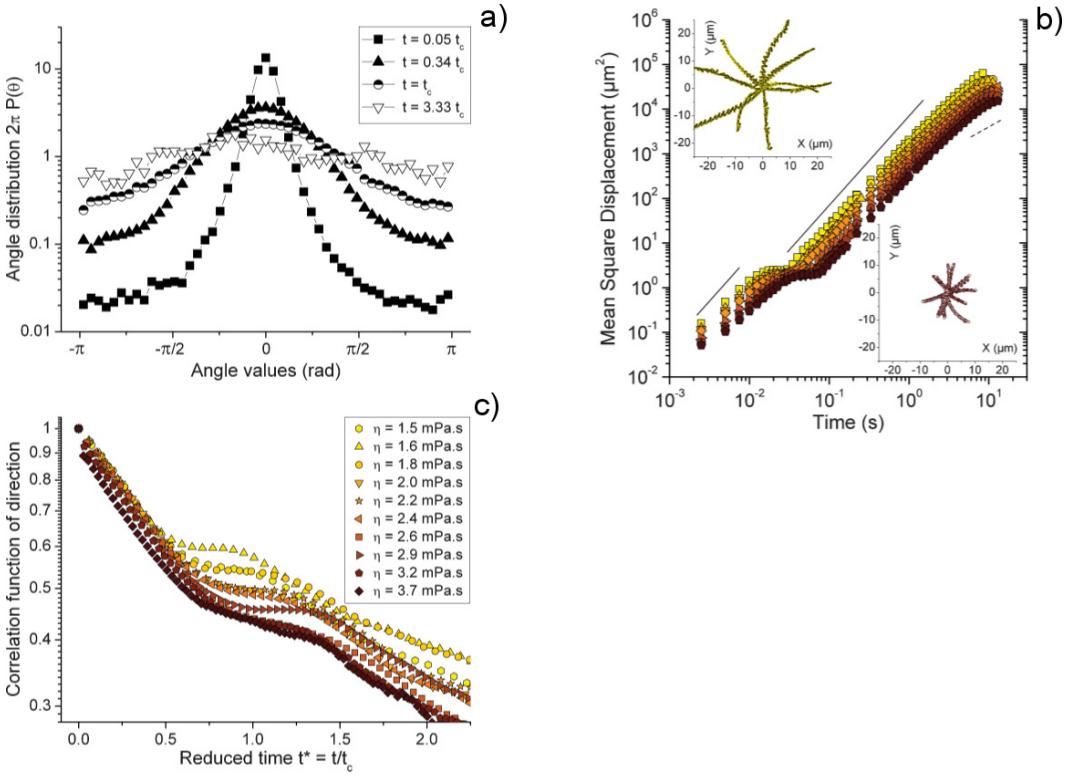

Figure 2.9: Characterisation of CR motion in media of different viscosities. a) Distribution probability of the deviation angle θ, defined as the angle between the istantaneous swimming direction $\mathbf{k}(t)$ and $\mathbf{k}(t+t_0)$. b) Mean square displacement $< r^2(t) >$ for different medium viscosities. Continuous lines have slope $m = 1$, dotted line has $m = 2$. Insets show examples of trajectories starting in the axes origin and lasting 0.5 s in media of different viscosity. Top right corner medium viscosity is equal to $\eta = 1.5\mathrm{m}/,\mathrm{Pa}/,\mathrm{s}$, the bottom left $\eta = 1.5\mathrm{m}/,\mathrm{Pa}/,\mathrm{s}$. For symbols legend see c). c) Swimming direction correlation function in media of different viscosities. Figure adapted from [113].

other one trailing behind. The movement typically stops after a few seconds and when it resumes both flagella have the same probability to be the new leader. The mechanism leading to this very peculiar kind of movement, which might have evolved before the actual axonemal beating [111], has only recently been demonstrated [111, 112] and it is related to a seemingly completely disconnected phenomenon: the growth and maintenance of eukaryotic flagella.

2.3.3 Motility of *Chlamydomonas reinhardtii*

The first microscopic high speed study of CR motility dates back to the early 80's [114, 115], a laser scattering technique called Dynamic Light Scattering (DLS) is used in order to obtain the cell velocity distribution of a suspension of algae inside an observation cell. Several years later Hill and al. [116], used a microscopy based tracking system to

study the trajectories of algae with and without a phototactic stimulus. A few years later, Vladimirov et al. used a laser based tracking technique to measure the distribution of velocities [117] and the gyrotactic coefficient [118] of *Chlamydomonas nivalis* (a closely related species) in a measurement cylinder. The velocities of cells and the period of the helical path of CR were also measured using dynamic differential microscopy [119] and video cell tracking both in 2D [113] and 3D [120]. CR are reported to swim at velocities in the range $84-100\,\mu$m/s along a tight left-handed helix, caused by small chiral tilts in the waveforms of its flagella. The spinning frequency is ~ 2 Hz, with a resulting pitch of $\sim 50\,\mu$m. For a detailed mathematical description of helical swimming see [121]. However, the helix is clearly not perfectly straight. Active flagellar noise (e.g. phase slips, but the actual origin has not been explicitly investigated experimentally) causes a small amount of angular diffusion D_{rot}, which has been measured explicitly for *C. nivalis* to be $D_{rot} \simeq 2\,\mathrm{rad}^2/\mathrm{s}$ [116]. By itself, this would cause a spatial diffusivity $D \simeq 0.25\times10^{-4}\,\mathrm{cm}^2/\mathrm{s}$ [122]. This is significantly smaller than the value $D \simeq 7\times10^{-4}\,\mathrm{cm}^2/\mathrm{s}$ which has been measured directly on a population of *C. reinhardtii* [123]. The discrepancy is due to the fact that the effective angular diffusion is not the main mechanism leading to CR spatial diffusion. Instead, diffusion is dominated by sharp reorientations which happen randomly following a Poissonian dynamics with characteristic time ~ 10 s. These sharp turns are due to ~ 2 s intervals during which CR flagella lose synchrony and beat at a constant but $\sim 30\%$-different frequency. This is probably due to a substantial increase of their intrinsic frequency difference [123] rather than a weakening of interflagellar coupling, possibly caused by changes in cytosolic Ca^{2+} concentration. The resulting motion is a persistent random walk, whose mean square displacement has the form:

$$< \Delta x^2(t) >= 2v^2\tau_p\left[t-\tau_p\left(1-e^{\frac{t}{\tau_p}}\right)\right] \tag{2.20}$$

where v is the cell velocity and τ_p is called the persistence time. It is easy to show how 2.20 is $\propto t^2$ for $t \ll \tau_p$ and $\propto t$ for $t \gg \tau_p$. In [119] CR are reported to swim in straight lines for $\sim 100\,\mu$m, slightly longer than one second, while Polin [123] and Garcia [113] give an estimate of ballistic time around 10s (see Figure 2.9), ten times larger. When subject to stimuli, the motion of CR resembles a persistent random walk with bias in one direction; we will discuss some examples in the next section.

Directed motion

In this section we will briefly discuss the capacity of CR to move along a fixed direction because of gravity or in reaction to chemical gradients or light stimuli. We have already mentioned how CR swim along a helical path scanning the environment with its eye-

spot placed on one side of the body cell. When swimming within a light field, the light hitting the eyespot produces a temporally modulated signal in all cases where the cell is swimming at an angle different from 0 (positive phototaxis) or π (negative phototaxis) with respect to the direction of light propagation: in this case the light intensity on the eyespot is constant [124]. Incident light, causes a Ca^{2+} ion current towards the flagella [125, 126, 127]: this current increases cis-flagellum and decreases the trans-flagellum beating amplitude [128]. Depending on the calcium ion current, CR can swim away or towards the light source [124]. Although the mechanism underlying the steering is understood, why the switch between positive and negative phototaxis happens is still unclear; recently [129] showed how long exposure to light cause CR to switch between the two regimes. Another factor that is known to affect CR swimming behaviour is gravity. The weight distribution of CR is not uniform along the cell body, with the centre of mass being shifted towards the rear (opposite to flagella) part of the cell, so that CR are commonly said to be "bottom heavy". As a result, the average swimming direction is directed upward. This mechanism is called *gravitaxis* (or negative-geotaxis)[130, 131], while the interplay between viscous drag and gravitational torque has been referred to as gyrotaxis [132], and causes algae to swim towards downwelling region of the fluid. The first effect creates a gradient of concentration, caused by the higher presence of CR in the upper region of the fluid and a less dense lower region of fluid with fewer or no cells. When the concentration difference is sufficiently large, convection flows are triggered and we observe "bioconvection" patterns [133, 134], with the formation of downwelling plumes. A continuous model has been proposed to describe the formation of this pattern [135, 136] while Pedley and Hill analysed the stability of an algal suspension [137]. Finally it has been shown that CR perform chemotaxis and accumulate towards a higher concentration of ammonium ions NH_4^+ [138, 139, 140]; the chemotactic behaviour is lost during gametogenesis, that can be triggered by a N depleted medium [141].

Chapter 3

Scattering of *Chlamydomonas reinhardtii* from curved surfaces

3.1 Introduction

From biofilm formation within soil's porous structure [70], to protistan parasites navigating through the densely packed blood of the host [142], and mammalian ova fertilisation [143], solid boundaries alter both motion and spatial distribution of microorganisms [49, 52] in ways that are currently not well understood [144, 145]. Explaining these interactions can pave the way for the use of extant microorganisms in technological applications ranging from bioremediation [146, 147], and artificial insemination [148], to directed transport and delivery of pharmacological cargo at the microscale [149], as well as inform the design of artificial microswimmers [150]. One of the most basic types of interaction is the scattering off a solid plane. Bacteria and other microswimmers with rear-mounted flagella ("pusher"-type) are well known to accumulate spontaneously on planar surfaces [151], a phenomenon that has been equally well explained by theories based on either purely steric [145] or hydrodynamic [144] interactions. New experiments are finally prising these two effects apart, with results in clear support of the latter [152, 153]. Our knowledge of cell-wall interaction for the other major class of microswimmers, those with front-mounted flagella ("puller"-type), is distinctly less advanced. Recent experiments suggest that steric effects dominate the scattering of these flagellates off flat boundaries [52]. If true in general, this would place the two microswimmer types in clearly separated categories of interaction. However, similarly to the bacterial case [153], differentiating steric and hydrodynamic effects requires one to move beyond a plane wall. Here we report the first detailed experimental study of the scattering of a model puller-type microswimmer, the biflagellate alga *Chlamydomonas reinhardtii* (CR)

[154], off a curved surface. Our results, supported also by numerical simulations, show that both hydrodynamic and steric forces are needed to explain the microswimmer's interaction with obstacles. At close contact, lubrication forces alone can lead to long-term entrapment, which is avoided through direct flagellar action following cell spinning. This might confer an advantage to organisms that, like *Chlamydomonas*, need to navigate through heterogeneous media.

3.2 Experimental setup

3.2.1 Materials and methods

We describe here the microfluidic devices passivation and cell growth protocol, as well as the instrumentation that will be used to perform all experimental work reported in this thesis: where changes to these protocol are present, they will be reported in the materials and methods section of the corresponding chapter. We build "quasi 2D" (whose thickness $t = 30\mu m$, measured using an optical profilometer, is comparable to CR cell diameter $2a \sim 10\,\mu m$) PDMS devices cast from SU8 master mould produced with standard soft litography techniques [41]. Each device contains a region where 12.5 μm cylindrical pillars extending from top to bottom are arranged in either hexagonal or slightly randomised square lattices of spacing 75 μm between the pillar centres; these regions are $4.5 \times 4.5\text{mm}^2$ big in the case of a random lattice and $3 \times 2.6\text{mm}^2$ for hexagonal arrangement. We find that results are identical in both arrangements for any measured experimental observable. This is also the case for the probability distributions of incoming angle, that we show in Figure 3.2a for both lattices: distributions are almost identical, but differ from the distribution arising from an isolated pillar, with the greatest discrepancy in the $0^\circ < \theta_{in} < 20^\circ$ region. The inside surfaces of the channels were passivated by injecting a syringe filtered 0.1% w/w solution of bovine serum albumine (BSA) in water to completely fill the channel; the solution was left inside the channel for 30 minutes before washing it using fresh culture medium and cells were subsequently injected inside the device: the BSA concentration used in experiments has not been optimised but we did not record any sign of CR sticking either to glass or PDMS in devices where this passivation protocol was used. It is worth advising the interested reader that BSA stock solution must be kept refrigerated and diluted in small aliquotes prior to use: this procedure prevents bacterial growth in the BSA which, when very severe contaminations are present, may cause the loss of the solution's passivating effect. *Chlamydomonas reinhardtii* (CR) strains CC125 and SHF1 (short flagella mutant,) were grown axenically in Tris-Acetate-Phosphate medium at 21°C under continuous fluorescent illumination (100 μE/m^{2}s, OSRAM Fluora). Cells from exponentially growing cultures at $\sim 5 \times 10^6$cells/ml were har-

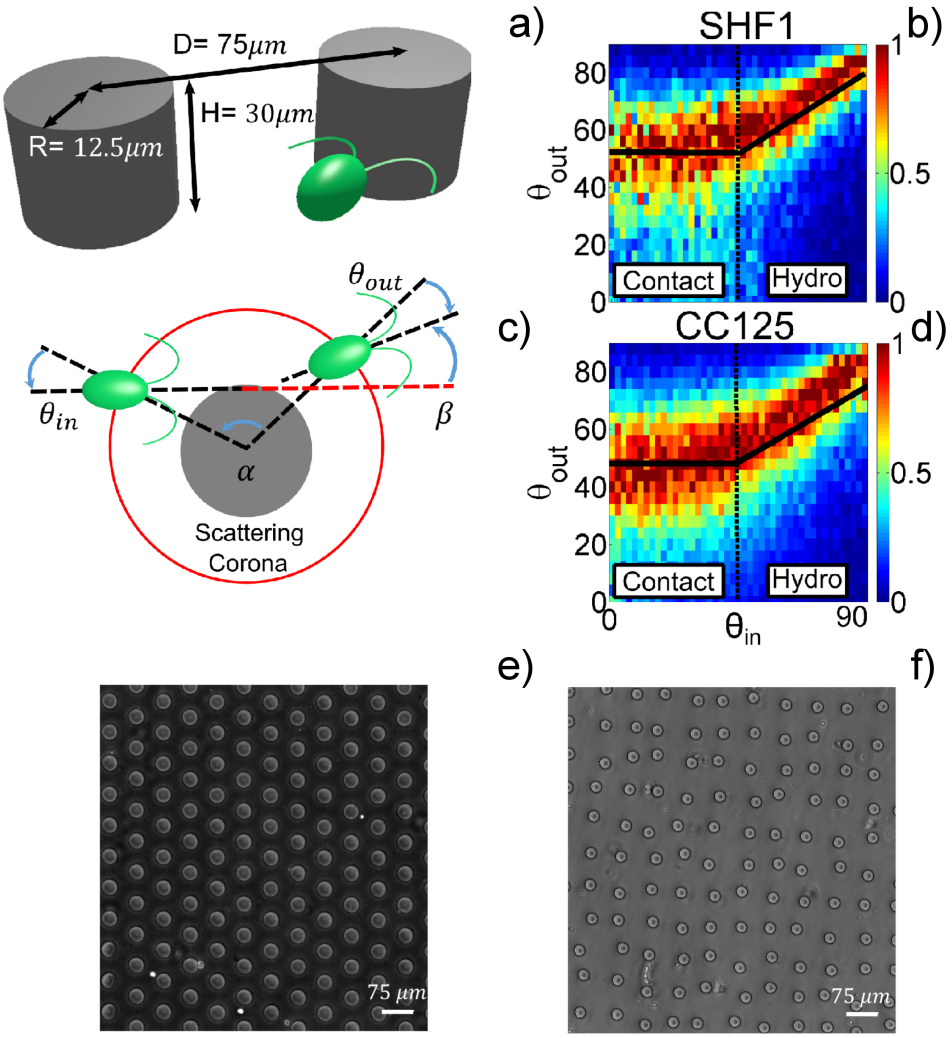

Figure 3.1: Experimental setups and scattering functions for CC125 and SHF1 strains. a) Schematics of pillar arrangement. b,d) Conditional probability for the outgoing scattering angle $p(\theta_{out}|\theta_{in})$ for CC125 and SHF1. Solid black lines indicate fit to Eq.3.5, dashed lines shows the value of θ_{in} corresponding to the switch between contact and hydrodynamic regime. c) Conventions used for measuring the signed scattering angles. e,f) Picture of a hexagonal and randomised square lattice of pillars realised using phase contrast and bright field microscopy.

vested and centrifuged for 7 minutes at 100 rcf; the supernatant is then steadily removed and replaced with fresh TAP. The CR are then left for one hour in the growth chamber at the conditions described above to recover. Algae are then loaded inside the experimental chamber and the sample is placed on a microscope stage. Cells were imaged under phase contrast with a Nikon TE2000-U inverted microscope fitted with a long-pass filter (cutoff wavelength 765 nm, Knight Optical, UK) to prevent phototactic stimulation. High throughput measurements of CR scattering off pillars are based on low magnification (10×, Ph1, NA 0.25) low frame rate (50 fps) recordings (Pike F-100B CCD camera, AVT). Cells' trajectories during the > 80k scattering events recorded for CC125 (> 45k for SHF1) were digitised using a standard particle tracking algorithm implemented in Matlab [155]. High magnification (40×, Oil immersion, NA 1.3), high frame rate (1200 fps, Vision Research Phantom V 5.2 CMOS) movies complemented the previous measurements with more detailed insight on cell dynamics during scattering events. A total of ~ 300 scattering events were recorded at high speed. Measuring the flagellar length of a sample of 50 individuals for each strain, we found the cell body to be $11.4 \pm 0.2 \mu$m for both strains while flagella are $11.2 \pm 0.2\,\mu$m for wild type (CC125) and $9.4 \pm 0.2, \mu$m for short flagella mutant (SHF1), as shown in Figure 3.2b.

3.2.2 Scattering observables

We extract radius and centre of pillars in experimental images using MATLAB built in Hough transform. We choose to define the scattering with reference to a circular impact area, concentric to the post and extending from its surface up to a distance ~ $3.5\,\mu$m larger than the flagellar length, giving a radius of $28\,\mu$m for CC125 (SHF1: $25\,\mu$m); results are not affected by choosing a different corona size within reasonable limits, as shown in Figure 3.2c. We define the impact point as the first tracking point within the scattering region and analogously the take off as the last point inside the corona. The incoming swimming direction $\mathbf{n_{in}}$ is extracted by linearly fitting the five points right before the impact point while the outgoing swimming direction $\mathbf{n_{out}}$ analogously consists of the fitting of the five points after the take off. This approach greatly reduces the noise intrinsic to real swimming trajectories and gives us a simple and reliable method to measure scattering quantities. θ_{in} (θ_{out}) is defined as the signed angle between $\mathbf{n_{in}}$ ($\mathbf{n_{out}}$) and the vector joining the pillar centre with the point where the cell enters (exits from) the scattering corona. The scattering process is symmetric with respect to the sign of θ_{in}, so we consider equivalent events with a positive or negative sign of the incoming angle. This is done by appropriately inverting all the relevant observables with $\theta_{in} < 0$. We will call α

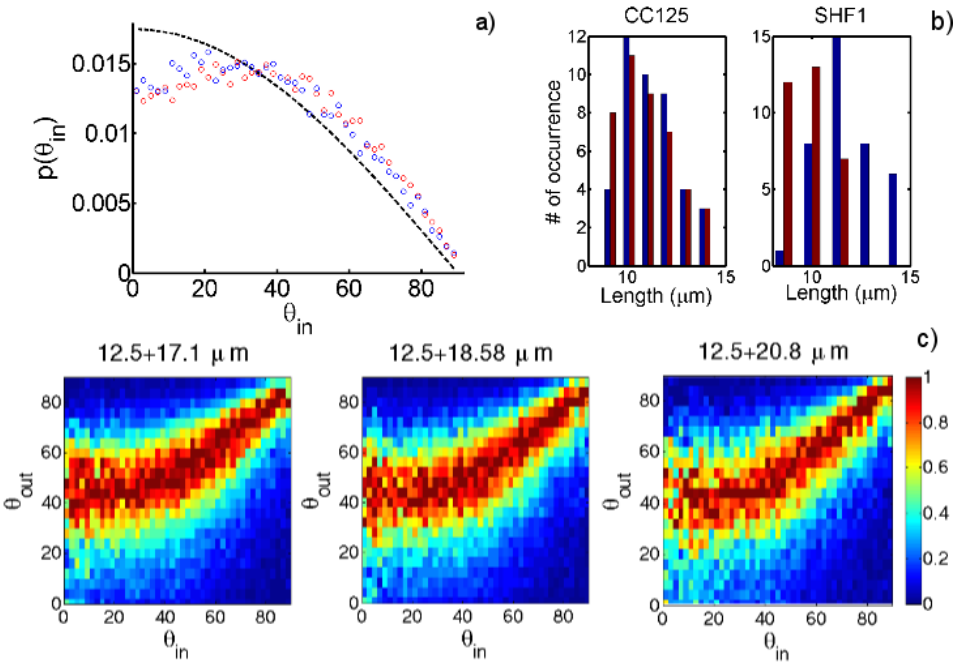

Figure 3.2: Experimental quantities relative to CC125 and SHF1 and scattering function with different scattering coronas. a)Probability to observe a scattering at a given θ_{in} for a random and hexagonal lattice and analytic solution for an isolated 2D disk with uniform impact parameter. b)Distribution of flagella and body size for the strains used in the experiments. c) Scattering functions obtained with three different sizes of scattering corona

the total angle swept by the swimmer around the post during the scattering event and β the angle between $\mathbf{n_{in}}$ and $\mathbf{n_{out}}$. For sign conventions see Figure 3.1c.

3.3 Simulations

We consider a minimal "puller" swimmer model consisting of three Stokeslet beads connected by springs. We assume constant propulsive forces concentrated on the two flagella beads with radius half the body-bead; see the illustration in Fig.3.3. Using a zero force condition on the entire swimmer and a balance of forces on each bead we can derive the equation of motion for each bead. The coupled dynamics of the beads B, L, R (denoting the swimmer body, left and right flagellum beads respectively) can be described by

$$\begin{aligned}\frac{d\mathbf{x}_k}{dt} =& \frac{1}{\xi_k}\left[\delta_{k,(L,R)}\mathbf{f}_k^f + \mathbf{f}_k^c + \mathbf{f}_k^x\right] + \sum_{j=(B,L,R)} G_{a_j}(\mathbf{x}_k,\mathbf{x}_j)\left[(1-\delta_{k,j})\mathbf{f}_j^c + \mathbf{f}_j^x\right] \\ &+ \sum_{j=(B,L,R)} \tilde{G}_{a_j}(\mathbf{x}_k,\mathbf{x}_j)\left(\mathbf{f}_j^c + \mathbf{f}_j^x\right)\end{aligned} \tag{3.1}$$

for $k = (B, L, R)$. Here $\xi_k = 6\pi a_k$ are the Stokes drag coefficients and $a_B = 1/3$, $a_L = a_R := a_F = 1/6$ are the bead radii. The propulsive forces $\mathbf{f}_L^f$ and $\mathbf{f}_R^f$ act only on the two flagella beads L and R. The connector spring forces $\mathbf{f}^c$ follow a finitely extensible nonlinear elastic (FENE) spring model [156]. The repulsive steric forces $\mathbf{f}_k^x$ are calculated with the Lennard-Jones potential activated at $2^{1/6}a \approx 1.12a$ distance away from a bead's center.

$$G_a(\mathbf{x}_k,\mathbf{x}_j) = \frac{1}{8\pi}\left[\frac{r^2+2a^2}{(r^2+a^2)^{3/2}}\mathbf{I} + \frac{(\mathbf{x}_k-\mathbf{x}_j)(\mathbf{x}_k-\mathbf{x}_j)^T}{(r^2+a^2)^{3/2}}\right]$$

with $r = ||\mathbf{x}_k - \mathbf{x}_j||$, is a regularized 3D Stokeslet where the regularization parameter a is the radius of the bead. Near a no-slip wall, the method of Stokeslet images, here denoted by $\tilde{G}_a$, are employed to calculate the fluid flow at each bead's position. The model is discussed and analyzed elsewhere for flat surfaces [157]. The wall in this case is a cylindrical pillar: since a solution for an image system with respect to a curved surface is not known, we approximate the pillar as flat in the vicinity of the swimmer and we use the solution for an infinite flat surface for each of the three Stokeslet beads as described in [35]. We believe we still obtain good agreement with the experimental results because the error introduced by this approximation is small compared to the one introduced by approximating a CR using the three beads model. To approximate the experimental setup with the pillar diameter 25 μm and algae average body radius 6 μm, we take the pillar diameter to be $4\,a_B$. We take $L_F = 2a_B$ and $\theta_F = 70^\circ$. Note that the model

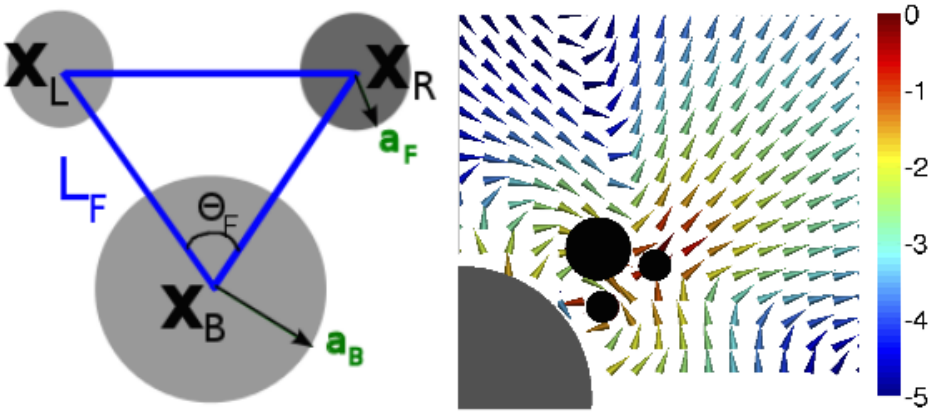

Figure 3.3: Diagram of the three-bead and springs swimmer model and the flow field (log scale) generated near a cylindrical pillar.

is deterministic, though noise could be added to the dynamics. To show the impact of algal rotation on swimmer trapping at the cylinder surface, we incorporate a periodic rotation of the flagellar beads in the equations described above. Depending on the configuration of a non-rotating three-bead swimmer with respect to the pillar, we observe different regimes shown in Fig. 3.4(a-e). When the swimmer configuration is perpendicular to the pillar, we observe (a) a hydrodynamic regime for high incoming angles (θ_{in}> ${\theta_{out}}^* \simeq 50°$) where the swimmer does not touch the pillar though it interacts with it hydrodynamically, (b) a trapping regime for low incoming angles ($\theta_{in}< 20°$) where the the swimmer orbits around the pillar, (c) a contact and scattering regime at intermediate incoming angles. When the swimmer configuration is tangential to the pillar surface, we observe (d) a hydrodynamic regime for high incoming angles; (e) a trapping and orbiting regime for low incoming angles . Note that in this latter configuration, scattering does not happen. However, if swimmer rotation about its main axis is included in the dynamics, the swimmer can escape entrapment and scatter away, as illustrated in Fig. 3.4f. For a swimmer in the perpendicular configuration, the dependence of the scattering angle on the incoming angle, $\theta_{out}(\theta_{in})$, is shown in Fig. 3.5 in the two cases $L_F = 2\,a_B$ (black) and $L_F = 1.8\,a_B$ (red), together with fits to Eq. 3.5 (solid lines). For $\theta_{in} \lesssim 30°$ the simulations deviate from the experimentally observed behaviour ($\theta_{out} = \theta_0^*$) due to proximity to the trapping threshold. Indeed the presence of a trapping regime highlights the fact that differently from the case of hydrodynamic scattering, a more detailed model is necessary to capture the correct behaviour of the swimmer during contact with the pillar.

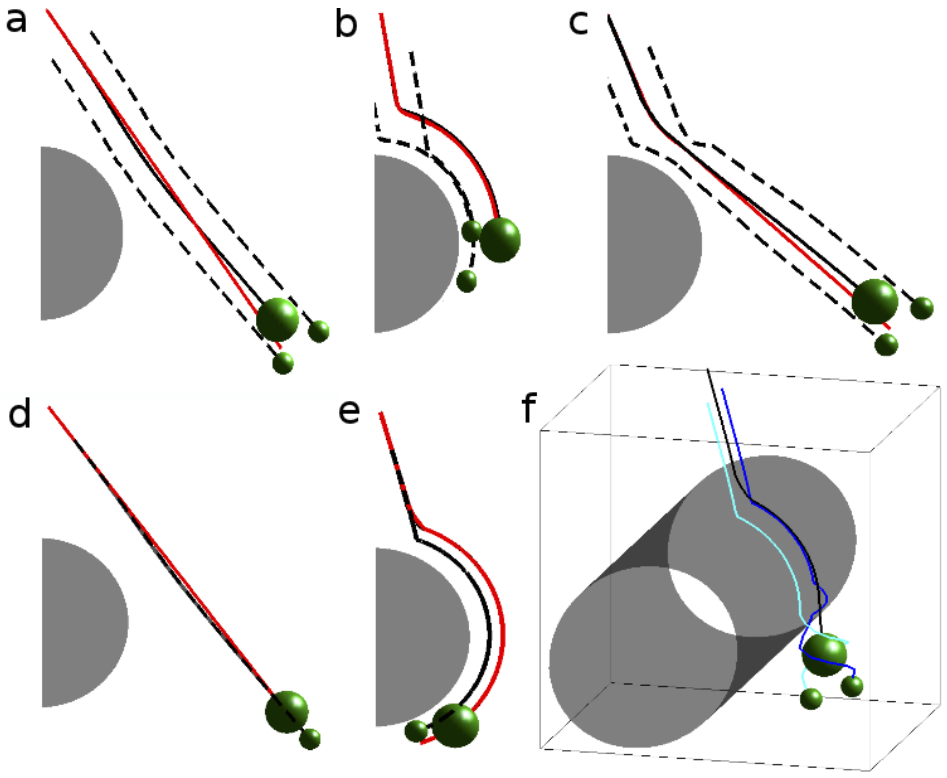

Figure 3.4: (a-c) Non-rotating swimmer with flagella configuration perpendicular to the surface. Examples of (a) hydrodynamic regime; (b) trapping regime; (c) scattering regime. (d,e) Non-rotating swimmer with flagella configuration parallel to the surface. Examples of (d) hydrodynamic regime; (e) trapping regime. This configuration does not display a scattering regime. Red lines are trajectories where hydrodynamics has been switched off. (f) Rotation-mediated escape: a swimmer with configuration tangential to the pillar surface is trapped and orbits around the obstacle, but it can escape when the rotation about the main axis is switched on.

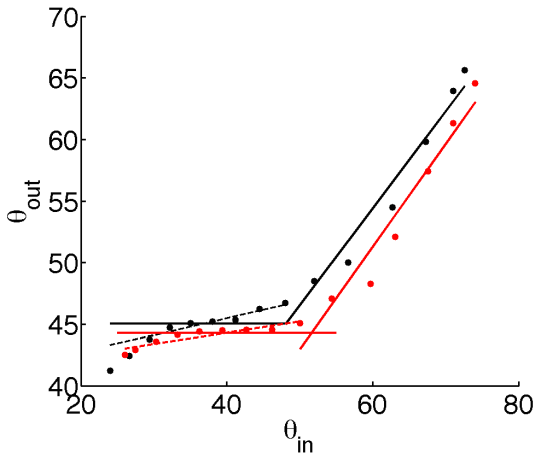

Figure 3.5: Scattering angle $\theta_{out}(\theta_{in})$ for simulations with a swimmer in perpendicular configuration with $L_F = 2a_B$ and $L_F = 1.8a_B$ (black and red circles respectively). Solid lines are fits to Eq.3.5, where fit values can be found in Table 3.1. Dashed lines are linear fits for the simulation results in the range $\theta_{in} = 25° \rightarrow 45°$ with slopes $m = 0.137$ and $m = 0.1$ (black and red dashed lines respectively).

	θ^*	θ_0^*	m	q	$d_{min}(\theta^*)$	ℓ	θ_{rs}
CC125	44°	(48 ± 1)°	0.59 ± 0.01	(22 ± 0.5)°	10.7 ± 0.1 μm	11.2 ± 0.2 μm	(33.3 ± 0.4)°
SHF1	45°	(50.76 ± 1)°	0.64 ± 0.05	(21 ± 0.4)°	9.0 ± 0.2 μm	9.36 ± 0.2 μm	(50.0 ± 0.7)°
$CC125_{sim}$	53^o	$(45\pm1)^o$	0.78	7.23°	$1.58a_B$	$2a_B$	−−
$SHF1_{sim}$	51.5^o	$(44.3 \pm 1)^o$	0.83	1.3°	$1.41a_B$	$1.8a_B$	−−

Table 3.1: Synopsis of experimental and simulation parameters. $(\theta^*, \theta_0^*, m, q)$ are defined in Eq. 3.5; $d_{min}(\theta^*)$: minimal distance of *Chlamydomonas* from the pillar surface for $\theta_{in} = \theta^*$; ℓ: average flagellar length; θ_{rs}: characteristic decay angle for the probability of random scattering.

3.4 Results

3.4.1 Random scattering

The ~ 300 scattering events recorded at high speed reveal that the direct collision with the pillar surface can sometimes induce *Chlamydomonas* to align along the short dimension of the sample cell (i.e. along the optical axis). During these events, the cell alternates periods of clockwise and counter-clockwise swimming along the pillar circumference. As a consequence, the memory of the initial direction is lost and the cell eventually leaves the scattering corona with an equal probability of having positive or negative θ_{out}. We refer to these as *random scattering* (RS) events. Notice that during standard scattering, instead, $\theta_{in}$and θ_{out}have consistently the same sign, and the scattering process involves

motion exclusively along the focal plane of the objective (i.e. no reorientations along the optical axis). Let us now consider the "negative" scattering events, i.e. those with opposite signs for $\theta_{in}$and θ_{out}. These are certainly of the random type, and are readily recognised among the thousands of scatterings recorded at low-magnification. The red lines in Fig. 3.6c,d show the distribution of the duration of negative scattering events for each of the two strains used, **multiplied by 2**. We use this to approximate the curve that would be obtained from the totality of the random scattering events. Notice that the tail of this doubled curve matches exactly that of the distribution of scattering duration for all the events recorded (black lines). Since the long-lasting scatterings are only random, the agreement supports the assumption that the red lines in Fig. 3.6c,d represent well the distribution of the duration of all RS events, not just the negative ones. This was further tested by selecting all the events lasting longer than 0.75 s, and comparing their behaviour with that of all negative scattering events. We find consistently good agreement between the two, as shown e.g. in Fig. 3.6b. The doubled distributions from the negative scatterings are then used to set thresholds in the scattering duration allowing us to either retain most of the deterministic scattering events and discard most of the random ones or *vice versa*. We select only events lasting less than 0.32 s in the former case, and longer than 0.75 s in the latter. As shown in Fig. 3.6a), 0.32 s is an appropriate threshold to select deterministic scattering events. RS, as their name would suggest, presents an almost uniform distribution of outgoing angle; we tested that these distributions do not change appreciably if different thresholds are selected, as long as the new thresholds are lower/higher than those we report above, for deterministic/random events respectively. As visible in Figure 3.6e, the scattering function for random scattering is, as expected, almost uniform, with zero scattering events with $\theta_{out} = \pm 90$ and symmetrical respect to $\theta_{out} = 0$, justifying our initial assumption that during a random scattering there is an equal probability of observing a resulting positive or negative θ_{out}.

Probability to perform random scattering

To model the process leading to random, rather than deterministic, scattering we make the following hypotheses: i) a cell will perform random scattering with probability 1 when the angle that its back-front axis makes with the local normal to the surface, θ, is 0; ii) a cell will perform random scattering with probability 0 for $\theta = \theta_d$; iii) a cell has an effective rotational diffusion D_r; iv) there is an effective angular speed ω -which we interpret as being due to flagella- advecting θ towards θ_d. As a result, the angle θ will follow a simple 1D Brownian process in the interval $[0, \theta_d]$, with absorbing boundaries. At the continuum level this is described by the following Fokker-Planck equation for the

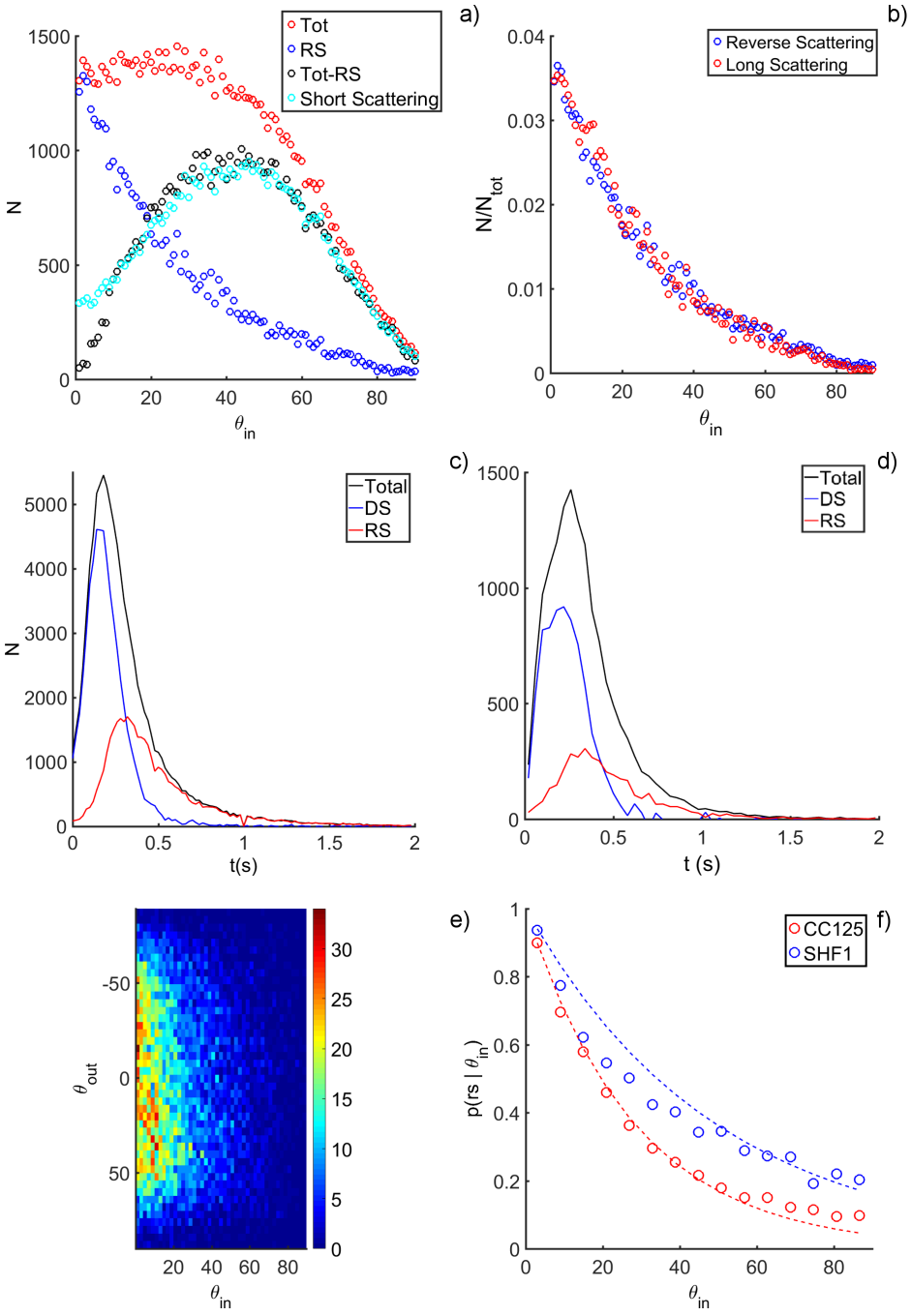

Figure 3.6: Random scattering results. a) Distribution of θ_{in} for all recorded scattering events (red circles) and random scattering (blue circles). The black curve is obtained by subtracting random events from the total distribution, and is compared to the cyan curve, which shows results for events lasting less than 0.32s. b) Distribution of incoming angle for events lasting longer than 0.75s (red) and for scattering events resulting in a negative θ_{out} (blue). c,d) Time distribution for deterministic (blue), random (red) and all scattering events (black). e) $p(\theta_{out}|\theta_{in})$ for random scatterings. f) Distribution of θ_{in} for random scatterings for CC125 and SHF1.

concentration $c(\theta, t)$ of Brownian walkers at position θ at time t

$$\frac{\partial c}{\partial t} = \frac{\partial}{\partial \theta}\left(-D_r \frac{\partial c}{\partial \theta} + \omega c\right). \tag{3.2}$$

The probability $P_{rs}(\theta_{in})$ that a cell with incoming angle θ_{in}will perform random scattering is then given by the probability that a Brownian walker starting at $\theta = \theta_{in}$ will be absorbed by the boundary $\theta = 0$. This can be easily estimated by pinning the concentration at a specific coordinate $\theta_{in}$to a fixed value c_0 and solving for the steady state solution. The steady state currents towards $\theta = 0$ and $\theta = \theta_d$ are respectively given by

$$j_0(\theta_{in}) = -\frac{c_0\omega}{e^{\frac{\omega\theta_{in}}{D}} - 1} \quad ; \quad j_d(\theta_{in}) = \frac{c_0\omega}{1 - e^{-\frac{\omega(\theta_d - \theta_{in})}{D}}}, \tag{3.3}$$

from which the probability $P_{rs}(\theta_{in})$ can be simply calculated as

$$P_{\mathrm{rs}}(\theta_{in}) = \frac{|j_0(\theta_{in})|}{|j_0(\theta_{in})| + j_d(\theta_{in})} = \frac{e^{-\frac{\omega\theta_{in}}{D}} - e^{-\frac{\omega\theta_d}{D}}}{1 - e^{-\frac{\omega\theta_d}{D}}}. \tag{3.4}$$

As shown in Figure 3.6f, the probability of performing a random scattering for both strains fits nicely with an exponential decay, with SHF1 mutant having a higher probability of performing RS for large value of θ_{in}, probably due to the intrinsically noisier flagellar beating pattern.

3.4.2 Deterministic scattering

After subtracting random scattering from the total distribution, the duration of the remaining events is normally distributed with $\mu = 0.125s$. The conditional probability $p(\theta_{out}|\theta_{in})$ is shown in Figure 3.1b,d for each of the two considered strains; the two scattering functions look qualitatively similar and consist of two parts: for low values of $\theta_{in}$the outgoing angle seems to be centred around the same value of θ_{out}regardless of the approaching direction of the alga. As the angle of impact increases and gets more parallel to the surface of the pillar, the resulting output tends to increase linearly up to a maximum value of θ_{out}= 85^o.

In Figure 3.7a,c, average θ_{out}as a function of $\theta_{in}$is plotted; for small $\theta_{in}$the function shows a very weak linear dependence, while for θ_{in}> 55^o, the curve is well fit by a line with slope $m \simeq 0.6^o$/degree for WT algae. We approximate the function as follows:

$$\langle\theta_{\mathrm{out}}\rangle(\theta_{in}) = \begin{cases} \theta_o^* & \text{if } \theta_{in} < \theta^* \\ m\theta_{in} + q & \text{if } \theta_{in} \geq \theta^* \end{cases} \tag{3.5}$$

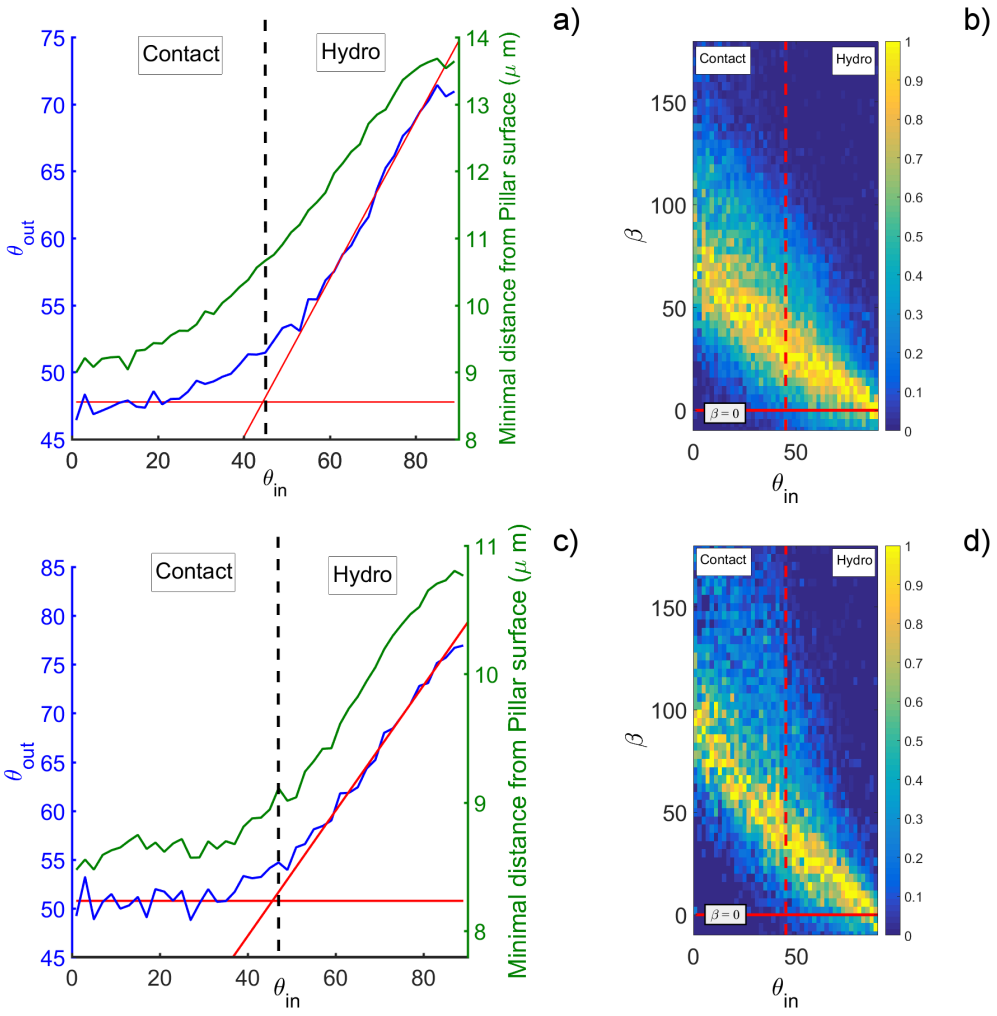

Figure 3.7: Average minimum distance and deviation. a,c) Average θ_{out} (blue) and distance of cell centroid from the pillar surface (green). b,d) Conditional probability for the deviation angle β (see Figure 3.1a for convention) $p(\beta|\theta_{in})$.

which is plotted as a red line in Figure 3.7. We define θ^* as the intersection between the linear fit and θ_o^*; our coarse grained model doesn't take into account the transition between the two regimes which takes place in a range wide about 20-30^o of θ_{in}. For both strains, the approximated curve maximum deviation from the actual data is $\sim 3.4^o$ which is an error $\leq 6\%$ which justifies our coarse grained approach. See table 3.1 for values measured in experiments for different strains and parameter values used in simulations.

Hydrodynamic regime

The hydrodynamic regime occurs when the minimum distance between the alga and the pillar surface during the scattering is larger than the flagellar length, so that only hydrodynamic interactions are possible. Several theoretical studies based on far field hydrodynamics suggest that a puller microorganism swimming by a solid wall experiences a reorientation that redirects its trajectory away from the surface; the graph of $\beta(\theta_{in})$ shown in Figure 3.7b,d shows that the deflection exerted by the pillar ranges from $(33.5 \pm 0.87)^o$ for θ_{in}= 57^o to $(5.1 \pm 1)^o$ for θ_{in}= 84^o never reaching zero. Since the minimum distance reached by algae at these incoming angles is larger than the flagellar length, no contact is present and the deflection can only be ascribed to hydrodynamics. In Figure 3.8, we can see how, for these θ_{in}, the swimming velocity increases by roughly 10% in the first part of the scattering; this happens also in our simulations (Figure 3.9a,c) when hydrodynamic forces are present and remains constant when they are not included. It is noticeable that in simulations, right after the initial increase, there is a dip in the swimming speed of comparable magnitude which is not present in the experimental results; this suggests that flagella are still able to beat at the same frequency despite the increased drag. This suggests that flagella may have more power at their disposal than what they usually employ in their beating cycle far from solid surfaces: as a consequence, when the drag increases they are still able to beat at 50 Hz by consuming more energy.

Contact regime

For lower θ_{in}, and consequently smaller d_{min}, flagella make contact with the pillar walls and steric interactions become dominant. Looking at Figure 3.8, we can separate the scattering mechanism into three phases: the initial collision between the swimmer and the pillar corresponds to the sharp drop that last between 40 and 60 ms, depending on the incoming angle. Steric arguments [158] would predict $v_0 \sin(\theta_{in})$ (angle in radians) as the minimal speed. We observe a decrease of significantly smaller magnitude (Fig. 3.8a), reaching at most $\sim 25\%$ for almost head-on events. The discrepancy is due to partial cell reorientation during slowing down, possibly due to a combination of hydrodynam-

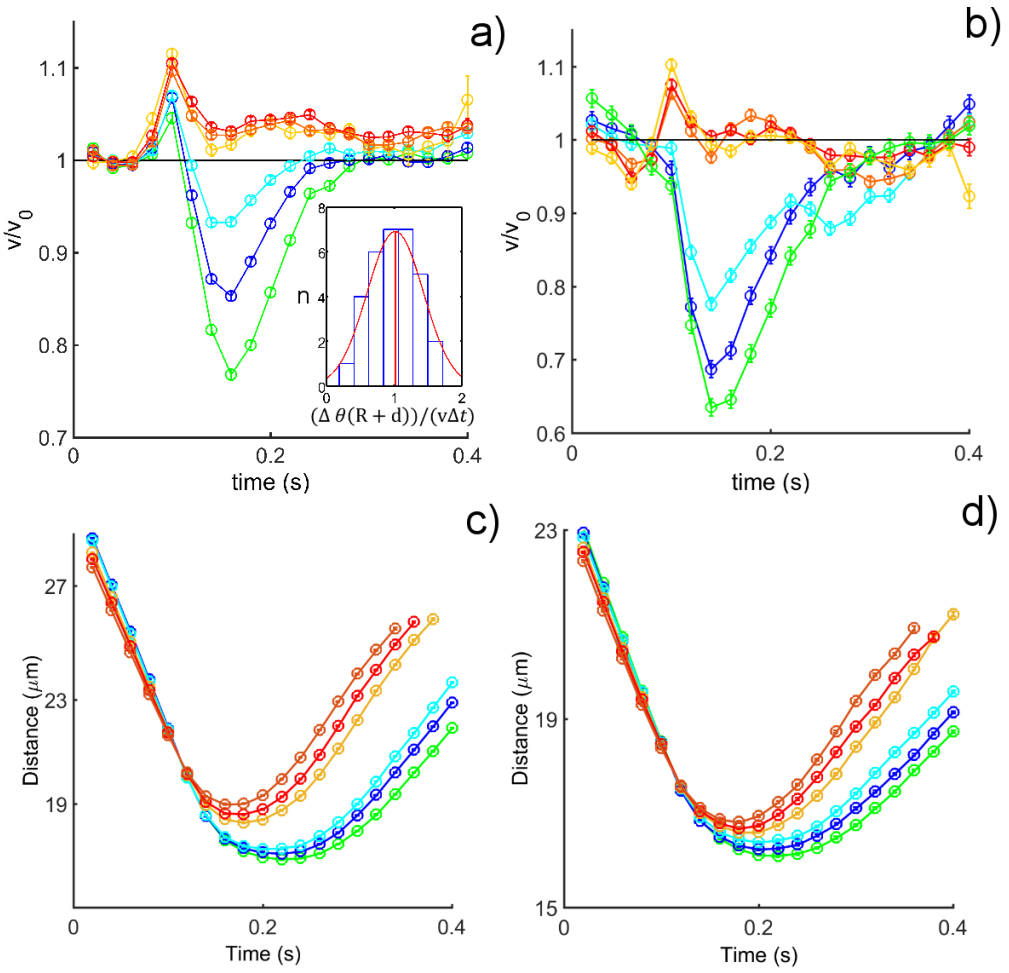

Figure 3.8: Experimental velocity and distance profile during scattering for CC125 (left) and SHF1 (right): $\theta_{in} = 0-10°$ (○), $10-20°$ (○), $20-30°$ (○), $50-60°$ (○), $60-70°$ (○), $70-80°$ (○). a,c) Experimental values of $v(t)/v_0$ during deterministic scattering events for CC125 and SHF1 respectively. Inset in a): Experimental distribution of $\Delta\theta\,(R+d)/(\Delta t\, v)$ during recovery stage ($\theta_{in} \in [0,35°]$). Red line: Gaussian fit (mean: 1.02 ± 0.07; st. dev.: 0.42). b,d) Evolution of distance from the pillar center during scattering in experiments for CC125 and SHF1.

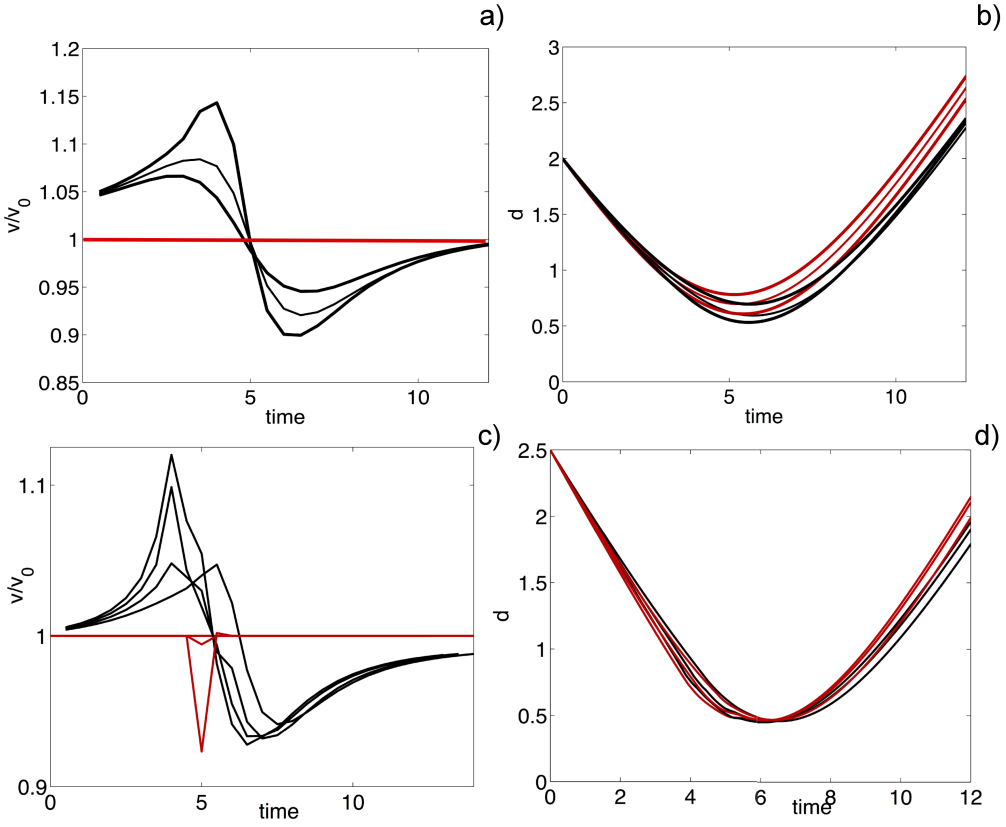

Figure 3.9: Velocity and distance profiles during scattering obtained from simulations. a,b) Swimmer velocity and distance profiles for a variety of launching angles at distance 2.0 a_b away from the pillar, normalized by the average value v_0 of v in free space when in the "hydrodynamic regime". We observe a dip followed by a recovery, though the start and end values of v are not the same due to the "hydrodynamic pull" of the swimmer by the pillar. The cases when hydrodynamics is switched off are shown in red color. c,d) Swimmer velocity and distance profiles for a variety of launching angles at distance 2.5 a_b away from the pillar when in the "contact-and-scatter regime". In all cases the swimmer is in the configuration perpendicular to the pillar surface.

ics and direct flagellar-wall contact. The reorientation is completed during the second stage, ending with a fully recovered speed ($v(t) = v_0$) and the cell aligned parallel to the pillar surface. Steric interactions imply that during this recovery, the angle θ that the cell makes with the local surface normal should obey (angles in radians) $\dot{\theta} = v(\theta)/(R+d)$, where d is the swimmer-surface separation. Assuming $v(\theta) = v_0 \sin(\theta)$, the angular variations within this stage, $\{\Delta\theta_j\}$, can be obtained from the instantaneous speed $\{v_j\}$. These should then satisfy $\left(\text{asin}(v_{j+1}/v_0) - \text{asin}(v_j/v_0)\right) = \Delta t(v_{j+1}+v_j)/2(R+d)$, where $\Delta t =$ 20 ms is the inverse frame rate. Fig. 3.8a inset shows that this is the case, supporting the interpretation that cells reorient by simply sliding over the convex, curved surface. Once the cell is reoriented parallel to the surface, if no interactions were present, one would expect to just swim away from the pillar in a straight line. If we consider a cell hitting the post at θ_{in}= 50^o, starting from $d_{min} = 9\mu m$, CC125 strain would take approximately 90 ms to leave the scattering corona; from the experiments we found this time to be 170±8 ms instead. From the high speed movies it is noticeable that both strains tend to swim along the surface of the obstacles and, when leaving, flagella are always in a plain perpendicular to the walls: in this configuration, flagellar contact is maximised and the appendix closest to the pillar pushes away during the beating cycle. $\langle\theta_{out}\rangle$ resulting from steric interactions as proposed in [52], should result to be $\langle\theta_{out}\rangle = 90^o - \arctan(l/2a)$ which corresponds to 45.51^o for CC125 and 50.61 for SHF1, which is very close to what we observe experimentally (see 3.1, p. 35 for values obtained in experiments and simulations). This interpretation suggests that the duration of scattering events should be independent of the size and curvature of the pillars used. To verify this hypothesis, we performed experiments with posts of different size: $2R = 80\mu m$. The microfluidic chamber was slightly shallower (~ 20 μm measured using a stylus profilometer) and the distance between pillar centres of 180μm. We recorded ~ 20k events and measured the scattering function, using a corona with a thickness equal to the other experiments performed for the CC125 strain and the scattering duration distribution as shown in Figure 3.10. The distribution for the two experiments overlap almost perfectly, given that the noise is higher for new experiments as the sample size is ~ 1/4 of what we gathered for the smaller pillars. We observe the scattering function shows just the plateau section while the hydrodynamic regime has nearly disappeared. This fact agrees with our model: in fact, we would expect the regime dominated by hydrodynamics to start when the minimum distance between the swimmer and the pillar centre is less than the pillar radius plus the flagellar length. It is easy to show that the hydrodynamic regime in this case should start at ~ 76^o. Also, from a comparison of the two time distribution, we can see how a random scattering has a higher probability of happening for larger pillar radii. In the simulations we show how the rotation of cells cause them to break the orbit and force

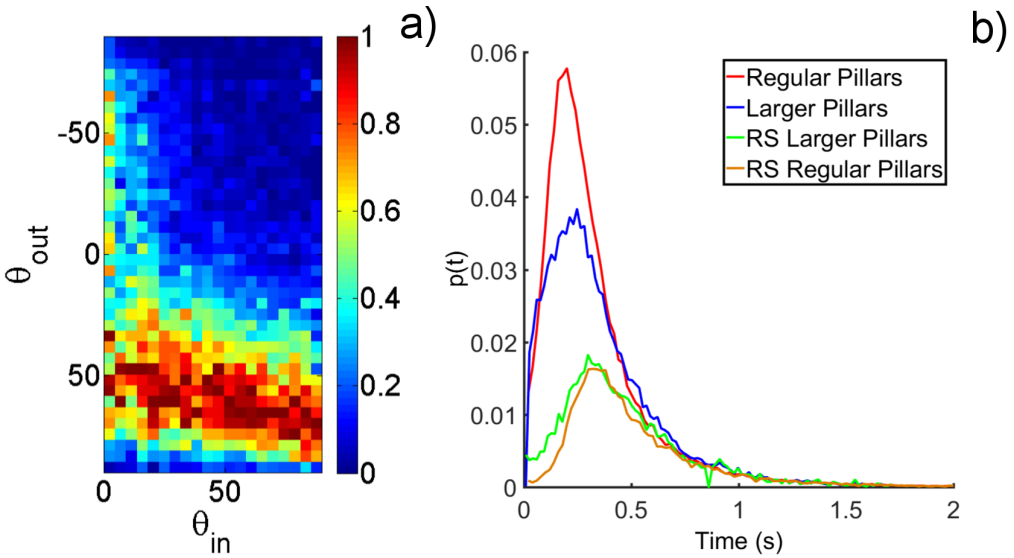

Figure 3.10: Results for larger pillars. a) Scattering function for deterministic events relative to pillars of $40\mu m$ radius. We expect the hydrodynamic part of the curve to begin around 75^o, but the binning of the data doesn't allow to show accurately the linear dependence of this branch of the curve. b) Duration distribution of scattering events for $40\mu m$ radius pillars compared to the results we obtained for the $12.5\,\mu m$ radius pillar.

them to scatter at an angle fixed by the ratio between the length of the flagella and the diameter of the body.

Given the waveform of flagellar beating, it is very unlikely that contact provides an attraction that keeps cells swimming along the pillar surface for the time it spends inside the scattering corona. The reason for this observed attraction may be the torque given by lubrication forces present when in a fluid, an extended body is dragged along a surface. Let us consider a spherical cell of radius a swimming at a speed U along the positive x-axis (horizontal), and close to a fixed pillar of circular section and radius $R = a\delta$. The gap between the two equals $a\epsilon$. The torque induced on the cell by the lubrication layer between the two bodies is given by [159]:

$$\tau_{\text{lub}} = 8\pi\eta a^2 U \frac{\delta(4+\delta)}{10(1+\delta)^2} \ln\left(\frac{1}{\epsilon}\right)$$

Note that the torque leads the cell to turn towards the pillar, rather than away from it. The angular speed ω_{rot} can be estimated immediately by balancing the lubrication torque with the rotational viscous drag $\tau_{drag} = 8\pi\eta a^3\omega_{rot}$:

$$\omega = \left(\frac{U}{a}\right) \frac{\delta(4+\delta)}{10(1+\delta)^2} \ln\left(\frac{1}{\epsilon}\right).$$

Writing $\omega_{rot} = U/\rho$, the radius of curvature of the trajectory becomes:

$$\rho = a\frac{10(1+\delta)^2}{\delta(4+\delta)}\frac{1}{\ln(1/\epsilon)}.$$

The experimental values ($R = 12.5\,\mu$m$, a = 5.7\,\mu$m$, d_{\min} \simeq 8.5\,\mu$m) correspond to ($\delta \simeq 2; \epsilon \simeq 0.5$), and give $\rho \simeq 64.5\,\mu$m. So, lubrication accounts for more than 70% of the attraction acting on cells; of course CR are not spherical and there are residual factors not considered that can account for the remaining force needed. According to this simple calculation, we expect that sufficiently large pillars would trap cells into closed orbits if it was not for the repulsion given by the flagellar beating.

3.5 Conclusions

We have presented the first experimental study of the interaction of the model microalga CR, commonly regarded as a prototypical puller microswimmer, with circular obstacles. The experiments reveal that the scattering is not simply steric, but follows qualitatively different rules depending on the angle of incidence, with direct evidence of purely hydrodynamic interaction at large angles, and a multi-stage steric/hydrodynamic process at small angles. The latter is terminated by direct flagellar contact with the surface preventing the extended trapping around the convex structure predicted by minimal models, a behaviour recapitulated by our simulations. The ability to avoid long-term trapping independently of obstacle size and shape might in fact represent a significant advantage for a soil alga like CR, which in nature needs to navigate a heterogeneous porous material. Together with these deterministic interactions, we report the existence of random scatterings, and propose a mechanism to explain their likelihood. We will show in the following chapter how these kinds of interaction have a profound impact on the motion of CR in confined environment.

Chapter 4

Chlamydomonas reinhardtii diffusion in straight channels

4.1 Introduction

Controlling biological and artificial microswimmers is crucial for future applications such as drug delivery [160, 161], bioremediation [162, 163] or stirring fluid at the submillilitre scale, for example in microreactors [164, 165]. Microswimmer trajectories, although ballistic on a short time scale, become diffusive for large observation periods [116, 166]. Controlling motility of swimmers at the sub millimetre scale is a major challenge in the field; microorganismal motility can be influenced by a series of external stimuli, such as light fields [167] and chemical gradients [9] which allow some degree of control on the spatial distribution and the swimming direction of the microswimmers. The technological implementation of these techniques on the microscale can be problematic, as this would require the use of complex active *ad hoc* components, such as optical fibres or pumping systems. Creating complex geometries, especially on PDMS microchips, is very cheap and easier to achieve at the current state of technology: in the past few years capture[168, 169], sorting[170, 171], and accumulation[49, 172] of microswimmers have been achieved in experiments and reproduced in numerical simulations. Exploiting the interactions with microstructures requires knowledge of the physics underlying the interactions of the considered swimmer with solid boundaries. Building on the results obtained in the previous chapter, we will present a study of diffusion of CR in straight microchannels of different width. Understanding algal behaviour in this geometry would represent a first building block towards a mathematical model of puller microswimmer motility in confinement. Our results show that swimmers diffusivity along the channel axis can be easily tuned by varying the channel width. As seen in Chapter 3, lubrication

forces tend to align CR swimming direction parallel to solid surfaces but rotational diffusivity randomises the swimming angles of algae[123] after the scattering interactions are over, so that boundaries work as rotational "noise quencher" for microorganisms swimming, directing their motion along a fixed direction. As a consequence, we observe that CR in narrower channels, where they interact more frequently with the channel boundaries, present a greater persistence length on the longitudinal axis; however, below a threshold width of $\sim 50\mu$m there is a sudden and unexpected drop of swimmer diffusivity and persistence length. In the following pages, we will try to explain these results, investigating CR motion and their interactions with walls. The chapter is organised as follows: we will first introduce the experimental setup and give an overview of the simulations, defining some key quantities and explaining how we measured them. We will then present data regarding algae swimming behaviour across the channel width highlighting how proximity to the walls promote alignment in algal swimming direction. We will later discuss the motion along the channel length, and how it can be regarded as a 1D persistent random motion. In the final part we will use the simulations to discuss the influence of random scattering and rotational diffusivity on the microbial transport capability of the channels.

4.2 Materials and methods

4.2.1 Experiments

We build quasi 2D microfluidic devices (thickness $\sim 25\,\mu$m) consisting of two chambers of 2×3.6 mm connected by 7 channels of length $L = 3.6$ mm and width $w = 30, 50, 100, 150, 200, 300, 400\,\mu$m as shown in Figure 4.1a. The inlets are punched at the top and bottom of the left chamber, along a direction perpendicular to the channel length: this procedure prevents the development of pressure driven flows across the channels. We inject fresh culture medium through these inlets, and we then apply pressure to both injection points using 1 ml syringes without plunges hung about 1 m above the device: since PDMS is an air permeable material, the applied pressure pushes the remaining air out of the device, filling both chambers and the channels with culture medium. We subsequently inject CC125 strain of CR, grown using the protocol discussed in Chapter 3, through the inlet and we leave them free to diffuse across the device. We record microscopy videos of 15k frames using a 2x magnification objective and a frame rate of 10 fps. We record a total $\sim$ 50k trajectories, not equally distributed among different channel widths w. In Figure 4.1b, the x and y axis convention is also shown: we will define the x axis, as the longitudinal direction of the channel while the y axis will be referred to as the transverse section of the channel. We measure scattering angles at a distance

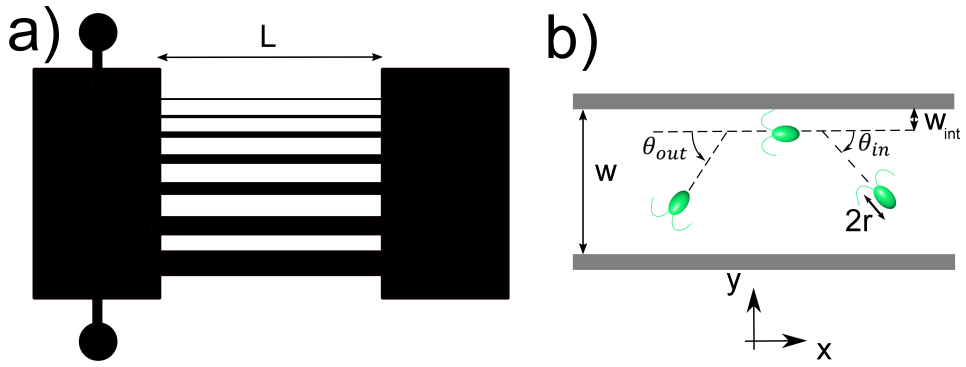

Figure 4.1: Schematics of the experimental setup. a) Scheme of the microfluidic channel used in the experiments: two rectangular chambers 3.6×2 mm connected by seven channels of width (from top to bottom) $w = 30, 50, 100, 150, 200, 300, 400\,\mu$m respectively and length $L = 3.6$mm. Circles placed on the top and bottom of the left chamber are punched using a biopsy puncher and culture medium is injected with a syringe through a needle placed in the punched holes. b) Representation of the inside of the channel; w is the channel width, w_{int} is equal to the average flagellar length for CC125 strain measured in chapter 3 and is the distance at which CR touch the channel wall with their flagella: in experiments it is the distance from the wall where both θ_{in} and θ_{out} are measured, in simulations it is the distance at which interactions between particles and boundaries are triggered. θ_{out} greater than 90° are considered to be "random scattering" (see Chapter 3 for definition). The axes at the bottom are the convention we will refer to in the remainder of the chapter.

$w_{int} = 11\,\mu$m, equal to the average length of CC125 flagella measured in Chapter 3, from the channel walls. We define the incoming and outgoing direction $\mathbf{k}_{in}$ and $\mathbf{k}_{out}$ by fitting the last three point before the alga enters the interaction zone and the first three points after leaving it respectively. We then measure the scattering angles θ_{in} and θ_{out} with respect to the x axis of the channel, using the convention shown in Figure 4.1b. Note that events resulting in a $\theta_{out} > 90°$ are random scattering events (see Chapter 3 for definition).

4.2.2 Simulations

Motion in "the bulk"

We model the swimming of each individual cell far from the walls (the "bulk") as a persistent random walker, whose position is given by the following equations of motion,

$$\begin{aligned} \dot{\vec{x}} &= v_0\,\hat{v}(\theta) \\ \dot{\theta} &= \sqrt{2D_\theta}\,\xi_\theta. \end{aligned} \tag{4.1}$$

where the dot indicates the temporal derivative, $\vec{x}$ is the position of the cell, θ is the moving direction and $\hat{v} = (\cos(\theta), \sin(\theta))^T$. Eq. (4.1) indicates that the centre of mass of

the cells moves with a mean speed v_0 while their moving direction is affected by a white noise that obeys $\langle \xi(t) \rangle = 0$ and $\langle \xi(t)\xi(t') \rangle = \delta(t-t')$. The amplitude of the angular noise is such that the angular diffusion coefficient is D_θ. We assume there are no interactions between cells as we use a low concentration of algae in experiments.

Interaction with the walls

We consider that cells interact with the walls through hydrodynamic and steric forces. The interaction takes places in a region within a distance of w_{int}, from the walls, as depicted in Figure 4.2. After entering this region, cells start steering at a rate:

$$\dot{\theta} = k_{\theta_i} \sin(\theta^* - \theta) + \sqrt{2D_\theta}\xi_\theta, \tag{4.2}$$

where k_{θ_i} is an arbitrary parameter, until their swimming angle reaches a value θ^*; at this point we consider the scattering event to be over and the cell starts moving away from the wall. We consider also that this relaxation constant can take two different values, k_{θ_1} and k_{θ_2}, depending on whether the cells are moving towards or away from the wall, to reflect the back/front asymmetry of the cells. We implement random scattering by setting a fixed probability r_0 of performing random scattering depending on the incoming angle θ_{in}, so that the occurrence of random events is maximum for $\theta_{in} = 90°$ and is equal to zero for $\theta_{in} = 0°$. Following a random scattering, θ_{out} is picked randomly from a uniform distribution $\theta_{rnd} \sim \mathrm{U}[-\pi/2 + \delta_\theta; \pi/2 - \delta_\theta]$ where δ_θ is a parameter chosen so that particles leave the interaction zone in a finite time (with a scattering angle of 0°, a particle would continue swimming inside the interaction zone in a direction parallel to the wall without ever leaving it). In this model, for instance, we can turn off random scattering by assuming $r_0 = 0$ or set $r_0 = 1$ so that every interaction with the walls results in a random event.

v_0	$80\mu m/s$
D_θ	$1.125\frac{rad^2}{s}$
k_{θ_1}	$3s^{-1}$
k_{θ_2}	$18s^{-1}$
θ_{det}	$^1 75°$
θ_{rnd}	$\sim \mathrm{U}[-\pi/2 + \delta_\theta; \pi/2 - \delta_\theta])$
$\delta_\theta])$	9°
W_{int}	$15\mu m$
r_0	$> r_{0min}$

Table 4.1: Model parameters. v_0 is measured directly from the experiments, k_{θ_1} and k_{θ_2} were fit to reproduce the scattering results from the experiments. D_θ, W_{int} and r_0 are free model parameters.

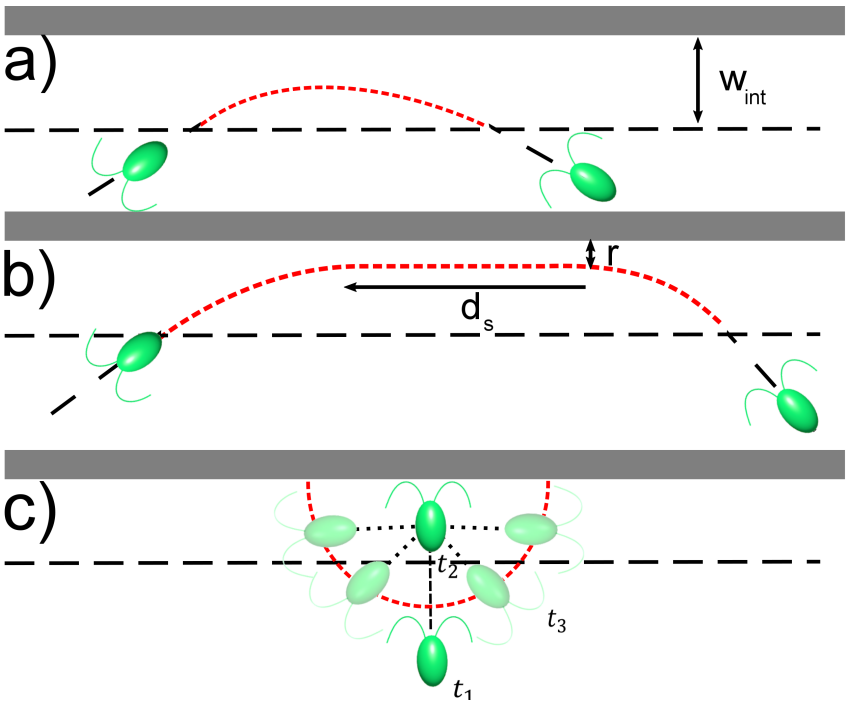

Figure 4.2: Interaction scheme in the simulations. Region of interaction w_{int} and an example of trajectory for each of the possible scattering type. Cells begin to interact with the wall when they are within a distance less than w_{int} from it. a) Hydrodynamic scattering: after entering the interaction zone, cells start steering with a rate k_θ until they either reach $\theta^\star_{out}$. b) Deterministic scattering: if the cell reaches a distance from the wall equal to its body radius r, it adhere to the surface and start sliding along it for a distance d_s before leaving at a fixed angle $\theta^\star$. c) Random scattering: after reaching the distance r from the wall, cells have a fixed probability to perform random scattering: in this case the outgoing angle is drawn from a uniform distribution of θ_{out}.

4.3 Results

We are interested in describing CR motility inside the channels, with the aim of coarse graining the effect of the transverse section of the channel on the longtudinal mobility of algae. CR are known to exhibit diffusive behaviour, swimming in straight lines with small deflections occurring at random time intervals, resulting in a persistent random walk [118, 123]. When scattering events happen at a high frequency ($1/\tau_{intra} \ll 1/\tau^\star_p$, where τ_{intra} is the time interval between two successive scattering and $\tau^\star_p$ is the persistence time in "bulk" (far from walls), we expect the algae to swim in straight lines at an angle fixed by scattering interactions between the two walls in a sort of sawtooth trajectory; on the other hand, in wider channels algae lose memory of the wall scattering, resulting in a more random motion in between two interactions with the channel edges. We will divide the data analysis in two parts: in the first section we will analyse how

some key characteristics of the algal motion change across the channel width (y axis in our convention), while in the second part, we will show how the characteristics influence the x axis dynamics of the cells, with particular focus on the x axis diffusivity.

4.3.1 Swimmers across the channel width

Figure 4.3c,d show that CR are found preferably in the immediate vicinity of the channel walls both in experiments and simulations. In experiments there is a 5-10 μm area close to the boundaries where we observe a 15-20% higher chance of finding an alga compared to the centre of the channel; this accumulation is also present in simulations although in a far more evident fashion, with a 100% higher probability of finding a cell in the immediate proximity of the wall (we use point like particles in simulations), where cells slide along the surface. In the simulations it is possible to observe a second peak in the particle distributions, in the area we defined as the interaction zone, where hydrodynamic repulsion begins to act; this second peak is present also in the experiments but is far less pronounced, with a 5% higher concentration of CR. This is significantly different from the uniform distribution one would have for brownian particles, and it is a consequence of the swimmers motility, which has been previously observed in simulations [173] for active matter, and observed experimentally for pusher-type microorganisms [144] but has been reported for puller-type swimmers only for concave surfaces [174]. In experiments the magnitude of the peaks do not vary appreciably as a function of the channel width, except for channels with $w < 50\,\mu$m where the situation is qualitatively different as the accumulation peaks relative to each side of the channel are close enough to overlap. The presence of a solid surface not only affects the concentration profile but also, more importantly, the swimming behaviour of the microorganisms: we observe in Figure 4.3a,c how the swimming direction is aligned with the channel axis for distances from the walls $r < 35-40\mu m$ and how this alignment vanishes as we approach the channel centre. This effect is evident also in Figure 4.3d, where the 2D nematic order parameter $OP_w(d)$ for different channel widths w measured at different distances from the closest wall d, defined as $< 2\cos^2(\theta_{sw}(d)) - 1 >$, shows a maximum in the proximity of walls decaying as the distance increases. The order parameter OP reach its maximum close to the wall, $OP_w(5\mu\text{m}) \sim 0.4$ and decays as d increases. The maximum value is almost constant for $100 < w < 400$ while the minimum varies significantly as a function of the channel width: in the $w = 300, 400\,\mu$m curves, OP reaches zero for $d > 80\,\mu$m, while in the $w = 100\,\mu$m curve, the minimum value observed is $OP \sim 0.2$. It is worth noting how $OP_{100}(50\,\mu\text{m}) > OP_{400}(50\,\mu\text{m})$. In the two narrowest channels, $w = 50, 30\,\mu$m the maximum value of the order parameter is observed for $w \sim 15\,\mu$m. In the simulations OP_w goes to zero in almost every channel for distances greater than 30μm; this

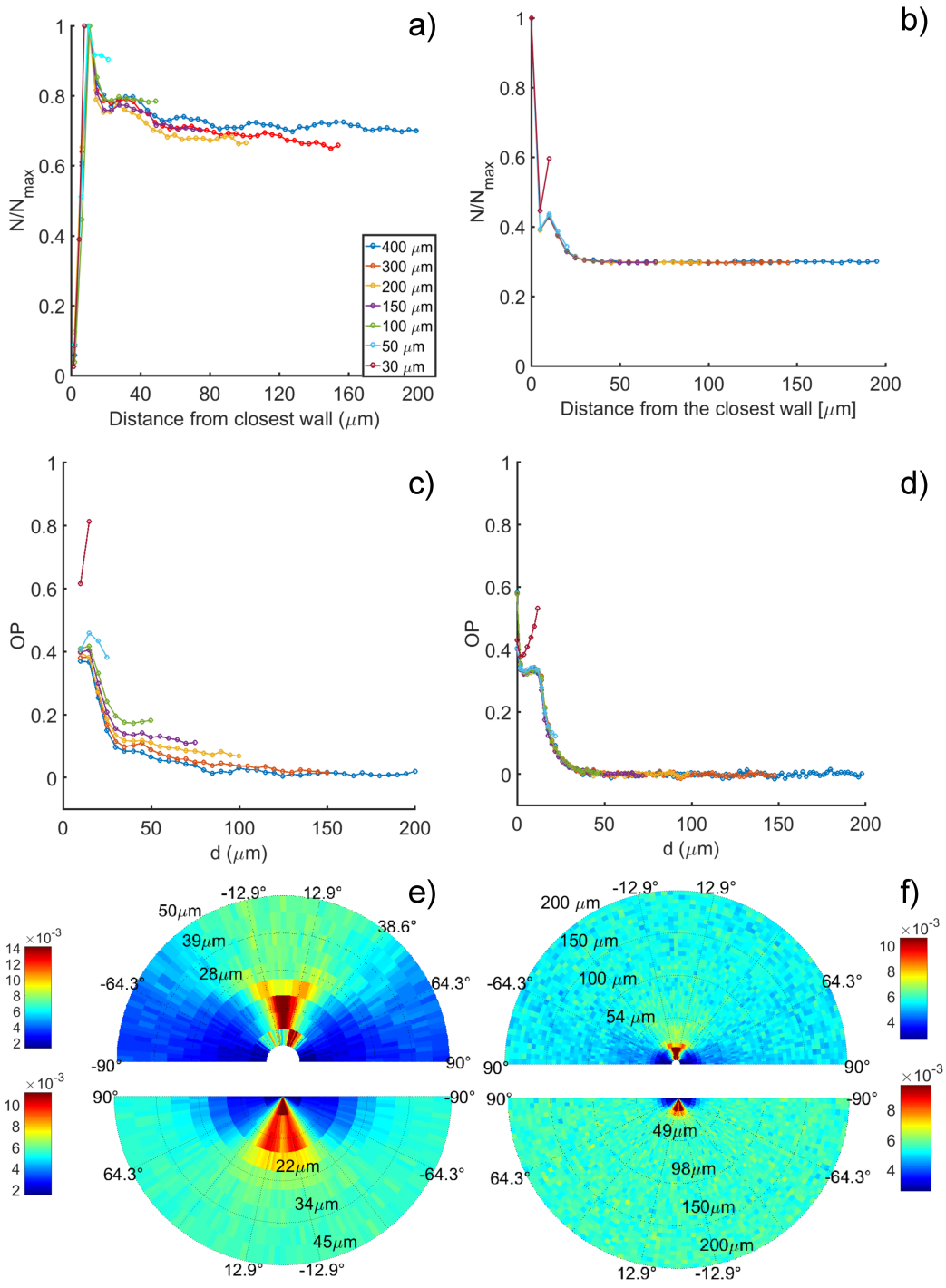

Figure 4.3: Position and swimming direction in experiments and simulations for w: 30 μm (⊖), 50 μm (⊖), 100 μm (⊖), 150 μm (⊖), 200 μm (⊖),300 μm (⊖),400 μm (⊖). a,b) Distribution of CR position along the y axis in experiments (a), and simulations (b). c,d) 2D nematic order parameter OP as a function of distance from the closest wall in experiments c) and simulations d).e,f) Distribution of swimming angle respect to the x axis in 100 μm (e) and 400 μm (f) wide channels in experiments (top) and simulations (bottom).

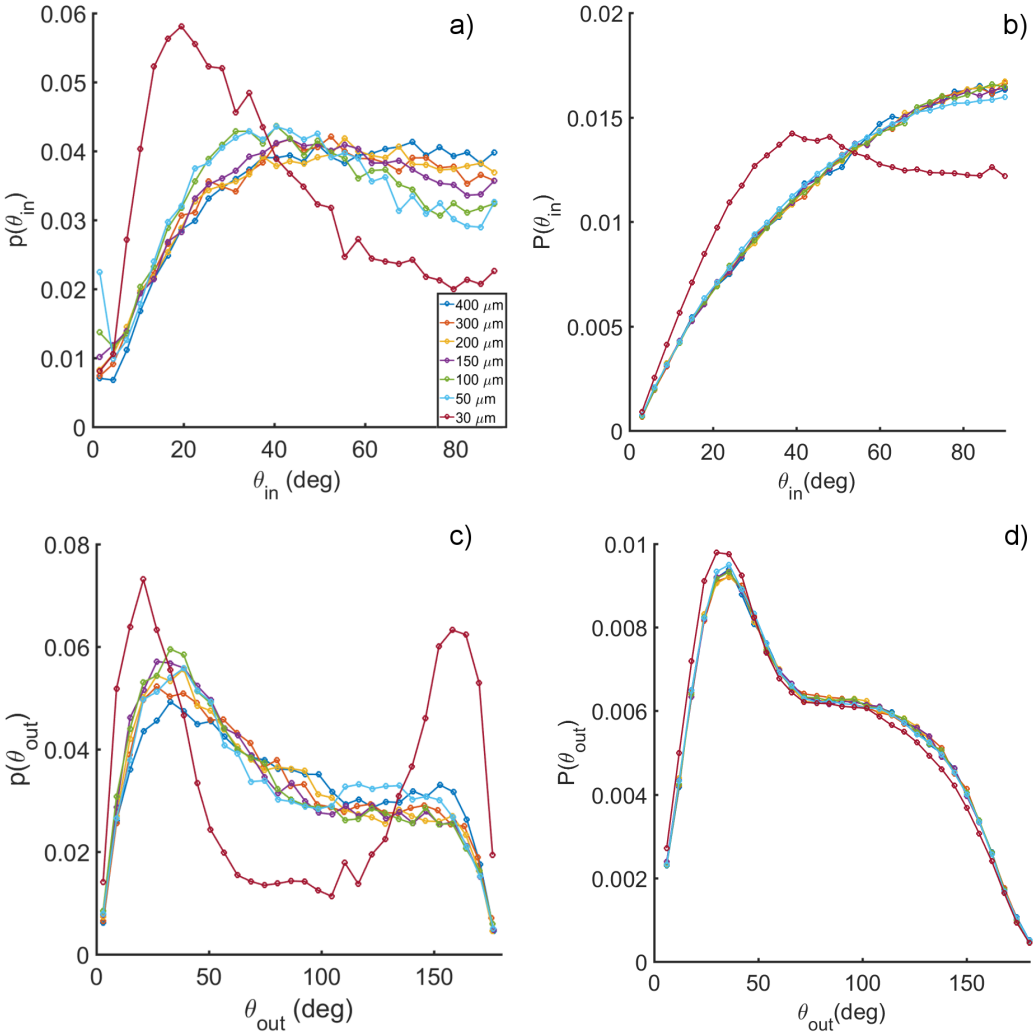

Figure 4.4: Distribution of incoming and outgoing angle θ_{in} and θ_{out} in experiments and simulations for w: 30 μm (⊖), 50 μm (⊖), 100 μm (⊖), 150 μm (⊖), 200 μm (⊖),300 μm (⊖),400 μm (⊖). a) Distribution of θ_{in} from the experiments. b) Distribution of θ_{in} from the simulations. c) Distribution of θ_{out} from the experiments. d) Distribution of θ_{out} from the simulations.

discrepancy may be due to residual hydrodynamic interactions with walls, not present in the simulations model, the investigation of which goes beyond the purpose of this chapter. In Figure 4.4 the distribution of incoming and outgoing angles for experiments (left) and simulations (right) are shown: In every channel except $w = 30\,\mu$m, we observe a peak placed around $\theta_{out} \sim 30°$ in the outgoing angle distribution on top of a quasi uniform background. The situation for the 30 μm channel is significantly different, there is a much greater portion of events resulting in a $\theta_{out} > 90^o$ (random scattering) and the peak for the incoming and outgoing angle are shifted down by 10^o compared to other channels; we believe that for very narrow channels, the alga is subject to hydrodynamic forces exerted by both walls, which heavily affect the interaction behaviour of the CR. This is consistent with the results for the previous chapter, where we show evidences of interactions between CR and a solid pillar at distances up to 15 μm, which is equal to the maximum distance from the walls in $w = 30\,\mu$m channel. This effect has repercussions also on the dynamics of random scattering, as the distribution of θ_{out} is not uniformly distributed between 0 and 180° but is peaked around $\theta_{out} \sim 150°$. All the data presented show how the CR proceed in straight line between collisions against the channel walls and how this orientation is stronger as the collisions are more frequent. This is also confirmed by Figure 4.5a,b where we see how the time interval between collision against opposite walls consist of a sharp peak that gets broader as the distance between the sides increases. In this case results of simulations and experiments are qualitatively similar.

4.3.2 Motility along the channel length

We present the distribution of displacement along the x axis for $w = 100\,\mu$m and $w = 400\,\mu$m, as examples of respectively a narrow and wide channel, in Figure 4.6; we use $w = 100\mu$m as we have a larger statistical sample. The experimental and simulation results are qualitatively similar for $w = 400\,\mu$m: the distribution shows two peaks symmetrical to Δx for $\Delta t = 2.1$s,which are still visible for larger time intervals in the experiments, and evolve towards a Gaussian distribution as Δt increases. Simulations results for $w = 100\,\mu$m show the same qualitative features as $w = 400\,\mu$m, while in experiments, the curve never resembles a normal distribution, even for $\Delta t = 16.1$s. This shows that in experiments cells possess a greater persistence length than their simulated versions: we believe that this effect may be due to hydrodynamic interactions between the wall and the swimmer at distances greater than a flagellar length. In fact, in our simulation the presence of a wall has no influence on a particle when it is outside the interaction zone: as a result, in simulations particles swimming directions are completely isotropic ($OP = 0$) when their distance from the closest wall is greater than a flagellar

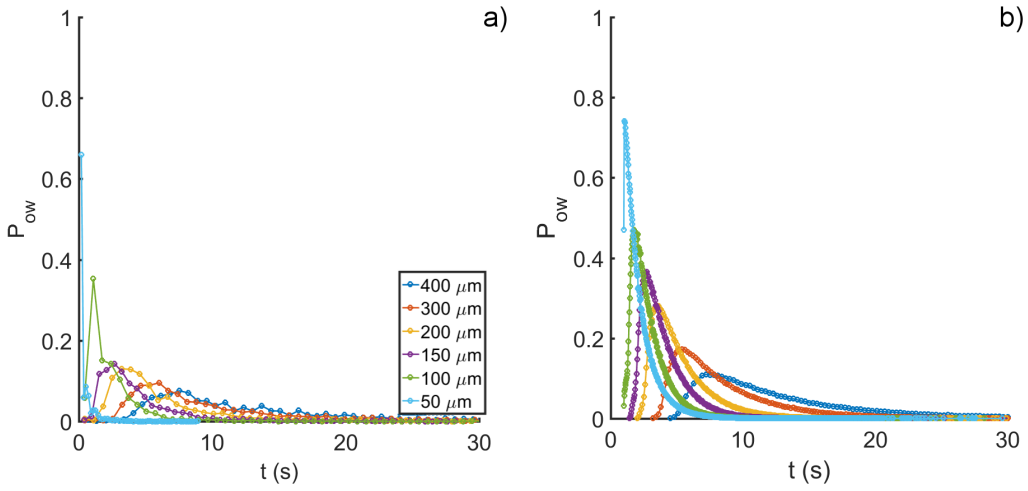

Figure 4.5: Distribution of time intervals between collisions against opposite walls of the channel for w: 30 μm (⊖), 50 μm (⊖), 100 μm (⊖), 150 μm (⊖), 200 μm (⊖),300 μm (⊖),400 μm (⊖). a) Distribution of time intervals between collision against opposite walls for channels of different width in experiments.b) Distribution of time intervals between collision against opposite walls for channels of different width in simulations.

length (10μm) while in experiments they still show a preferential swimming direction several tens of microns away from the wall (see Figure 4.3c,d). In Figure 4.7 we show the graph for the mean square displacement $< \Delta x_w^2(t) >$ divided by $2t$ (we chose to show this graph instead of the simple mean square displacement so that $\lim_{t\to\infty} < \Delta x_w^2(t) > /2t = D$, where D is the diffusion coefficient) (b) and the mean displacement $< \Delta x_w(t) >$ (a) for each different channel width. In defining $< \Delta x_w(t) >$, we initialise each trajectory pointing towards the positive side of the x axis, so that $\Delta x(0) > 0$. Both curves present an initial linear increase that gradually saturates to a plateau value; in (c) and (d) we report the average plateau value of each curve, called $x_p(w)$ and $D(w)$ respectively, obtained as an average of the respective curve values for $t > 15$s while in (e) and (f) we report the intersection times between the linear fit of the first 5 s of each curve and the relative plateau value. We call persistence time τ_p the intersection time for curves in (a) and ballistic time τ_b the corresponding values for curves presented in (b). All the quantities present a very similar trend: D and τ_b increase as w decreases up to a maximum value for $w = 50\mu m$ and a steep decrease in channels where $w = 30\mu m$, while $x_p(w)$ and $\tau_p(w)$ present a maximum for $w = 100\mu m$ and a decrease or lower w. It's interesting to note that $x_p(w)^2/\tau_p(w)$, shown in Figure 4.9, is dimensionally a diffusivity and its graph is very similar to one for the diffusion coefficient D. Results from simulations, shown in Figure 4.8a, compare qualitatively very well with experiments with the only exception of the maximum position in the $x_p(w)$ and $\tau_p(w)$ curves: we observe a maximum for

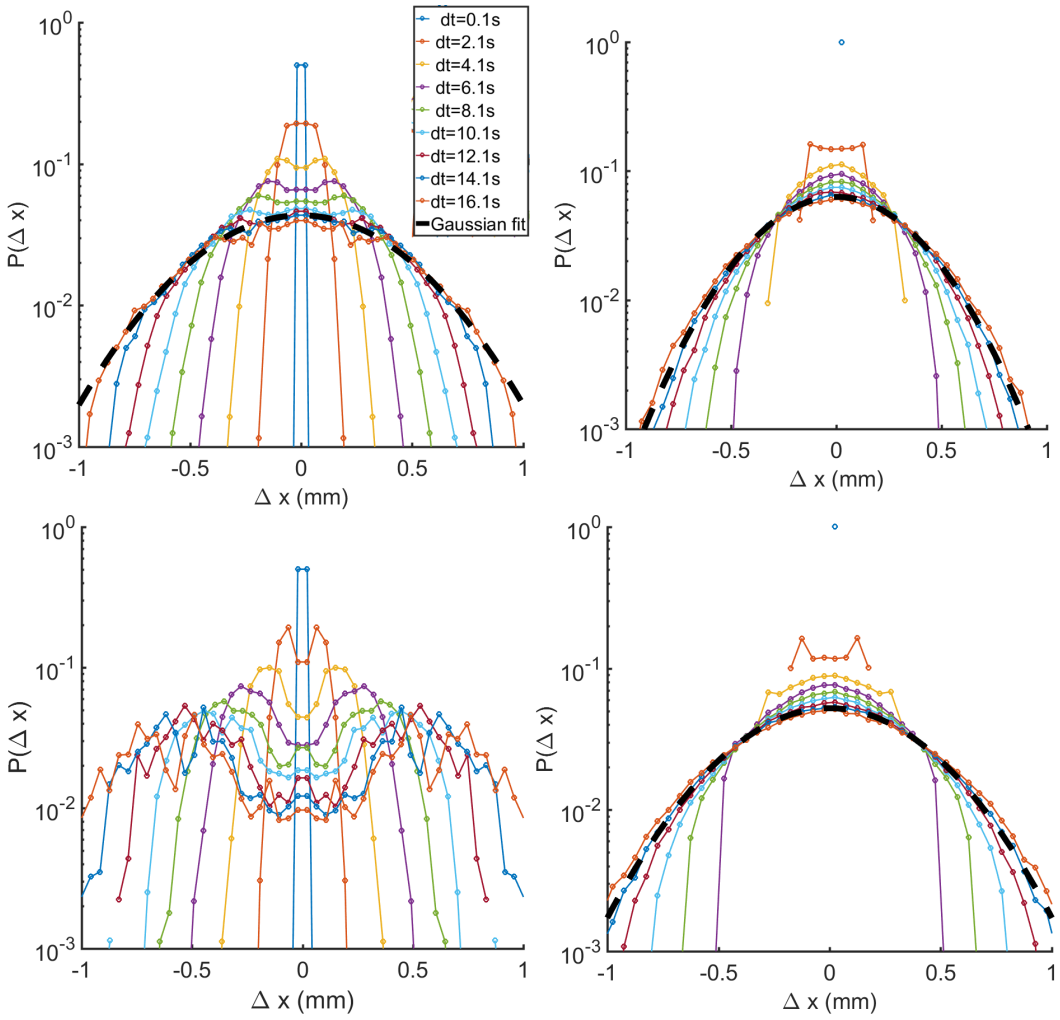

Figure 4.6: Distribution of displacement along the x axis $\Delta x(\Delta t)$ for $\Delta t = 0.1 \rightarrow 16$s in channels of two different widths. a,b) $\Delta x(\Delta t)$ for $w = 400\mu$m in experiments (left) and simulations (right).c,d) $\Delta x(\Delta t)$ for $w = 100\mu$m in experiments (left) and simulations (right).

$w = 50\,\mu$m in simulations and $w = 100\,\mu$m in experiments. The agreement is good also from a quantitative point of view, as shown Figure 4.10, with simulations overestimating the diffusivity in $w = 30\,\mu$m channel. This discrepancy may be due, as previously discussed, to the different scattering dynamics we observe in this narrow channel. Despite the differences in Figure 4.6, the simulations reproduce nicely swimmer motility along the x axis in the channels: since the only two mechanisms influencing the on-axis diffusivity of swimmers in simulations are rotational noise and random scattering, we want to understand the effect of each element on the motion of swimmers. Since the simulations reproduce accurately the experimental results, in the next section we will exploit the flexibility offered by numerical methods to gain some insights on the system and to study the results for channels of different length L.

4.3.3 Analysis of the simulations results

Using the simulations we can conclude that the non monotonic trend of diffusivity is entirely due to the presence of random scattering: in fact as we can see in Figure 4.10b, we see how simulations with no random scattering present a monotonically decreasing $D(w)$ curve. The introduction of random scattering causes diffusivity to drop by two orders of magnitude for $w = 30\,\mu$m, compared to a difference of 50% for $w = 400\,\mu$m. For $w = 30\,\mu$m, the only mechanism that causes algae to change sign of the swimming direction is random scattering. Even though head on collisions are more frequent in wider channels (and therefore the probability of random events), algae are much more likely to change direction through rotational diffusivity rather than as a consequence of interactions with walls, as they are very rare. In fact, considering a swimmer with no rotational diffusivity, scattering instantly (without sliding) at a fixed angle of 30° it would hit the walls only 6 times in a 3.6 mm channel when $w = 400\,\mu$m, compared to almost 200 times for $w = 30\,\mu$m. As an additional effect, the observed random scattering probability is actually higher for $w = 30\,\mu$m, explaining why in experiments swimmers in narrow channel show such a low diffusivity. We want now to evaluate the probability for a particle that, once it entered the channel from one of its two ends, manages to cross the whole length L leaving from the side opposite to its entrance point. We will call “success” an alga entering the channel from one end and swimming to the opposite side, while we will call a “failure” an alga entering and leaving the channel from the same side. Measuring success rate in experiments is not simple, it requires to track individual algae as long as it stays inside the channel, which is not always possible as tracking software may lose the particle before its exit. The tracking software may lose an alga when it overlaps for more than one frames with another bright feature on the experimental frames; this may happen as a consequence of collision with another alga inside the channel, or when other bright fea-

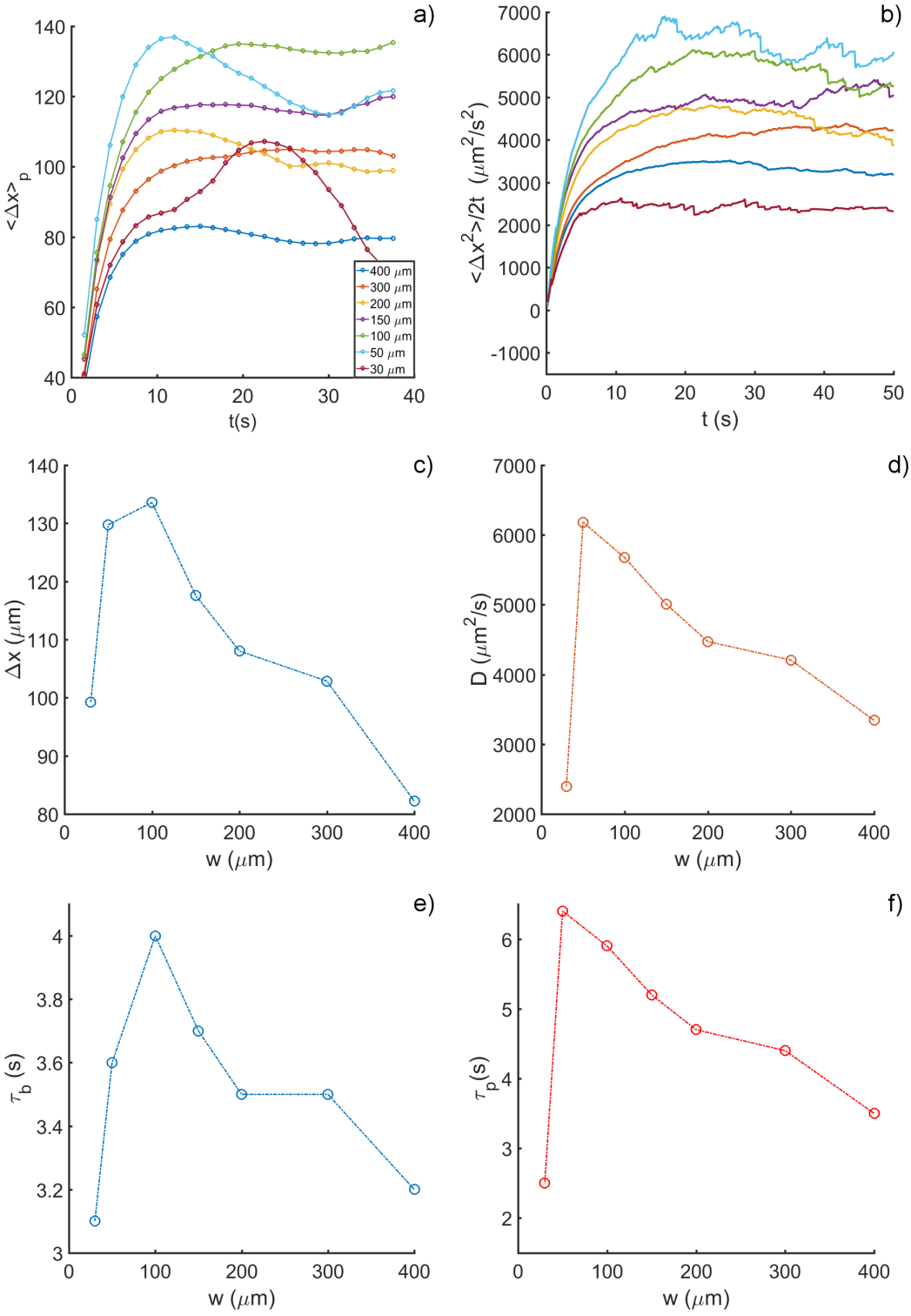

Figure 4.7: Characterisation of x axis motility in experiments. a) Mean displacement along the x axis $< \Delta x_w(t) >$ for channels of different width. b) Mean square displacement divided by $2t$ $< \Delta x_w^2(t) > /2t$ for channels of different width. c) Plateau value $x_p(w)$ of $< \Delta x_w(t) >$ as a function of channel width. d) Diffusivity $D(w)$ as a function of channel width. e) Persistence time $\tau_p(w)$ as a function of channel width. f) Ballistic time $\tau_b(w)$ as a function of channel width

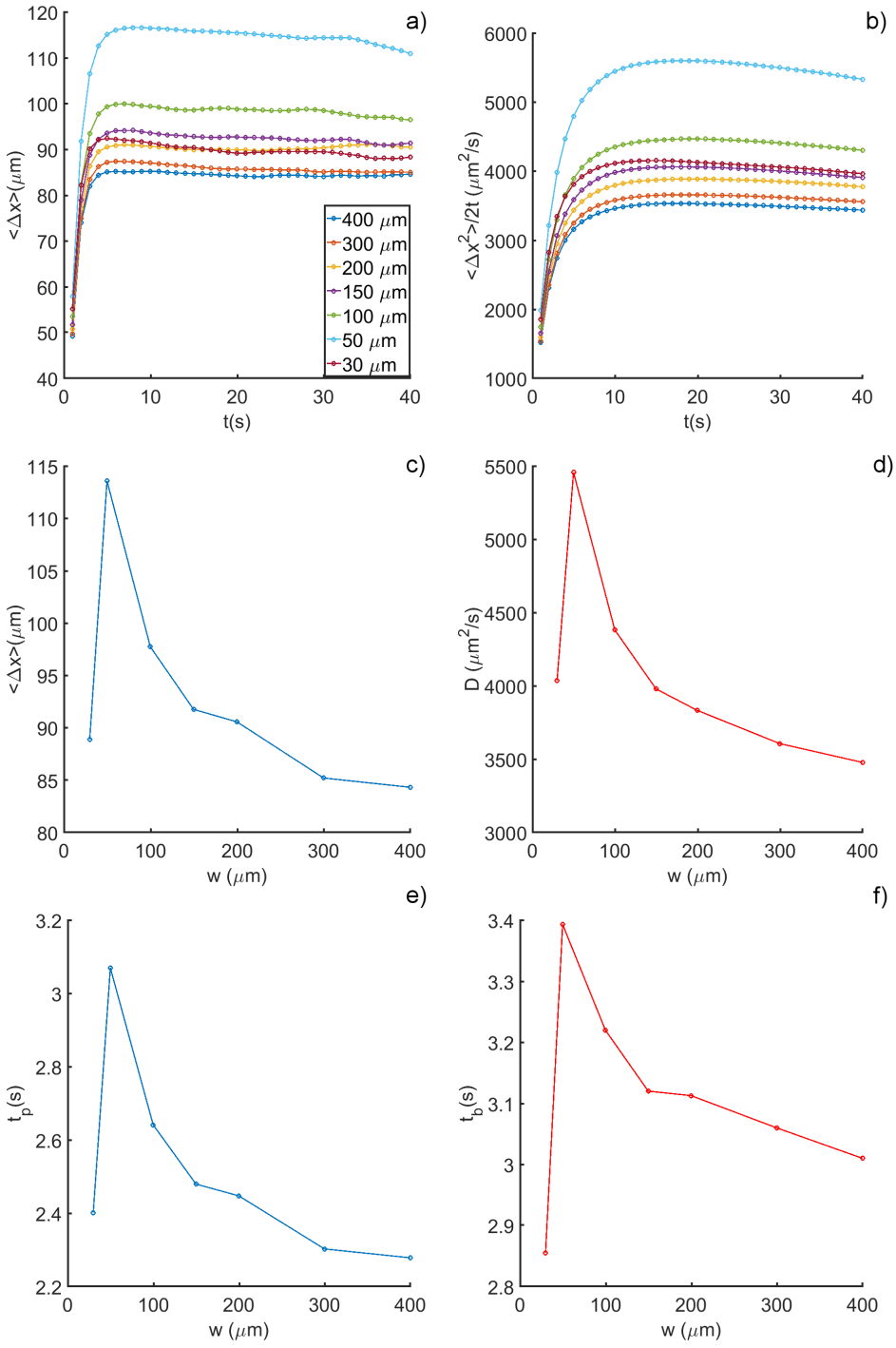

Figure 4.8: Characterisation of x axis motility in simulations. a) Mean displacement along the x axis $< \Delta x_w(t) >$ for channels of different width. b) Mean square displacement divided by $2t$ $< \Delta x_w^2(t) > /2t$ for channels of different width. c) Plateau value $x_p(w)$ of $< \Delta x_w(t) >$ as a function of channel width. d) Diffusivity $D(w)$ as a function of channel width. e) Persistence time $\tau_p(w)$ as a function of channel width. f) Ballistic time $\tau_b(w)$ as a function of channel width.

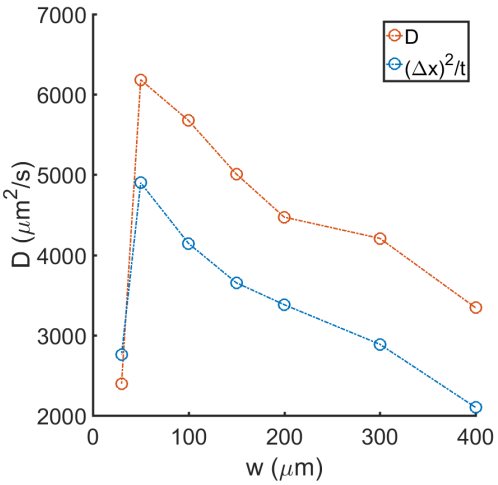

Figure 4.9: Comparison between $x_p(w)^2/2\tau_p(w)$ and the diffusion coefficient $D(w)$. We realise that $x_p(w)^2/2\tau_p(w)$ has the same dimension as a diffusion coefficient $D(w)$: we see that the trend for both quantities is qualitatively similar.

tures are present in the channel such as impurities. Although losing an alga in the middle of the channel is not very frequent, since we track the algae for thousands of frames, we end up having in our set a large number of interrupted trajectories that either begin after the alga has already entered, or end before it manages to get out, making it impossible to attribute success or failure to the trajectory. Furthermore, longer trajectories have higher chances to be interrupted and this results in a bias, leading to underestimate the number of successful trajectories, that are usually the longest. Also, experiments have a maximum observation time window (corresponding to the experiment duration) which leads once again to underestimate the success rate as shown in Figure 4.10a. For this reason we rely on the simulation results to evaluate the success rate, as it represents the experimental setup with a good degree of fidelity. The results for channels with L =3.6 mm long are shown in Figure 4.10d. Not surprisingly the shape of the curve, resembles the one we obtain for the diffusivity. The success rate, is basically a first passage problem and, for Brownian motion, it decreases as $1/L$. In Figure 4.10c we can observe how this is true for channels longer than $2mm$ while in shorter channels the success probability is nearly one, independently of the observation time window. In these situations particles swim in a straight line from entry to exit without ever changing direction. We see from Figure 4.8c that the persistence length for $w = 150\,\mu$m is $< x >_p \sim 95\,\mu$m: the diffusive scaling starts to match the simulation results around $L \sim 1000$ which is around ten times $< x >_p$.

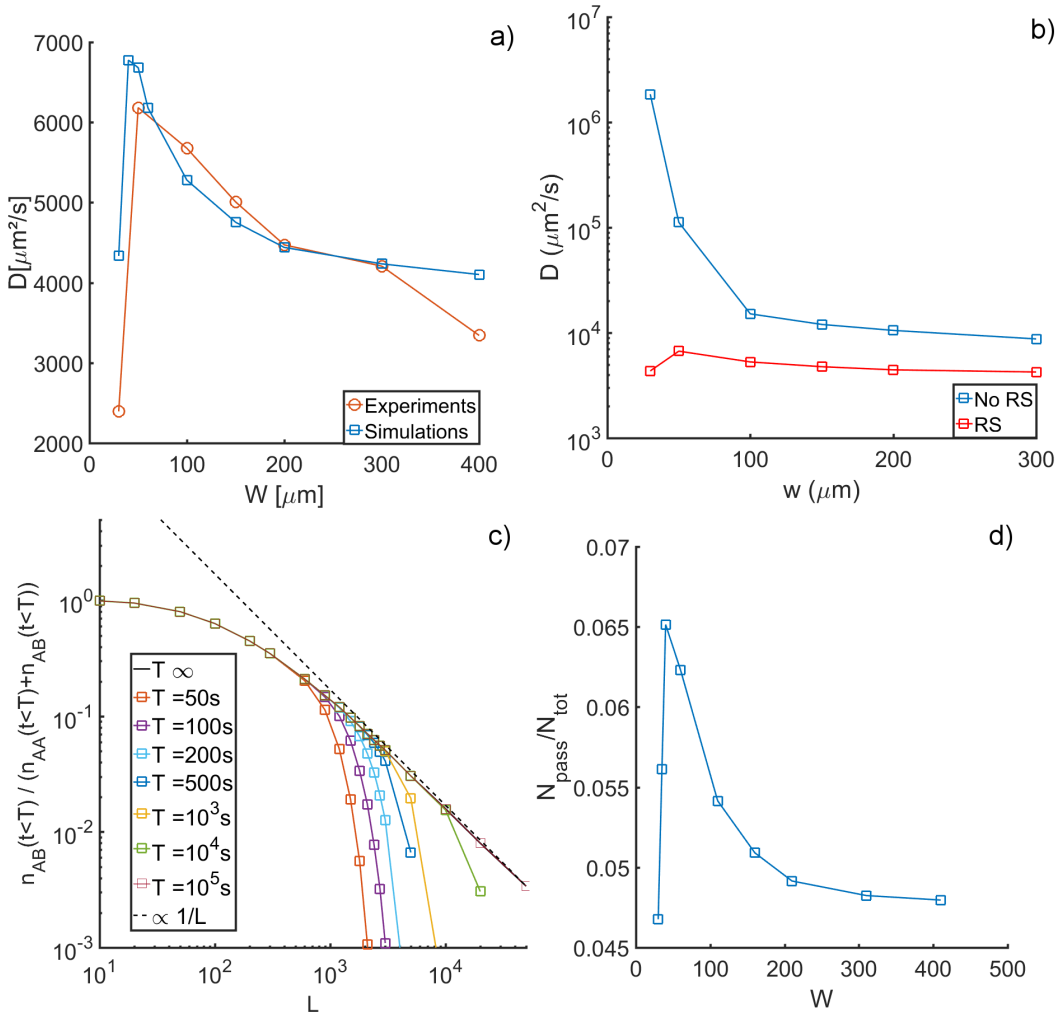

Figure 4.10: Characterisation of the diffusivity along the x axis and success rate in simulations. (a) Comparison of diffusivity in experiments and simulations (b) Diffusivity in simulations with and without random scattering (c) Probability of success for simulated trajectories in a simulated $w = 150\,\mu$m channel for different observation times (d) Probability of success for channels of different widths in simulations.

4.4 Conclusions

We present the first study on diffusion in straight narrow channels of CR as model puller-type swimmer. Algae motion can be described as a persistent random walk, ballistic on short time scale and diffusive as $t \to \infty$ but the presence of solid boundaries orient algae preferentially along channel axis or at a fixed angle with respect to it, causing the ballistic time to increase. Interaction with walls extends to an area of several flagellar lengths, as a residual alignment is present up to 100 μm away from the channel sides: this residual alignment may be due to the interaction with both walls at the same time, a mechanism that we do not explore in this thesis. Interacting with walls can cause algae to perform random scattering and switch swimming direction, so frequent interactions against the walls can reduce the ballistic time causing the diffusivity trend to be non monotonic, with an optimal value, in our case, for $w \sim 50\,\mu$m. We find that the scattering mechanisms introduced in Chapter 3 are crucial for understanding the behaviour of CR in straight channel, extending the validity of the work for different geometries.

Chapter 5

Chlamydomonas reinhardtii escape from a circular pool

5.1 Introduction

The study of diffusion out of a domain through small spots has been referred to as narrow escape problem (NEP) and traditionally [175], "it consists in calculating the first passage time of a Brownian particle $\bar{\tau}$ to a small absorbing region $\partial\Omega_\alpha$ on the otherwise reflecting boundary $\partial\Omega$ of a bounded domain Ω". The problem was first introduced by Baron Rayleigh in the context of acoustic in 1894 [176], in studying the flux out of a cavity resonator through a small hole. When describing the problem it can be useful to determine the escape time from the domain. For a uniform concentration of particles inside a 2D disc with radius R with a narrow aperture of size A so that $\Delta A = A/2\pi R \ll 1$, the expected value escape time τ can be written as [177]:

$$E(\tau) = \frac{R^2}{D}\left[\log\frac{1}{\Delta A} + \log 2 + \frac{1}{8} + O(\Delta A)\right] \tag{5.1}$$

where D is the diffusion coefficient of the particles. Surprisingly, $E(\tau)$ highly depends on the initial positions of the particles. When particles are perfectly ballistic, the mathematical approach to modelling the escape dynamics is completely different and is referred to as leaking chaotic systems (LCS)[178]. Interestingly this category of problems is also related to acoustic: almost 50 years after Baron Raleigh, Sabine [179] (and later measured experimentally by Joyce [180]) empirically obtained an equation for the residual sound intensity inside a room, showing that it decays exponentially with time and reaches an

inaudible level at time T_r, called reverberation time:

$$T_r \propto \frac{V}{cA} \tag{5.2}$$

where V is the room volume, c the speed of sound, and ΔA the sum of all the apertures in the room; it is worth noting that the position of apertures or the initial configuration of particles does not affect the reverberation time. The escape from a confined space through a narrow exit is ubiquitous in biology at all levels: from mRNA escaping through nucleus pores in the cell [181] to signalling in dendritic spines [182, 183] and microorganisms diffusing through porous media[184]. The description of motion of cells or other particles falls in the spectrum between pure Brownian diffusion (velocity autocorrelation time $\tau_c = 0$) and pure ballistic motion ($\tau_c \to \infty$). As seen previously, the motion of microswimmers is ballistic on short timescales and diffusive for longer observation times, so their escape dynamics will be more complicated than the two previous cases. In the past two years, two recent papers [171, 185], modelled the motion of swimming microorganisms as a dynamic billiard. In these articles it is shown how, as long as the LCS hypotheses hold [178], microfluidic devices with specific geometries can be used to trap, separate or control microorganisms depending on their scattering angle (see Figure 5.1). As we learned in Chapter 4, the motion of CR is influenced by the time intercurring between successive scattering, with ballistic time increasing for frequent collisions: if collisions are sufficiently frequent, their motion can be modelled with a billiard particle. We build a PDMS device with "small" (we will be discussing the meaning of small in the next section) circular chambers with two exits on its perimeter and we fill them with CR. In the next chapter, we will first study if the motion of algae inside such pools can be described as a billiard particle, and we will observe the emptying dynamics, aiming at identifying the "escape rate" of particles inside such pools.

5.2 Materials and methods

5.2.1 Experiments

Motion inside a circular pool

We build quasi 2D microfluidic channels as in previous chapters, with 8 arrays of circular pools (we will also refer to them as chambers or rooms) of radius $R = 100\,\mu$m with two exits located on the pool perimeter at an angular distance $\gamma = 90°$ from each other. Each array presents a different exit size w whose values are, in increasing order: 15, 20, 25, 30, 40, and 50 μm. An experimental image of the rooms arrays are shown in Figure 5.2a. Using the procedure described in Chapter 4 we punch the inlets on a direction

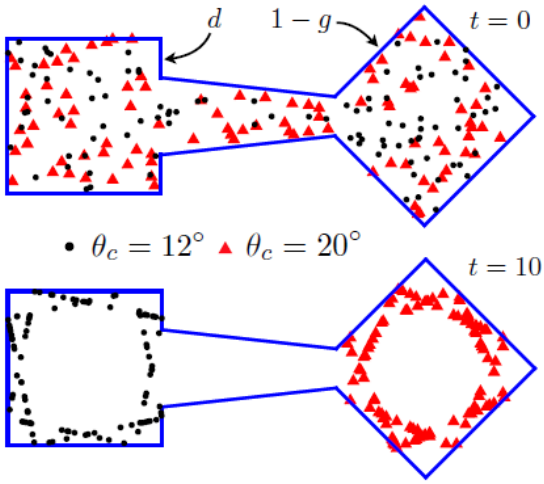

Figure 5.1: Example of separation of particles depending on their scattering angles θ_c. Starting from a uniform distribution of swimmers (a) in two chambers connected by a narrow channel, the two populations of swimmer spontaneously separate; at steady state, particles with $\theta_c = 12°$ (black circles) are preferably found in the left chamber, while swimmers with $\theta_c = 20°$ (red triangles) accumulate on the right chamber.

perpendicular to the orientation of the pools array, preventing flow to build up across the pools. We inject CR in the circuit and let them free to diffuse inside the circular chambers. We find the rooms' centre position $\mathbf{x_c}$ using the built-in MATLAB Hough transform, and record algae position $\mathbf{x}$ inside the pools. We define the CR to have entered a room if its distance from the center $\mathbf{r} = \mathbf{x} - \mathbf{x_c}$ is $|\mathbf{r}| < R + a/2$ where $a = 20\,\mu$m is equal to the average size of a CR body and flagella; similarly we consider an alga outside if $r > R + a/2$; chosing a different threshold, within reasonable limits, does not significantly affect the results. We record experimental videos using a 4x objective and a frame rate of 20 fps; we record $\sim 10^4$ trajectories for each exit size w. To characterise the effect of solid boundaries on the swimming behaviour of algae, we define the instantaneous swimming angle $\theta_{swim}(t)$ as the angle between $\mathbf{r}$ and the swimming direction $\mathbf{e}$ defined as the vector resulting from the linear fit of the tracked algal position between $t - 0.1$s and t; a swimming angle of 90° means that the alga is swimming perpendicular to the chamber radius while $\theta_{swim} = 0°$ and $\theta_{swim} = 180°$ indicate CR swimming respectively away or towards the room centre. Due to simmetry, we do not distinguish between cells swimming clockwise or counter-clockwise. Similarly to Chapter 4, we find that CR tend to swim aligned to the pool walls when sufficiently close to them and show no preferential swimming direction when their distance from the boundary is greater than 10μm ($|\mathbf{r}| < 90\,\mu$m) as visible in

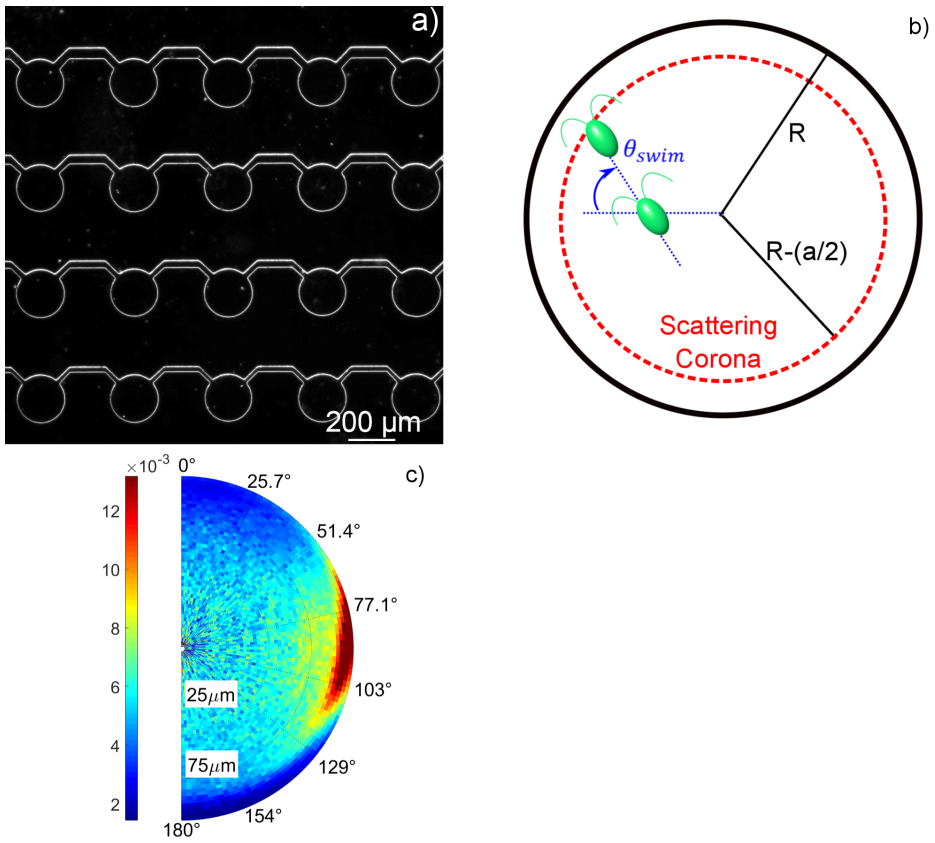

Figure 5.2: Examples of experimental setup and definition of experimental observables. a,b) Picture from experiments of arrays of pools with exit channels of different width. a) From top to bottom: w = 30,25,20,15 μm. b) Schematic of a circular pool (exits not considered): the black continuous line is the pool physical boundary, red dashed line represents the scattering corona (or interaction zone) set at a flagellar distance $a/2$ (where a=20 μm is the CR size consisting of body plus flagellar length). Swimming angle $\theta_{swim}(t)$ are the angle between the instantaneous swimming direction of an alga, measured by linearly fitting the alga position between $t-0.1$s (corresponding to three frames) and t and the vector connecting the pool centre to the alga position $\mathbf{x}(t)$. A swimming angle of 0° indicates the alga swimming away from the centre while 180° means the alga is moving towards the pool centre. c) Distribution of swimming angles as a function of distance d from the pool centres.

Figure 5.2c. As first reported in [174], this swimming angle distribution is reflected in a net accumulation of algae inside a narrow (~ 10 μm wide) annulus close to the chamber walls as shown in Figure 5.4a,b. We call this area (similarly to Chapters 3,4), the interaction zone (or scattering corona). We want to check if the description of surface scattering given in Chapter 3 still holds for concave surfaces, so we choose to measure angles analogous to the one measured when studying interactions with pillars. We define θ_{in}as the

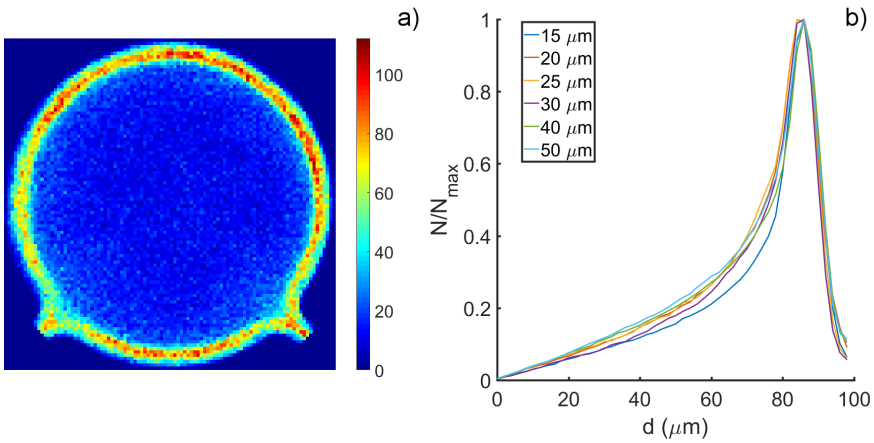

Figure 5.3: Accumulation of CR at the chamber walls. a) Heat map of tracked CR position **x** inside circular pools.b) Radial distribution of CR position inside the circular pool for different exit sizes.

swimming angle at the instant t_e when the the alga first enters the interaction zone as show in Figure 5.4a; $\theta_{out}$is analogously defined as $180° - \theta_{swim}$ 0.1s after the alga has left the scattering corona. From 5.4b, it is easy to see that the θ_{out} present a peak, with a maximum for $\theta^{\star}_{out} = 67.23°$, that we interpret as being given by deterministic scattering events. We expect this total probability distribution $p_T(\theta_{out})$ to consist of the weighted sum of a "deterministic" $p_d(\theta_{out})$ and a "random" $p_r(\theta_{out})$ distribution given by deterministic and random scattering. We isolate the random scattering events using the procedure explained in Chapter 3, and we calculate the deterministic θ_{out}distribution as:

$$p_d(\theta_{out}) = p_T(\theta_{out}) - p_r(\theta_{out}). \tag{5.3}$$

shown in Figure 5.4b. As shown in Chapter 4, CR swim almost in straight lines if the distance covered between two successive collisions with walls is comparable with the swimming persistence length. When leaving the interaction zone at $\theta^{\star}_{out}$, a CR would need to swim $\sim 60\,\mu$m before the next scattering, which is approximately the distance between two collisions in the $50\,\mu$m channel described in Chapter 4, where algae showed the highest ballistic time recorded in the experiments. To check how correct this approximation is, we measure β defined as the angle between the swimming direction at the exit point $\mathbf{e_{out}}$ from the interaction zone and the swimming direction at the entry point $\mathbf{e_{in}}$ at the successive entry in the scattering corona (see Figure 5.4a). Its distribution is peaked around zero as visible in Figure 5.4c, suggesting that algae trajectory between two scattering events is not significantly different from a straight line. As a consequence we expect that the majority of deterministic scatterings, will be followed

by an event with $\theta_{in} = \theta^{\star}_{out}$. To evaluate the proportion of collisions consequent to a deterministic interaction, we first need to determine the distribution of $p_r(\theta_{in})$ due to random events. We suppose that the θ_{in}distribution arising from random events is analogous to the one from a chamber uniformly filled with particles moving isotropically in all directions. For this case, it can be shown that the resulting incoming angle distribution is equal to $(4/\pi)\cos^2(\theta_{in})$. Supposing that "deterministic" peak is sufficiently far from $\theta_{in} = 0$, we suppose the random distribution to be $A\cos^2(\theta)$, and we choose A so that $p_T(0°) = p_r(0°)$. We extract the deterministic distribution as showed in 5.3 and we observe that both deterministic distributions (plotted in Figure 5.4b) present a peak for $\theta = 67.23°$ as we expected. If all the deterministic events would move in a straight line between scattering, we would find that the portion represented by p_d over the total distribution, would be the same for $\theta_{in}$and θ_{out}: what we find instead is that deterministic events represent 85.8% of $p_T(\theta_{out})$ and 55.7% of $p_T(\theta_{in})$ respectively, which means that the fraction of events where the ballistic approximation is not valid is ~ 30%. Finally we measure the angular distance α swum by a CR during a scattering interaction. From the α plot in Figure 5.4c we see that, as we have already observed for straight channels and pillar, even in concave geometries, cells briefly adhere and slide along the pool perimeter during scattering interactions. We see how the graph presents a peak around $\alpha = 20°$, corresponding to $\sim 40\,\mu$m which is equal to four CR body lengths: this angle will be important in the analysis of the escape dynamics in the following sections.

5.2.2 Simulations

We build a minimal model for the emptying dynamics of our experimental system. In our simulations we simulate 50k circular particles of radius a, representing the body and flagella of CR, each moving at a constant speed v drawn from a normal distribution centered around $v_0 = 84\,\mu$m/s (average speed measured from experiments) inside a round pool of radius $R = 10a$; since we use a dilute concentration of algae in our experiments, we neglect any interaction between the particles. We initiate our simulations with a random distribution of positions and swimming directions. Interactions with the walls are triggered when a particle centroid is at a distance a from the chamber boundary, and cause the alga to swim at a fixed angle $\theta^{*}_{out} = 67.23°$ (as measured in experiments) with the velocity vector away from the wall surface, in a simplified version of a deterministic scattering. As shown in Figure 5.5, particles radial distribution evolves from uniform to a net accumulation on the borders at steady state.

We define an arc of angular extent $\gamma_{exit} = w/R$, where w is the escape size, as the "exit region". To perform a direct escape, a particle must hit the exit region at a distance

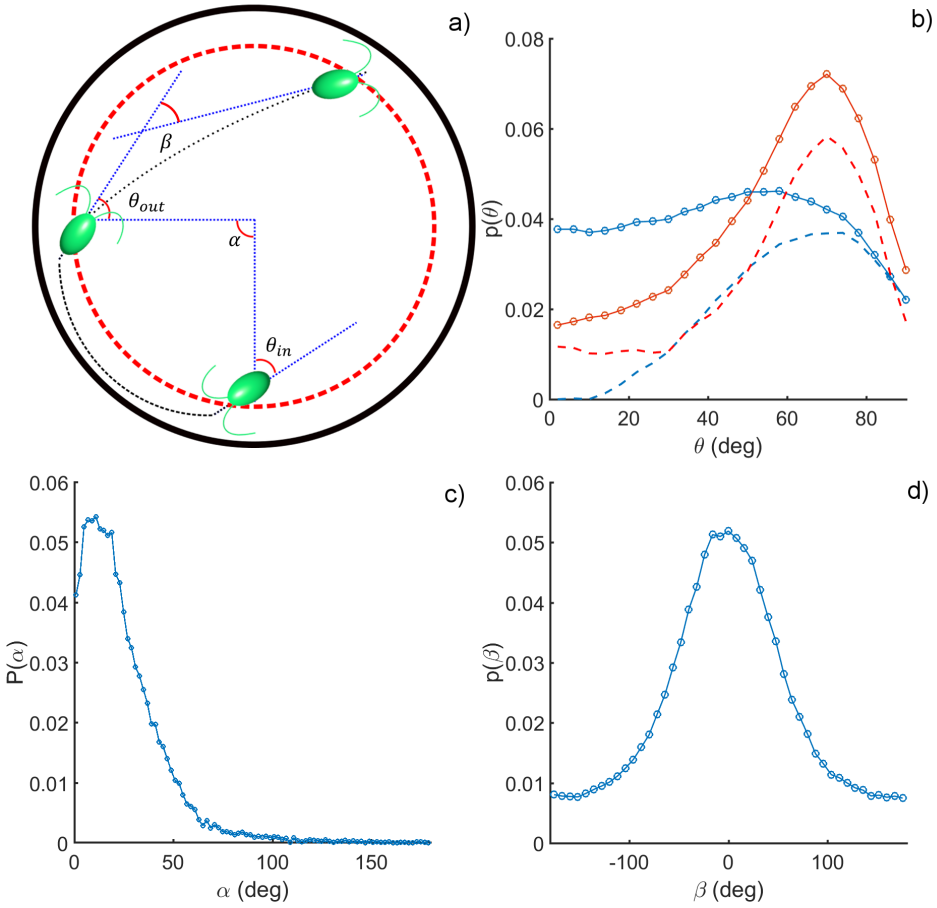

Figure 5.4: Angles measured in the experiments and scheme of the convention used to measure them. a) Schematic representation of a circular pool used in experiments. Black solid line represents the pool walls of radius $R = 100\,\mu$m, red dashed line is the scattering corona or interaction zone, defined as a circle concentric to the pool, with radius $R_c = 90\,\mu$m, equal to a flagellar length away from the pool's wall. The black dotted line represents the swimming trajectory of the drawn alga, while blue dotted line represents the alga direction at the enter/exit point inside/from the scattering corona (swimming direction) and the radii of the scattering corona at the enter/exit points, that we will refer to as scattering radius. θ_{in},θ_{out} the angle between the scattering radius and the swimming direction when algae enters/leave the scattering corona. α is the angular distance swum inside the scattering corona before exiting from it. β is the angle between the swimming direction at the exit point and the swimming direction at the entry point of the successive scattering. b)Total distribution (continuous) of θ_{in} (blue) and θ_{out} (red) measured in the experiments and deterministic distribution (dashed) of θ_{in} (blue) and θ_{out} (red) . c) Distribution of α from experiments. d) Distribution of β from experiments.

from the closest exit edge so that:

$$d_e > \frac{a}{\cos(\theta_{swim})}, \tag{5.4}$$

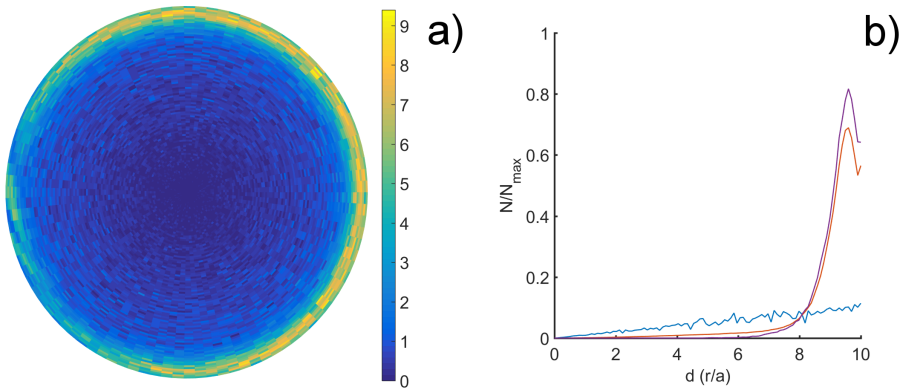

Figure 5.5: Particle distribution inside a simulated pool. a)Distribution of particle positions inside a simulated pool. b) Radial distribution of algae in simulations at $t = 0$s (blue), $t = 5$s (red) and $t = 20$s (purple).

where θ_{swim} is the swimming angle measured at the exit point. This condition translates the requirement that algae must able to swim through the channel entrance without touching the pool walls, because, as we showed in Chapter 3, steric interactions causes CR to move away from solid surfaces, effectively keeping algae inside the pool. If, after hitting the exit region, the swim through condition is met, the particle is removed from the system and counted as escaped.

5.3 Results

We want to study the time required for an alga to escape from a circular pool depending on exit size w. To characterise the escape dynamics, we study the survival probability of a particle inside a circular pool $s = N(t)/N(0)$, as defined in [178]: considering all algae to have entered a pool at $t = 0$, we record the fraction of particles who have not escaped at time t. Experimental results are presented in Figure 5.7a $N(t)/N(0)$ curves are well described by stretched exponentials of the form $N(t)/N(0) = \exp(-(\nu t)^k)$, where $k = 0.6517 \pm 0.0729$ for all w. In simulations we obtain that $N(t)/N(0)$ curve is a stretched exponential when we introduce a distribution of swimming speed v_0; if we use a single value for the swimming speed the emptying curve is a simple exponential ($k = 1$). In experiments we obtain this kind of decay because of the variability in the algal population (e.g. different swimming speed and rotational diffusivity among different individuals), but, even in experiments, we observe that the curves' tails resemble a simple exponential. We fit the curves with a stretched exponential and , by arbitrarily selecting a time threshold above which the emptying curves look linear in the semilog plot, we also fit them with a simple exponential. We find that values of ν obtained with these two meth-

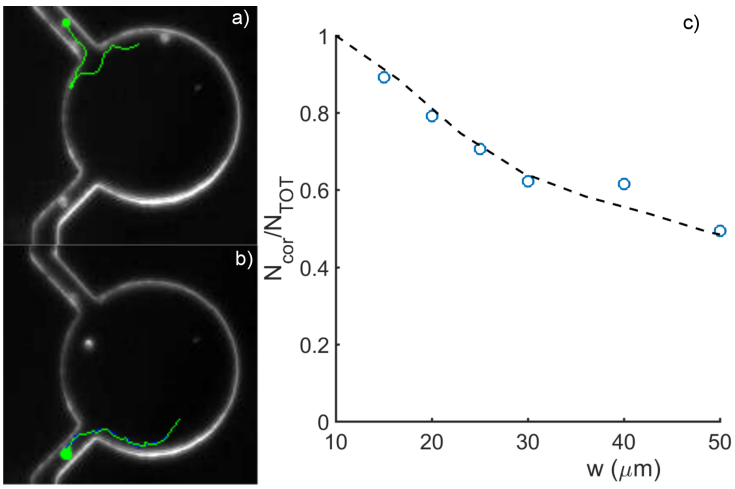

Figure 5.6: Example of corner escapes and fraction over total exits as a function of the channel width. a,b)Examples of corner escape trajectories: green lines represent the tracked trajectory of a CR performing a corner escape, and the green dot is the final position of the alga. In a) the alga slides along the surface as a consequence of a deterministic scattering while in b) the escape is a result of a random scattering. c) Fraction of corner escapes over the total number of exits as a function of the exit channel width w: blue circles are the data extracted from experiment while the black dashed line are the results of simulations.

ods are not significantly different quantitatively and show the same qualitative features, so we will treat ν as a simple exponential rate for simplicity. In Figure 5.7c, we plot the value of $\nu(w)$ for experiments. The curve presents an initial steep increase for w between 15 and 20 μm followed by a region with constant escape rate and a second steep increment for $w = 40\,\mu$m and a second final plateau for larger values. The results of simulations are totally different from a qualitative point of view, showing a strictly monitonically increasing trend with no plateaus and $\nu = 0$ for $w = 15\,\mu$m. Our model is not sufficient to reproduce the experimental dynamics we observe, this means we are missing a crucial ingredient in our simulations.

5.3.1 Corner escape

After a careful re-examination of the experimental videos, we observe that, besides swimming straight through the exit (*direct escapes*), algae are able to escape the pool by sliding along the surface and swim out of the chamber. We show two examples of this mechanism, that we will call *corner escapes*, in Figure 5.6a,b: in the figures, we see two algae which are swimming along the pool border, and then steer inside the exit channel. To quantify the number of similar escapes, we establish a criterion to distinguish between direct and corner escapes based on the angular distance α_{exit} covered by an escaped

alga inside the interaction zone prior to its escape. Defining γ_{exit} as w/R (representing the angular size of the exit), we consider an escape to be direct when $\alpha_{exit} < \gamma_{exit}/2$ and to be a corner escape otherwise. As shown in Figure 5.6c, we find that corner escapes are not a marginal effect, representing more than 40% of the escapes for all w and almost 100% for $w = 15\,\mu$m. To implement corner escapes in simulations, we define two "corner regions" of angular extent $\gamma_c = 25°$ (from the α maximum position, shown in Figure 5.4c) adjacent to both edges of the exit region. When a particle hits this zone, it has a certain probability p_c of escaping the pool, defined as:

$$p_c = p_0 \exp(-\frac{\Delta\gamma^2}{\sigma^2}) \tag{5.5}$$

where $\Delta\gamma$ is the angular distance between the impact point and the exit closest edge, while $\sigma = 20°$ is the standard deviation of the α experimental distribution. We choose a value of p_0 (the same for every exit width w) to match the experimental corner escape fraction. Adding this escape mechanism to our simulations causes the resulting $\nu(w)$ curve to match quantitatively the one obtained from the experiments except for $\nu(w = 15\,\mu\text{m})$: we believe that when w is smaller than twice the flagellar length of CR, the probability of performing a corner escape is reduced because algae cannot swim through the exit without touching the walls of the escape channel. We obtain the experimental escape rate by choosing a smaller value for p_0 (dashed curve in Figure 5.6). Since our model now reproduces so accurately the experimental results, we will exploit the flexibility offered by simulations to understand independently the effect of each escape mechanism. In Figure 5.7d we compare the $\nu(w)$ curves resulting from simulations where only corner ($\nu_c(w)$, red curve) or direct exits ($\nu_d(w)$, blue curve) are allowed to the results obtained when they're both present at the same time ($\nu_a(w)$,yellow curve). $\nu_c(w)$ given by corner escapes only, is a periodic curve oscillating around a mean value, while $\nu_d(w)$ given by direct exits only is equal to zero for $w = 15\,\mu$m and grows monotonically as w increases. We observe that in the w range of the first plateau (15-30 μm) $\nu_d(w)$ is less than $0.5\nu_c(w)$. The escape rates given by the two isolated mechanisms have the same value for $w \sim 40\,\mu$m while direct escapes are predominant for larger widths.

We define $\nu_{cd}(w)$ as: $\nu_{cd}(w) = \nu_c(w) + \nu_d(w)$, shown as the purple curve in Figure 5.7d. This curve is qualitatively similar to $\nu_a(w)$ while, from a quantitative point of view, we can see how the purple curve is always above the yellow one with the greatest discrepancy ($\nu_a(w) = 0.8\nu_{cd}(w)$) observed for $w = 50\,\mu$m. This fact indicates that the two escape mechanisms are correlated, even though we are not currently able to explain the reason. The results presented refer to simulations with no rotational diffusivity but

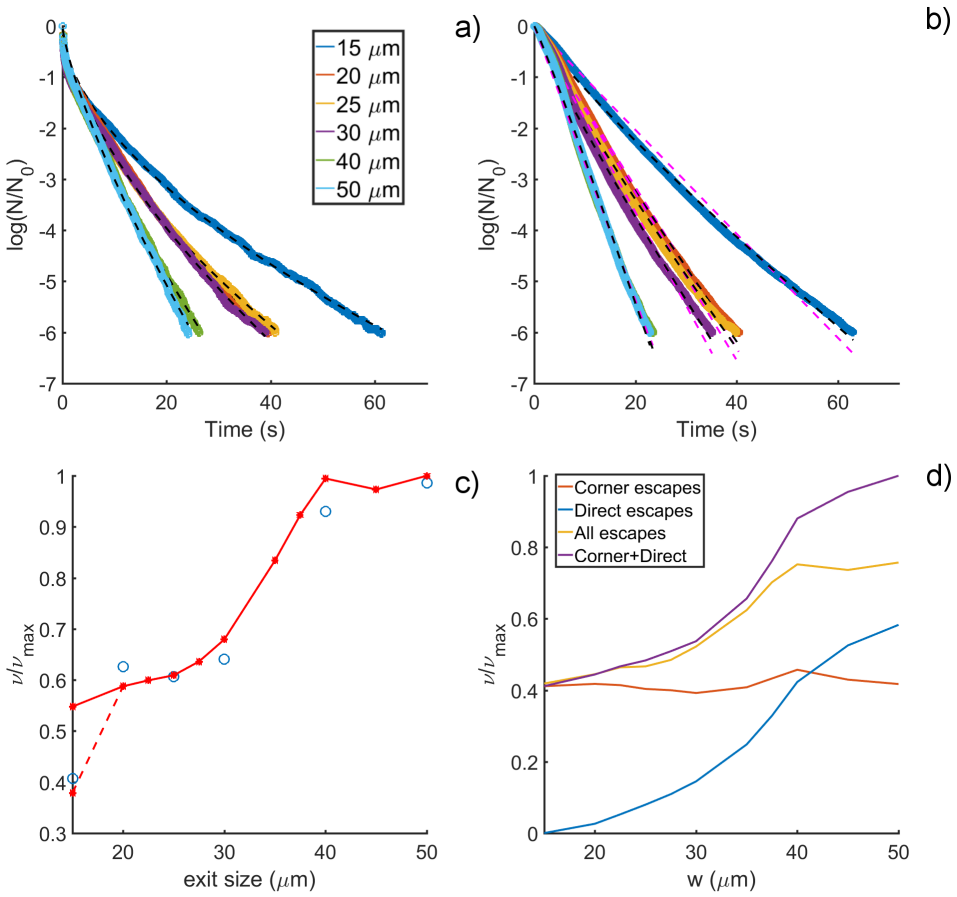

Figure 5.7: Emptying curves and escape rate as a function of w in experiments and simulations. a) $N(t)/N(0)$ for different channel widths in experiments; legend also apply to b). Black dashed lines represents a curve fitting with a stretched exponential of the form $\exp(-(\nu t)^k)$ .b) $N(t)/N(0)$ for different channel widths in simulations. Black dashed lines represents a curve fitting with a stretched exponential while magenta dashed lines are curves from a). c) $\nu(w)$ in experiments (blue circles) and simulations (red line and dot). Red dashed line represents $\nu(15\,\mu\text{m})$ when a different corner escape probability p_0 is used. d) $\nu(w)$ in simulations where only direct (blue) or corner escapes (red) are allowed; yellow curve shows results from simulations where both exit mechanisms are allowed and purple curve represents the sum of the red and blue curve.

qualitative features of the results are conserved for low level of noise. For higher noise figures, the $\nu(w)$ curve grows smoothly as w increases with no signs of plateaus. In the next section we will analyse the characteristics of the corner escape mechanism.

5.3.2 Corner escape simulation analysis

We perform simulations where direct escapes are not allowed and two corner regions are placed at a distance w (angular distance $\gamma_{exit} = w/R$). In Figure 5.8a, we show the corner

escape rate $\nu_c(w)$ of swimmers with different values of $\theta^\star_{out}$; all the resulting curves are periodic with different phases and amplitudes. In simulations with no noise, it can be easily shown that particles' scattering points against the pool borders are set at an angular distance $\gamma = 180° - 2\theta^\star_{out}$. We remember that each of the two corner regions extends on the pool perimeter for an arc of $\gamma_c = 25°$, so that, in the range of considered scattering angles, a particle cannot touch the same corner region on two consecutive hits. As a consequence a particle can touch each corner region only once, hence attempting to escape for a maximum of twice every round trip. From these considerations we expect to present a maximum in the $\nu_c(w)$ function when:

$$180° - 2\theta^\star_{out} = n(\gamma_c + \gamma_{exit}) \tag{5.6}$$

so each particle is bound to have one impact against each corner region every pool tour. This prediction is confirmed by Figure 5.8b,c showing the period and the position of the first maximum as for different $\theta^\star_{out}$. In Figure 5.8d, we plot the amplitude for different $\theta^\star_{out}$: the trend of this curve suggests there is a resonance-like mechanism. We do not currently understand Figure 5.8d highly irregular trend: although we run simulations with more than 50 thousands particles (which should in principle guarantee negligible error bars), we do not explore all the possible initial conditions, which may explain this unexpected behaviour.

5.3.3 CR and Anti-CR

Finally, we perform simulations with only direct escapes. As stated in Eq. 5.4, once $\theta^\star_{out}$ is fixed, algae have an "effective" exit size of $w - 2d_e$ (see (5.4) for d_e definition) so that there is a minimum exit width $2d_e$ that allows particles to escape. As a consequence, swimmers with lower scattering angles are able to escape through narrower exits. On the other hand, to find an exit placed on the perimeter, hitting the boundaries as often as possible can be advantageous. We compare the escape rate of a particle with scattering angle $\theta^\star_{out}$ (CR-like behaviour) against a particle that we will call "anti-CR" (ACR) with a fixed interaction angle of $90° - \theta^\star_{out}$. CR will have a higher scattering frequency, while ACR will have a larger effective exit size. In Figure 5.9 we plot the ratio $\nu_C(w)/\nu_{AC}(w)$ of the escape rates given by the two particles, for different $\theta^\star_{out}$; as $\theta^\star_{out}$ approaches 45° differences between the two species are less evident (by definition CR and ACR have the same scattering angle at 45°). As expected, ACR perform better for narrow exit sizes, where CR scattering angle does not allow direct escapes, while CR has the maximum relative efficiency in the intermediate range. For large w both types manage to escape after completing a lap around the pool, presenting a similar escape rate. It is worth not-

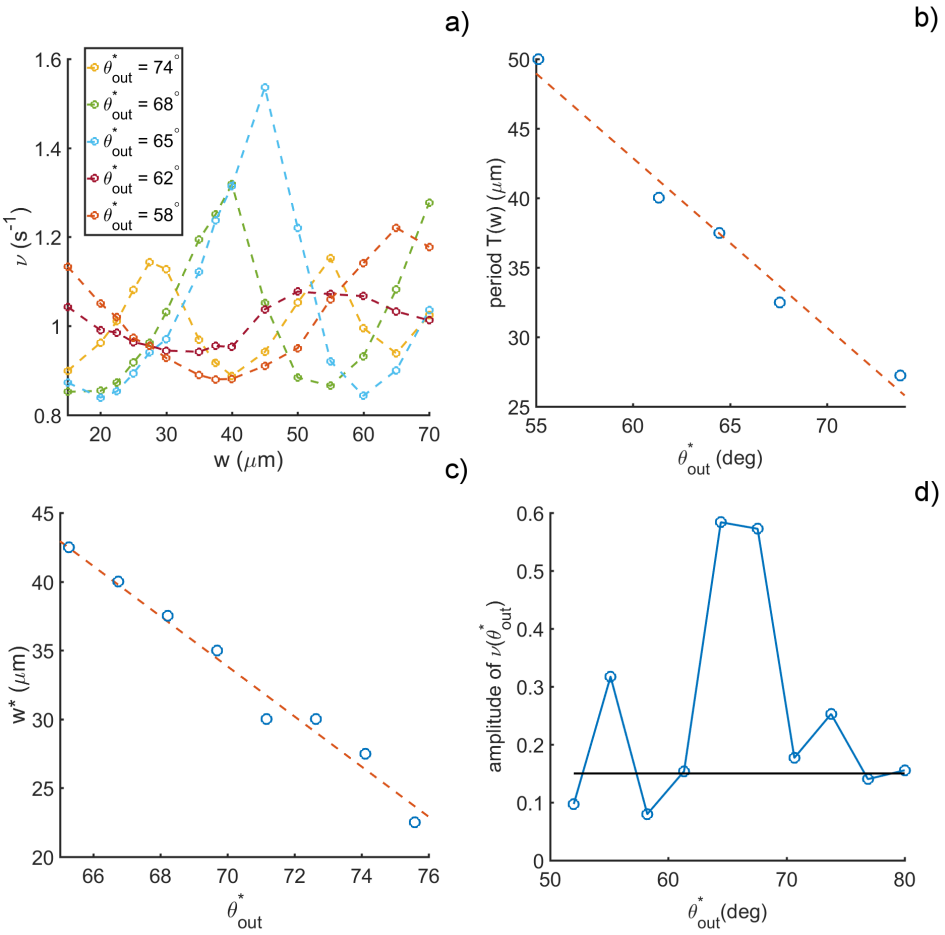

Figure 5.8: Results from simulations where only corner escapes are allowed. a)$\nu_c(w)$ for different values of $\theta^{\star}_{out}$. b)Period of $\nu_c(w)$ extracted by fitting the curves with a sinus function. c)Channel width w^* where we observe the first maximum in the $\nu_c(w)$ curves. d) Values of: max($\nu_c(w)$)-min($\nu_c(w)$) as a function of channel width w.

ing how the corner escape mechanism compensates the poor performances of CR for narrow apertures, conferring evolutive advantages to microorganisms such as *Chlamydomonas*, which need to navigate through complex environments.

5.4 Conclusions

We present the first experimental study of narrow escape problem for microorganisms in circular pools. We find that for sufficiently small pools, the behaviour of algae can be modelled as a dynamic billiard with particles scattering at fixed outgoing angles (as studied in [171, 185]) that we reproduce through a simple minimal model. The escape

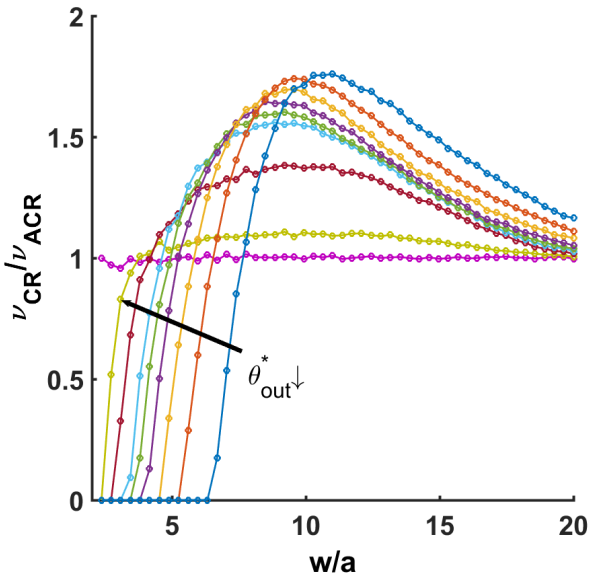

Figure 5.9: Escape rate of CR compared to its relative ACR $\nu(w)_{CR}/\nu(w)_{ACR}$. Escape rate for a CR-like particle $\nu(w)_{CR}$ with fixed scattering angle $\theta^{\star}_{out}$ compared to its relative ACR $\nu(w)_{ACR}$ with scattering angle $90^{\circ} - \theta^{\star}_{out}$.

rate dependence we find is not linear as predicted by LCS theory. Besides direct escapes, we find that a crucial role is played by the hydrodynamic forces (presented in Chapter 3) that cause swimming cells to adhere to the pool walls and guide them through the exit channel. The resulting dependence of the escape rate from these two mechanisms has a very distinctive trend, with very steep increases alternating to almost constant parts in the $\nu(w)$ curve. The coordination of these two mechanisms results in a more efficient escape in a broad range of exit sizes compared to the two isolated mechanisms. From the results of this chapter, we think a pool with exits of different width may be used to rectify the algal current, forcing microorganisms to migrate from the narrow to the wider exit side. In future work we should study the behaviour of CR for different pore sizes, more irregular pool geometries and when the "billiard" approximation is not valid. The effects studied in this work are clearly dominated by interactions with solid boundaries, so we expect the geometry of the pool to heavily affect the escape dynamics of cells.

Chapter 6

Conclusions

This thesis contains one of the few experimental study in a field, the interactions between puller type microswimmers and solid surfaces, that has been treated extensively in theoretical and numerical papers. Experiments in this field are hard to interpret as a multitude of forces are always acting on the system, and discriminating the effect of each one of them can be challenging. The work presented in Chapter 3 provides the first detailed study of the scattering mechanism of a puller-type microswimmer against curved surfaces. This chapter besides integrating and confirming in part the work of [52], provides new insights on the scattering against solid boundaries, introducing two new "regimes" of interactions: namely hydrodynamic and random. The first, takes places at a distance where steric interactions are not present and can be explained through far field hydrodynamics, while the second highlights the importance of the flagellar beating form that causes CR interaction front with walls to be time dependent and unstable, resulting in stochastic scattering results. Finally, for the first time, the spinning around its cell axis of CR is considered when describing cell-surface interactions. All of the results presented in this chapter not only provide insights on the considered phenomenon but must be used as building blocks when modelling more complicated systems. An example of this need is readily presented in Chapter 4, when studying a seemingly simple case as CR diffusion in straight channels. We find that the model we propose for interactions with pillars can be directly transferred to flat surfaces. We find that interactions with walls force algae to swim along a preferred direction when sufficiently close to walls; due to the noise in flagellar beating pattern, CR tend to deviate and lose memory of their previous direction after $\tau_p \sim 1$s. As a result, when collision frequency is of the order of τ_p^{-1}, algae deviate very little from the angle imposed by wall interactions, resulting in an increased ballistic time. On the other hand, frequent impacts against channel sides, result in a great number of random scatterings, which cause CR to reverse their swimming

direction and reduce their ballistic time. Our results show that there is an optimal value of confinement that maximises the effective diffusion coefficient of algae. We perform simulations of our system and we manage to reproduce both qualitatively and quantitatively the experimental results, showing that rotational diffusion and random scattering rate, are the only important parameters to model the experimental reality. The work presented in this chapter presents a way to control the diffusivity of CR using a simple geometry and a passive microfluidic device. We use the results of Chapter 4 to reproduce a microorganismal billiard and to study the escape rate from circular pools through narrow apertures in Chapter 5. In this chapter we prove that rotational diffusivity is negligible when studying the escape dynamics in "small" circular pools. Although the motion of algae can be modelled as an Hamiltonian billiard, we find that that the dependence of the escape rate from the aperture size is not linear as predicted from theory [178]. We individuate an escape mechanism from pools which is a direct consequence of the scattering dynamics of CR: when sliding along a solid surface, lubrication forces provide a torque that redirects CR towards the wall. As a result, if sliding past the escape channel corner, algae can be attracted inside the exit aperture and manage to escape: we call this escape mechanism "corner escape". The nature of this escape mechanism is highly stochastic and alter significantly the escape dynamics, especially for narrow aperture. We also show that corner escape is crucial in understanding our experimental results through a minimal model consisting of particles swimming in straight lines inside a circular pool.

The work in this thesis provides the first and most accurate dataset of puller swimmer interactions with solid surfaces with different geometrical properties, showing how every characteristic of the scattering dynamics is important to understand swimmer diffusion in complex media and provides examples of applications in microfluidics to control statistical properties of microswimmers' motion. Throughout the work presented in this thesis, we wanted to force CR moving in the plane of focus of microscope, in order to be able to detect change in velocity modulus and direction without the need to use three-dimensional optical techniques such as holography. To achieve this result, we used microfluidic devices whose thickness is of the same order of magnitude of CR cell diameter. The presence of the device upper and bottom surface surely affects the flow field of microorganisms along the channel's thickness due to the increased drag caused by two solid surfaces but we neglect, if any, the effects on the velocity field in the plane of focus. We are not aware of any experimental study on the effect of confinement on the flow field created by swimming microorganisms: we suggest a characterisation of the flow field as a function of the microchannel thickness could be extremely interesting for microswimmer community similarly to the "bulk" flow field measured in [39]. An-

other possible future development of the work in this thesis may follow from the results presented in Chapter 4: we believe that the validity of the results obtained for straight channels needs to be validated for more complicated geometries in order to build microfluidic devices that can be employed in the design of bioreactors or microorganisms sorters. The first geometry to study may be a zig zag or a channel with non constant width: these examples are fairly similar to the straight geometry, can provide further insights on the motion of microswimmers in complex geometries where irregularities are present, and may find direct application in the rectification or sorting of microorganisms. The results in Chapter 5 also need to be further investigated; in particular, we do not understand the correlation between the two individuated escape mechanisms and the resonance-like trend in the $\nu(w)$ curves for corner escapes when using different scattering angles. The results of this chapter suggest that a pool with escape sites of different size may cause a net flux of microorganisms due to the circuit asimmetry: for example two chambers, one on the left and one on the right, connected by an array of pools where the narrow exit is on the left and a wider exit on the right is likely to see the accumulation of microswimmers on the right hand side chamber.

Bibliography

[1] M. Contino, E. Lushi, I. Tuval, V. Kantsler, and M. Polin, "Microalgae scatter off solid surfaces by hydrodynamic and contact forces," *Physical Review Letters*, vol. 115, no. 25, pp. 258102–258102, 2015.

[2] R. Jeanneret, M. Contino, and M. Polin, "A brief introduction to the model microswimmer chlamydomonas reinhardtii," *The European Physical Journal Special Topics*, vol. 225, no. 11, pp. 2141–2156, 2016.

[3] C. Darwin, *On the Origin of Species*. London: John Murray, 1859.

[4] A. Boetius, A. M. Anesio, J. W. Deming, J. A. Mikucki, and J. Z. Rapp, "Microbial ecology of the cryosphere: sea ice and glacial habitats," *Nat Rev Micro*, vol. 13, no. 11, pp. 677–690, 2015.

[5] T. D. Brock and H. Freeze, "Thermus aquaticus gen. n. and sp. n., a nonsporulating extreme thermophile," *Journal of Bacteriology*, vol. 98, no. 1, pp. 289–297, 1969.

[6] G. Horneck, D. M. Klaus, and R. L. Mancinelli, "Space microbiology," *Microbiology and Molecular Biology Reviews : MMBR*, vol. 74, no. 1, pp. 121–156, 2010.

[7] R. Di Leonardo, L. Angelani, D. Dell'Arciprete, G. Ruocco, V. Iebba, S. Schippa, M. P. Conte, F. Mecarini, F. De Angelis, and E. Di Fabrizio, "Bacterial ratchet motors," *Proceedings of the National Academy of Sciences*, vol. 107, no. 21, pp. 9541–9545, 2010.

[8] B. D. Berg H. C., "Chemotaxis in escherichia coli analysed by three-dimensional tracking," *Nature*, vol. 239, no. 5374, pp. 500–504, 1972.

[9] G. H. Wadhams and J. P. Armitage, "Making sense of it all: bacterial chemotaxis," *Nat Rev Mol Cell Biol*, vol. 5, no. 12, pp. 1024–1037, 2004.

[10] E. Tamar, M. Koler, and A. Vaknin, "The role of motility and chemotaxis in the bacterial colonization of protected surfaces," vol. 6, p. 19616, 2016.

[11] E. M. Purcell, "Life at low reynolds number," *American Journal of Physics*, vol. 45, no. 1, pp. 3–11, 1977.

[12] H.-C. Flemming and J. Wingender, "The biofilm matrix," *Nature reviews. Microbiology*, vol. 8, no. 9, p. 623, 2010.

[13] M. Ordax, E. Marco-Noales, M. M. López, and E. G. Biosca, "Exopolysaccharides favor the survival of erwinia amylovora under copper stress through different strategies," *Research in Microbiology*, vol. 161, no. 7, pp. 549–555, 2010.

[14] D. G. Davies, M. R. Parsek, J. P. Pearson, B. H. Iglewski, J. t. Costerton, and E. Greenberg, "The involvement of cell-to-cell signals in the development of a bacterial biofilm," *Science*, vol. 280, no. 5361, pp. 295–298, 1998.

[15] B. Purevdorj, J. Costerton, and P. Stoodley, "Influence of hydrodynamics and cell signaling on the structure and behavior of pseudomonas aeruginosa biofilms," *Applied and environmental microbiology*, vol. 68, no. 9, pp. 4457–4464, 2002.

[16] T. Mah and G. O'Toole, "Mechanisms of biofilm resistance to antimicrobial agents," *Trends in microbiology*, vol. 9, no. 1, pp. 34–39, 2001.

[17] D. Davies, "Understanding biofilm resistance to antibacterial agents," *Nature Reviews. Drug discovery*, vol. 2, no. 2, pp. 114–122, 2003.

[18] P. S. Stewart, "Mechanisms of antibiotic resistance in bacterial biofilms," *International Journal of Medical Microbiology*, vol. 292, no. 2, pp. 107–113, 2002.

[19] J. Costerton, P. Stewart, and E. Greenberg, "Bacterial biofilms: A common cause of persistent infections," *Science*, vol. 284, no. 5418, pp. 1318–1322, 1999.

[20] D. M. Yebra, S. Kiil, and K. Dam-Johansen, "Antifouling technology—past, present and future steps towards efficient and environmentally friendly antifouling coatings," *Progress in Organic Coatings*, vol. 50, no. 2, pp. 75–104, 2004.

[21] M. A. Bighiu, A.-K. Eriksson-Wiklund, and B. Eklund, "Biofouling of leisure boats as a source of metal pollution," *Environmental Science and Pollution Research*, vol. 24, no. 1, pp. 997–1006, 2017.

[22] G. D. Bixler, A. Theiss, B. Bhushan, and S. C. Lee, "Anti-fouling properties of microstructured surfaces bio-inspired by rice leaves and butterfly wings," *Journal of Colloid and Interface Science*, vol. 419, pp. 114–133, 2014.

[23] X. Pu, G. Li, and H. Huang, "Preparation, anti-biofouling and drag-reduction properties of a biomimetic shark skin surface," *Biology Open*, 2016.

[24] C. Maggi, M. Paoluzzi, N. Pellicciotta, A. Lepore, L. Angelani, and R. Di Leonardo, "Generalized energy equipartition in harmonic oscillators driven by active baths," *Physical Review Letters*, vol. 113, no. 23, pp. 238303–238303, 2014.

[25] N. Koumakis, A. Lepore, C. Maggi, and R. Di Leonardo, "Targeted delivery of colloids by swimming bacteria," vol. 4, 2013.

[26] R. W. Fox, A. T. McDonald, and P. J. Pritchard, *Introduction to fluid mechanics*, vol. 5. John Wiley & Sons New York, 1998.

[27] E. Lauga and T. R. Powers, "The hydrodynamics of swimming microorganisms," *Reports on Progress in Physics*, vol. 72, no. 9, pp. 096601 0034–4885, 2009.

[28] A. T. Chwang and T. Y.-T. Wu, "Hydromechanics of low-reynolds-number flow. part 2. singularity method for stokes flows," *Journal of Fluid Mechanics*, vol. 67, no. 4, pp. 787–815, 1975.

[29] D. Papavassilou, *The reciprocal theorem and swimmer interactions.* PhD thesis, University of Warwick, 2016.

[30] G. J. Hancock, "The self-propulsion of microscopic organisms through liquids," *Proceedings of the Royal Society of London. Series A. Mathematical and Physical Sciences*, vol. 217, no. 1128, p. 96, 1953.

[31] A. T. Chwang and T. Y.-T. Wu, "Hydromechanics of low-reynolds-number flow. part 1. rotation of axisymmetric prolate bodies," *Journal of Fluid Mechanics*, vol. 63, no. 3, pp. 607–622, 1974.

[32] J. R. Blake, "A note on the image system for a stokeslet in a no-slip boundary," vol. 70, no. 2, pp. 303–310, 1971.

[33] L. H.A., "Zittingsverlag akad. v. wet," 1896.

[34] D. J. Griffiths, *Introduction to Electrodynamics (4th ed.).* Pearson, 2013.

[35] R. Cortez, "The method of regularized stokeslets," *SIAM Journal on Scientific Computing*, vol. 23, no. 4, pp. 1204–1225, 2001.

[36] R. Cortez, L. Fauci, and A. Medovikov, "The method of regularized stokeslets in three dimensions: analysis, validation, and application to helical swimming," *Physics of Fluids*, vol. 17, no. 3, 2005.

[37] J. Ainley, S. Durkin, R. Embid, P. Boindala, and R. Cortez, "The method of images for regularized stokeslets," *Journal of Computational Physics*, vol. 227, no. 9, pp. 4600–4616, 2008.

[38] K. Drescher, J. Dunkel, L. H. Cisneros, S. Ganguly, and R. E. Goldstein, "Fluid dynamics and noise in bacterial cell–cell and cell–surface scattering," *Proceedings of the National Academy of Sciences of the United States of America*, vol. 108, no. 27, pp. 10940–10945, 2011.

[39] K. Drescher, R. E. Goldstein, N. Michel, M. Polin, and I. Tuval, "Direct measurement of the flow field around swimming microorganisms," *Physical Review Letters*, vol. 105, no. 16, 2010.

[40] G. M. Whitesides, "The origins and the future of microfluidics," *Nature*, vol. 442, no. 7101, pp. 368–373, 2006.

[41] Y. Xia and G. M. Whitesides, "Soft lithography," *Angewandte Chemie International Edition*, vol. 37, no. 5, pp. 550–575, 1998.

[42] R. A. Kellogg, R. Gómez-Sjöberg, A. A. Leyrat, and S. Tay, "High-throughput microfluidic single-cell analysis pipeline for studies of signaling dynamics," *Nat. Protocols*, vol. 9, no. 7, pp. 1713–1726, 2014.

[43] C.-W. Chang, C.-C. Peng, W.-H. Liao, and Y.-C. Tung, "Polydimethylsiloxane slipchip for mammalian cell culture applications," *Analyst*, vol. 140, no. 21, pp. 7355–7365, 2015.

[44] A. J. Blake, T. M. Pearce, N. S. Rao, S. M. Johnson, and J. C. Williams, "Multilayer pdms microfluidic chamber for controlling brain slice microenvironment," *Lab Chip*, vol. 7, pp. 842–849, 2007.

[45] E. K. Sackmann, A. L. Fulton, and D. J. Beebe, "The present and future role of microfluidics in biomedical research," *Nature*, vol. 507, no. 7491, pp. 181–189, 2014.

[46] R. Rusconi, M. Garren, and R. Stocker, "Microfluidics expanding the frontiers of microbial ecology," *Annual review of biophysics*, vol. 43, pp. 65–91, 2014.

[47] C. Bechinger, R. Di Leonardo, H. Löwen, C. Reichhardt, G. Volpe, and G. Volpe, "Active particles in complex and crowded environments," *Reviews of Modern Physics*, vol. 88, no. 4, pp. 045006–, 2016.

[48] ElveFlow, "How to build a microfluidic device."

[49] P. Galajda, J. Keymer, P. Chaikin, and R. Austin, "A wall of funnels concentrates swimming bacteria," *Journal of Bacteriology*, vol. 189, no. 23, pp. 8704–8707, 2007.

[50] E. Lushi, H. Wioland, and R. E. Goldstein, "Fluid flows created by swimming bacteria drive self-organization in confined suspensions," *Proceedings of the National Academy of Sciences*, vol. 111, no. 27, pp. 9733–9738, 2014.

[51] C. Maggi, J. Simmchen, F. Saglimbeni, J. Katuri, M. Dipalo, F. De Angelis, S. Sanchez, and R. Di Leonardo, "SelfâĂŘassembly of micromachining systems powered by janus micromotors," *Small*, vol. 12, no. 4, pp. 446–451, 2016.

[52] V. Kantsler, J. Dunkel, M. Polin, and R. E. Goldstein, "Ciliary contact interactions dominate surface scattering of swimming eukaryotes," *Proceedings of the National Academy of Sciences of the United States of America*, vol. 110, no. 4, pp. 1187–1192, 2013.

[53] S. Elizabeth Hulme, W. R. DiLuzio, S. S. Shevkoplyas, L. Turner, M. Mayer, H. C. Berg, and G. M. Whitesides, "Using ratchets and sorters to fractionate motile cells of escherichia coli by length," *Lab on a Chip*, vol. 8, no. 11, pp. 1888–1895, 2008.

[54] H. Wioland, F. G. Woodhouse, J. Dunkel, J. O. Kessler, and R. E. Goldstein, "Confinement stabilizes a bacterial suspension into a spiral vortex," *Physical review letters*, vol. 110, no. 26, p. 268102, 2013.

[55] H. Wioland, F. G. Woodhouse, J. Dunkel, and R. E. Goldstein, "Ferromagnetic and antiferromagnetic order in bacterial vortex lattices," *Nature physics*, vol. 12, no. 4, pp. 341–345, 2016.

[56] A. Bricard, J.-B. Caussin, N. Desreumaux, O. Dauchot, and D. Bartolo, "Emergence of macroscopic directed motion in populations of motile colloids," *arXiv preprint arXiv:1311.2017*, 2013.

[57] S. Park, H. Hwang, S.-W. Nam, F. Martinez, R. H. Austin, and W. S. Ryu, "Enhanced caenorhabditis elegans locomotion in a structured microfluidic environment," *PLoS ONE*, vol. 3, no. 6, p. e2550, 2008.

[58] S. Jung, "Caenorhabditis elegans swimming in a saturated particulate system," *Physics of Fluids*, vol. 22, no. 3, pp. 031903

[59] T. Majmudar, E. E. Keaveny, J. Zhang, and M. J. Shelley, "Experiments and theory of undulatory locomotion in a simple structured medium," *Journal of the Royal Society Interface*, vol. 9, no. 73, pp. 1809–1823, 2012.

[60] S. Johari, V. Nock, M. M. Alkaisi, and W. Wang, "On-chip analysis of c. elegans muscular forces and locomotion patterns in microstructured environments," *Lab on a Chip*, vol. 13, no. 9, pp. 1699–1707, 2013.

[61] N. A. Licata, B. Mohari, C. Fuqua, and S. Setayeshgar, "Diffusion of bacterial cells in porous media," *Biophysical Journal*, vol. 110, no. 1, pp. 247–257, 2016.

[62] M. Raatz, M. Hintsche, M. Bahrs, M. Theves, and C. Beta, "Swimming patterns of a polarly flagellated bacterium in environments of increasing complexity," *The European Physical Journal Special Topics*, vol. 224, no. 7, pp. 1185–1198, 2015.

[63] C. R. Williams and M. A. Bees, "A tale of three taxes: photo-gyro-gravitactic bioconvection," *Journal of Experimental Biology*, vol. 214, no. 14, pp. 2398–2408

[64] J. E. Sosa-Hernández, M. Santillán, and J. Santana-Solano, "Motility of escherichia coli in a quasi-two-dimensional porous medium," *Physical Review E*, vol. 95, no. 3, pp. 032404–, 2017.

[65] H. Mao, P. S. Cremer, and M. D. Manson, "A sensitive, versatile microfluidic assay for bacterial chemotaxis," *Proceedings of the National Academy of Sciences*, vol. 100, no. 9, pp. 5449–5454, 2003.

[66] J. Seymour, T. Ahmed, and R. Stocker, "A microfluidic chemotaxis assay to study microbial behavior in diffusing nutrient patches," *Limnology and Oceanography: Methods*, vol. 6, no. 9, pp. 477–488, 2008.

[67] T. Long and R. M. Ford, "Enhanced transverse migration of bacteria by chemotaxis in a porous t-sensor," *Environmental Science & Technology*, vol. 43, no. 5, pp. 1546–1552, 2009.

[68] R. Singh and M. S. Olson, "Transverse chemotactic migration of bacteria from high to low permeability regions in a dual permeability microfluidic device," *Environmental Science & Technology*, vol. 46, no. 6, pp. 3188–3195, 2012.

[69] M. S. Olson, R. M. Ford, J. A. Smith, and E. J. Fernandez, "Mathematical modeling of chemotactic bacterial transport through a two-dimensional heterogeneous porous medium," *Bioremediation Journal*, vol. 10, no. 1-2, pp. 13–23, 2006.

[70] W. M. Durham, O. Tranzer, A. Leombruni, and R. Stocker, "Division by fluid incision: Biofilm patch development in porous media," *Physics of Fluids*, vol. 24, no. 9, p. 091107, 2012.

[71] W. M. Durham, E. Climent, and R. Stocker, "Gyrotaxis in a steady vortical flow," *Physical Review Letters*, vol. 106, no. 23, pp. 238102–238102, 2011.

[72] Y.-H. M. Chan and W. F. Marshall, "Scaling properties of cell and organelle size," *Organogenesis*, vol. 6, no. 2, pp. 88–96, 2010.

[73] W. F. Marshall, "Origins of cellular geometry," *Bmc Biology*, vol. 9, pp. 57–57, 2011.

[74] N. W. Goehring and A. A. Hyman, "Organelle growth control through limiting pools of cytoplasmic components," *Current Biology*, vol. 22, no. 9, pp. R330–R339, 2012.

[75] G. Allorent, R. Tokutsu, T. Roach, G. Peers, P. Cardol, J. Girard-Bascou, D. Seigneurin-Berny, D. Petroutsos, M. Kuntz, C. Breyton, F. Franck, F.-A. Wollman, K. K. Niyogi, A. Krieger-Liszkay, J. Minagawa, and G. Finazzi, "A dual strategy to cope with high light in *Chlamydomonas reinhardtii*," *Plant Cell*, vol. 25, no. 2, pp. 545–557, 2013.

[76] Y. Allahverdiyeva, M. Suorsa, M. Tikkanen, and E.-M. Aro, "Photoprotection of photosystems in fluctuating light intensities," *Journal of Experimental Botany*, vol. 66, no. 9, pp. 2427–2436, 2015.

[77] A. N. Dodd, J. Kusakina, A. Hall, P. D. Gould, and M. Hanaoka, "The circadian regulation of photosynthesis," *Photosynthesis Research*, vol. 119, no. 1-2, pp. 181–190, 2014.

[78] Y. Niwa, T. Matsuo, K. Onai, D. Kato, M. Tachikawa, and M. Ishiura, "Phase-resetting mechanism of the circadian clock in *Chlamydomonas reinhardtii*," *Proceedings of the National Academy of Sciences of the United States of America*, vol. 110, no. 33, pp. 13666–13671, 2013.

[79] W. J. Snell, "Cell-cell interactions in *Chlamydomonas*," *Annual Review of Plant Physiology and Plant Molecular Biology*, vol. 36, pp. 287–315, 1985.

[80] S. S. Merchant, S. E. Prochnik, O. Vallon, E. H. Harris, S. J. Karpowicz, G. B. Witman, A. Terry, A. Salamov, L. K. Fritz-Laylin, L. Marechal-Drouard, W. F. Marshall, L.-H. Qu, D. R. Nelson, A. A. Sanderfoot, M. H. Spalding, V. V. Kapitonov, Q. Ren, P. Ferris, E. Lindquist, H. Shapiro, S. M. Lucas, J. Grimwood, J. Schmutz, P. Cardol, H. Cerutti, G. Chanfreau, C.-L. Chen, V. Cognat, M. T. Croft, R. Dent, S. Dutcher, E. Fernandez, H. Fukuzawa, D. Gonzalez-Ballester, D. Gonzalez-Halphen, A. Hallmann, M. Hanikenne, M. Hippler, W. Inwood, K. Jabbari, M. Kalanon, R. Kuras, P. A. Lefebvre, S. D. Lemaire, A. V. Lobanov, M. Lohr, A. Manuell, I. Meier, L. Mets, M. Mittag, T. Mittelmeier, J. V. Moroney, J. Moseley, C. Napoli, A. M. Nedelcu,

K. Niyogi, S. V. Novoselov, I. T. Paulsen, G. Pazour, S. Purton, J.-P. Ral, D. M. Riano-Pachon, W. Riekhof, L. Rymarquis, M. Schroda, D. Stern, J. Umen, R. Willows, N. Wilson, S. L. Zimmer, J. Allmer, J. Balk, K. Bisova, C.-J. Chen, M. Elias, K. Gendler, C. Hauser, M. R. Lamb, H. Ledford, J. C. Long, J. Minagawa, M. D. Page, J. Pan, W. Pootakham, S. Roje, A. Rose, E. Stahlberg, A. M. Terauchi, P. Yang, S. Ball, C. Bowler, C. L. Dieckmann, V. N. Gladyshev, P. Green, R. Jorgensen, S. Mayfield, B. Mueller-Roeber, S. Rajamani, R. T. Sayre, P. Brokstein, I. Dubchak, D. Goodstein, L. Hornick, Y. W. Huang, J. Jhaveri, Y. Luo, D. Martinez, W. C. A. Ngau, B. Otillar, A. Poliakov, A. Porter, L. Szajkowski, G. Werner, K. Zhou, I. V. Grigoriev, D. S. Rokhsar, and A. R. Grossman, "The *Chlamydomonas* genome reveals the evolution of key animal and plant functions," *Science*, vol. 318, no. 5848, pp. 245–251, 2007.

[81] D. B. S. Elizabeth H. Harris and G. B. Witman., *The Chlamydomonas Sourcebook (Second Edition)*. Academic Press, San Diego, CA, 2009.

[82] T. J. Pedley and J. O. Kessler, "Hydrodynamic phenomena in suspensions of swimming microorganisms," *Annual Review of Fluid Mechanics*, vol. 24, pp. 313–358, 1992.

[83] K. W. Foster and R. D. Smyth, "Light antennas in phototactic algae," *Microbiological Reviews*, vol. 44, no. 4, pp. 572–630, 1980.

[84] D. G. W. Roberts, M. R. Lamb, and C. L. Dieckmann, "Characterization of the eye2 gene required for eyespot assembly in *Chlamydomonas reinhardtii*," *Genetics*, vol. 158, no. 3, pp. 1037–1049, 2001.

[85] K. Komsic, L. Wöstehoff, and B. Becker, "The contractile vacuole as a key regulator of cellular water flow in chlamydomonas reinhardtii," *Eukaryotic cell*, vol. 13, no. 11, pp. 1421–1430, 2014.

[86] J. L. Salisbury, M. A. Sanders, and L. Harpst, "Flagellar root contraction and nuclear-movement during flagellar regeneration in *Chlamydomonas-reinhardtii*," *Journal of Cell Biology*, vol. 105, no. 4, pp. 1799–1805, 1987.

[87] G. J. Pazour, N. Agrin, J. Leszyk, and G. B. Witman, "Proteomic analysis of a eukaryotic cilium," *Journal of Cell Biology*, vol. 170, no. 1, pp. 103–113, 2005.

[88] L. Vincensini, T. Blisnick, and P. Bastin, "1001 model organisms to study cilia and flagella," *Biology of the Cell*, vol. 103, no. 3, pp. 109–130, 2011.

[89] C. R. Wood, K. Huang, D. R. Diener, and J. L. Rosenbaum, "The cilium secretes bioactive ectosomes," *Current Biology*, vol. 23, no. 10, pp. 906–911, 2013.

[90] D. R. Mitchell and M. Nakatsugawa, "Bend propagation drives central pair rotation in *Chlamydomonas reinhardtii* flagella," *Journal of Cell Biology*, vol. 166, no. 5, pp. 709–715, 2004.

[91] T. Niedermayer, B. Eckhardt, and P. Lenz, "Synchronization, phase locking, and metachronal wave formation in ciliary chains," *Chaos*, vol. 18, no. 3, pp. 037128–037128, 2008.

[92] I. H. Riedel-Kruse, A. Hilfinger, J. Howard, and F. Juelicher, "How molecular motors shape the flagellar beat," *Hfsp Journal*, vol. 1, no. 3, pp. 192–208, 2007.

[93] U. Ruffer and W. Nultsch, "High-speed cinematographic analysis of the movement of *Chlamydomonas*," *Cell Motility and the Cytoskeleton*, vol. 5, no. 3, pp. 251–263, 1985.

[94] P. V. Bayly, B. L. Lewis, P. S. Kemp, R. B. Pless, and S. K. Dutcher, "Efficient spatiotemporal analysis of the flagellar waveform of *Chlamydomonas* reinhardtii," *Cytoskeleton*, vol. 67, no. 1, pp. 56–69, 2010.

[95] P. V. Bayly, B. L. Lewis, E. C. Ranz, R. J. Okamoto, R. B. Pless, and S. K. Dutcher, "Propulsive forces on the flagellum during locomotion of *Chlamydomonas reinhardtii*," *Biophysical Journal*, vol. 100, no. 11, pp. 2716–2725, 2011.

[96] H. Kurtuldu, J. S. Guasto, K. A. Johnson, and J. P. Gollub, "Enhancement of biomixing by swimming algal cells in two-dimensional films," *Proceedings of the National Academy of Sciences*, vol. 108, no. 26, pp. 10391–10395, 2011.

[97] T. Yagi, I. Minoura, A. Fujiwara, R. Saito, T. Yasunaga, M. Hirono, and R. Kamiya, "An axonemal dynein particularly important for flagellar movement at high viscosity - implications from a new *Chlamydomonas* mutant deficient in the dynein heavy chain gene dhc," *Journal of Biological Chemistry*, vol. 280, no. 50, pp. 41412–41420, 2005.

[98] P. Bayly and K. Wilson, "Analysis of unstable modes distinguishes mathematical models of flagellar motion," *Journal of the Royal Society Interface*, vol. 12, no. 106, p. 20150124, 2015.

[99] C. B. Lindemann and D. R. Mitchel, "Evidence for axonemal distortion during the flagellar beat of *Chlamydomonas*," *Cell Motility and the Cytoskeleton*, vol. 64, no. 8, pp. 580–589, 2007.

[100] R. E. Goldstein, M. Polin, and I. Tuval, "Emergence of synchronized beating during the regrowth of eukaryotic flagella," *Physical Review Letters*, vol. 107, no. 14, pp. 148103–148103, 2011.

[101] K. C. Leptos, K. Y. Wan, M. Polin, I. Tuval, A. I. Pesci, and R. E. Goldstein, "Antiphase synchronization in a flagellar-dominance mutant of *Chlamydomonas*," *Physical Review Letters*, vol. 111, no. 15, pp. 158101–158101, 2013.

[102] R. E. Goldstein, M. Polin, and I. Tuval, "Noise and synchronization in pairs of beating eukaryotic flagella," *Physical Review Letters*, vol. 103, no. 16, pp. 168103–168103, 2009.

[103] J. Kurths, A. Pikovsky, and M. Rosenblum, *Synchronization: a universal concept in nonlinear sciences*. Cambridge University Press New York, 2001.

[104] M. Uchida, K. Ishizaka, P. Hansmann, Y. Kaneko, Y. Ishida, X. Yang, R. Kumai, A. Toschi, Y. Onose, R. Arita, K. Held, O. K. Andersen, S. Shin, and Y. Tokura, "Pseudogap of metallic layered nickelate r2-xsrxnio4 (r = nd, eu) crystals measured using angle-resolved photoemission spectroscopy," *Physical Review Letters*, vol. 106, no. 2, pp. 027001–027001, 2011.

[105] J. Kotar, L. Debono, N. Bruot, S. Box, D. Phillips, S. Simpson, S. Hanna, and P. Cicuta, "Optimal hydrodynamic synchronization of colloidal rotors," *Physical Review Letters*, vol. 111, no. 22, pp. 228103–228103, 2013.

[106] D. R. Brumley, K. Y. Wan, M. Polin, and R. E. Goldstein, "Flagellar synchronization through direct hydrodynamic interactions," *Elife*, vol. 3, 2014.

[107] V. F. Geyer, F. Juelicher, J. Howard, and B. M. Friedrich, "Cell-body rocking is a dominant mechanism for flagellar synchronization in a swimming alga," *Proceedings of the National Academy of Sciences of the United States of America*, vol. 110, no. 45, pp. 18058–18063, 2013.

[108] K. Y. Wan and R. E. Goldstein, "Coordinated beating of algal flagella is mediated by basal coupling," *Proceedings of the National Academy of Sciences*, vol. 113, no. 20, 2016.

[109] P. Hegemann and B. Bruck, "Light-induced stop response in *Chlamydomonas reinhardtii* - occurrence and adaptation phenomena," *Cell Motility and the Cytoskeleton*, vol. 14, no. 4, pp. 501–515, 1989.

[110] D. Tam and A. E. Hosoi, "Optimal feeding and swimming gaits of biflagellated organisms," *Proceedings of the National Academy of Sciences of the United States of America*, vol. 108, no. 3, pp. 1001–1006, 2011.

[111] S. M. Shih, B. D. Engel, F. Kocabas, T. Bilyard, A. Gennerich, W. F. Marshall, and A. Yildiz, "Intraflagellar transport drives flagellar surface motility," *Elife*, vol. 2, pp. e00744–e00744, 2013.

[112] P. Collingridge, C. Brownlee, and G. L. Wheeler, "Compartmentalized calcium signaling in cilia regulates intraflagellar transport," *Current Biology*, vol. 23, no. 22, pp. 2311–2318, 2013.

[113] M. Garcia, S. Berti, P. Peyla, and S. Rafaï, "The random walk of a low-reynolds-number swimmer," 2010.

[114] T. Racey, R. Hallett, and B. Nickel, "A quasi-elastic light scattering and cinematographic investigation of motile chlamydomonas reinhardtii," *Biophysical journal*, vol. 35, no. 3, pp. 557–571, 1981.

[115] T. Racey and F. Hallett, "A low angle quasi-elastic light scattering investigation ofchlamydomonas reinhardtii," *Journal of muscle research and cell motility*, vol. 4, no. 3, pp. 321–331, 1983.

[116] N. A. Hill and D. P. Hader, "A biased random walk model for the trajectories of swimming micro-organisms," *Journal of Theoretical Biology*, vol. 186, no. 4, pp. 503–526, 1997.

[117] V. Vladimirov, P. Denissenko, T. Pedley, M. Wu, and I. Moskalev, "Algal motility measured by a laser-based tracking method," *Marine and freshwater research*, vol. 51, no. 6, pp. 589–600, 2000.

[118] V. A. Vladimirov, "Measurement of cell velocity distributions in populations of motile algae," *Journal of Experimental Biology*, vol. 207, no. 7, pp. 1203–1216, 2004.

[119] V. A. Martinez, R. Besseling, O. A. Croze, J. Tailleur, M. Reufer, J. Schwarz-Linek, L. G. Wilson, M. A. Bees, and W. C. K. Poon, "Differential dynamic microscopy: A high-throughput method for characterizing the motility of microorganisms," *Biophysical Journal*, vol. 103, no. 8, pp. 1637–1647, 2012.

[120] K. Drescher, K. C. Leptos, and R. E. Goldstein, "How to track protists in three dimensions," *Review of Scientific Instruments*, vol. 80, no. 1, p. 014301, 2009.

[121] H. C. Crenshaw, "Kinematics of helical motion of microorganisms capable of motion with 4-degrees of freedom," *Biophysical Journal*, vol. 56, no. 5, pp. 1029–1035, 1989.

[122] F. J. Sevilla and M. Sandoval, "Smoluchowski diffusion equation for active brownian swimmers," *Physical Review E*, vol. 91, no. 5, p. 052150, 2015.

[123] M. Polin, I. Tuval, K. Drescher, J. P. Gollub, and R. E. Goldstein, "*Chlamydomonas* swims with two "gears" in a eukaryotic version of run-and-tumble locomotion," *Science*, vol. 325, no. 5939, pp. 487–490, 2009.

[124] R. R. Bennett and R. Golestanian, "A steering mechanism for phototaxis in *Chlamydomonas*," *Journal of the Royal Society Interface*, vol. 12, no. 104, pp. 1742–5689, 2015.

[125] G. B. Witman, "Chlamydomonas phototaxis," *Trends in cell biology*, vol. 3, no. 11, pp. 403–408, 1993.

[126] E.-M. Holland, F.-J. Braun, C. Nonnengässer, H. Harz, and P. Hegemann, "The nature of rhodopsin-triggered photocurrents in chlamydomonas. i. kinetics and influence of divalent ions," *Biophysical journal*, vol. 70, no. 2, pp. 924–931, 1996.

[127] H. Harz and P. Hegemann, "Rhodopsin-regulated calcium currents in chlamydomonas," *Nature*, vol. 351, no. 6326, pp. 489–491, 1991.

[128] R. Kamiya and G. B. Witman, "Submicromolar levels of calcium control the balance of beating between the two flagella in demembranated models of chlamydomonas.," *The Journal of Cell Biology*, vol. 98, no. 1, pp. 97–107, 1984.

[129] J. Arrieta, A. Barreira, M. Chioccioli, M. Polin, and I. Tuval, "Phototaxis beyond turning: persistent accumulation and response acclimation of the microalga *chlamydomonas reinhardtii*," *Scientific Reports*, vol. 7, 2017.

[130] B. Bean, "Geotaxis in *Chlamydomonas*," *J. Cell. Biol.*, vol. 67, no. 24a, 1975.

[131] B. Bean, "Geotactic behaviour in *Chlamydomonas*," *J. Protozool.*, vol. 24, pp. 394–401, 1977.

[132] J. O. Kessler, "Hydrodynamic focusing of motile algal cells," *Nature*, vol. 313, no. 5999, pp. 218–220

[133] J. R. Platt, ""bioconvection patterns" in cultures of free-swimming organisms," *Science*, vol. 133, no. 3466, pp. 1766–1767 1961.

[134] N. Hill and T. Pedley, "Bioconvection," *Fluid Dynamics Research*, vol. 37, no. 1, pp. 1–20

[135] M. L. S. Childress and E. A. Spiegel, "Pattern formation in a suspension of swimming microorganisms: equations and stability theory," *J Fluid Mech.*, vol. 69, no. 03, pp. 591–613, 1975.

[136] T. J. Pedley and J. O. Kessler, "A new continuum model for suspensions of gyrotactic micro-organisms," vol. 212, pp. 155–182, 1990.

[137] T. J. Pedley, N. A. Hill, and J. O. Kessler, "The growth of bioconvection patterns in a uniform suspension of gyrotactic micro-organisms," vol. 195, pp. 223–237, 1988.

[138] R. Sjoblad and P. H. Frederikse, "Chemotactic responses of *Chlamydomonas reinhardtii.*," *Molecular and cellular biology*, vol. 1, no. 12, pp. 1057–1060

[139] E. Govorunova and O. Sineshchekov, "Chemotaxis in the green flagellate alga chlamydomonas," *Biochemistry (Moscow)*, vol. 70, no. 7, pp. 717–725 0006–2979, 2005.

[140] H. I. Choi, J. Y. H. Kim, H. S. Kwak, Y. J. Sung, and S. J. Sim, "Quantitative analysis of the chemotaxis of a green alga, *Chlamydomonas reinhardtii*, to bicarbonate using diffusion-based microfluidic device," *Biomicrofluidics*, vol. 10, no. 1, pp. 1932–1058, 2016.

[141] E. V. Ermilova, Z. M. Zalutskaya, T. V. Lapina, and M. M. Nikitin, "Chemotactic behavior of *Chlamydomonas reinhardtii* is altered during gametogenesis," *Current microbiology*, vol. 46, no. 4, pp. 0261–0264

[142] N. Heddergott, T. Krüger, S. B. Babu, A. Wei, E. Stellamanns, S. Uppaluri, T. Pfohl, H. Stark, and M. Engstler, "Trypanosome motion represents an adaptation to the crowded environment of the vertebrate bloodstream," *PLOS Pathogens*, vol. 8, no. 11, pp. e1003023–, 2012.

[143] P. Denissenko, V. Kantsler, D. J. Smith, and J. Kirkman-Brown, "Human spermatozoa migration in microchannels reveals boundary-following navigation," *Proceedings of the National Academy of Sciences*, vol. 109, no. 21, pp. 8007–8010, 2012.

[144] A. P. Berke, L. Turner, H. C. Berg, and E. Lauga, "Hydrodynamic attraction of swimming microorganisms by surfaces," *Physical Review Letters*, vol. 101, no. 3, 2008.

[145] G. Li and J. X. Tang, "Accumulation of microswimmers near a surface mediated by collision and rotational brownian motion," *Physical Review Letters*, vol. 103, no. 7, pp. 078101–078101, 2009.

[146] D. L. Valentine, J. D. Kessler, M. C. Redmond, S. D. Mendes, M. B. Heintz, C. Farwell, L. Hu, F. S. Kinnaman, S. Yvon-Lewis, M. Du, E. W. Chan, F. G. Tigreros, and C. J. Villanueva, "Propane respiration jump-starts microbial response to a deep oil spill," *Science*, vol. 330, no. 6001, p. 208, 2010.

[147] J. D. Kessler, D. L. Valentine, M. C. Redmond, M. Du, E. W. Chan, S. D. Mendes, E. W. Quiroz, C. J. Villanueva, S. S. Shusta, L. M. Werra, S. A. Yvon-Lewis, and T. C. Weber, "A persistent oxygen anomaly reveals the fate of spilled methane in the deep gulf of mexico," *Science*, vol. 331, no. 6015, p. 312, 2011.

[148] P. Merviel, M. H. Heraud, N. Grenier, E. Lourdel, P. Sanguinet, and H. Copin, "Predictive factors for pregnancy after intrauterine insemination (iui): An analysis of 1038 cycles and a review of the literature," *Fertility and Sterility*, vol. 93, no. 1, pp. 79–88, 2017.

[149] D. B. Weibel, P. Garstecki, D. Ryan, W. R. DiLuzio, M. Mayer, J. E. Seto, and G. M. Whitesides, "Microoxen: Microorganisms to move microscale loads," *Proceedings of the National Academy of Sciences of the United States of America*, vol. 102, no. 34, pp. 11963–11967, 2005.

[150] A. T. Brown, I. D. Vladescu, A. Dawson, T. Vissers, J. Schwarz-Linek, J. S. Lintuvuori, and W. C. K. Poon, "Swimming in a crystal," *Soft Matter*, vol. 12, no. 1, pp. 131–140, 2016.

[151] P. D. Frymier, R. M. Ford, H. C. Berg, and P. T. Cummings, "Three-dimensional tracking of motile bacteria near a solid planar surface," *Proceedings of the National Academy of Sciences*, vol. 92, no. 13, pp. 6195–6199, 1995.

[152] M. Molaei, M. Barry, R. Stocker, and J. Sheng, "Failed escape: Solid surfaces prevent tumbling of escherichia coli," *Physical Review Letters*, vol. 113, no. 6, pp. 068103–068103, 2014.

[153] O. Sipos, K. Nagy, R. Di Leonardo, and P. Galajda, "Hydrodynamic trapping of swimming bacteria by convex walls," *Physical Review Letters*, vol. 114, no. 25, pp. 258104–258104, 2015.

[154] R. E. Goldstein, "Green algae as model organisms for biological fluid dynamics," *Annual Review of Fluid Mechanics, Vol 47*, vol. 47, pp. 343–375, 2015.

[155] V. Pelletier, N. Gal, P. Fournier, and M. L. Kilfoil, "Microrheology of microtubule solutions and actin-microtubule composite networks," *Physical Review Letters*, vol. 102, no. 18, pp. 188303–, 2009.

[156] C.-C. Hsieh, S. Jain, and R. G. Larson, "Brownian dynamics simulations with stiff finitely extensible nonlinear elastic-fraenkel springs as approximations to rods in bead-rod models," *The Journal of chemical physics*, vol. 124, no. 4, p. 044911, 2006.

[157] E. Lushi, V. Kantsler, and R. E. Goldstein, "Scattering of bi-flagellate microswimmers from surfaces," *arXiv preprint arXiv:1608.02551*, 2016.

[158] J. Elgeti and G. Gompper, "Wall accumulation of self-propelled spheres," *EPL (Europhysics Letters)*, vol. 101, no. 4, p. 48003, 2013.

[159] S. Kim and S. Karrilla, *Microhydrodynamics: Principles and selected applications*. Dover, Boston, 1991.

[160] O. Felfoul, M. Mohammadi, S. Taherkhani, D. de Lanauze, Y. Zhong Xu, D. Loghin, S. Essa, S. Jancik, D. Houle, M. Lafleur, L. Gaboury, M. Tabrizian, N. Kaou, M. Atkin, T. Vuong, G. Batist, N. Beauchemin, D. Radzioch, and S. Martel, "Magneto-aerotactic bacteria deliver drug-containing nanoliposomes to tumour hypoxic regions," *Nat Nano*, vol. 11, no. 11, pp. 941–947, 2016.

[161] J. Li, B. Esteban-Fernández de Ávila, W. Gao, L. Zhang, and J. Wang, "Micro/nanorobots for biomedicine: Delivery, surgery, sensing, and detoxification," *Sci. Robotics*, vol. 2, no. 4, 2017.

[162] J.-M. Bollag, T. Mertz, and L. Otjen, "Role of microorganisms in soil bioremediation," *Bioremediation through Rhizosphere Technology*, vol. 563, pp. 2–10, 1994.

[163] T. A. Anderson and J. R. Coats, *Bioremediation through Rhizosphere Technology*, vol. 563. American Chemical Society, 1994.

[164] T. J. Ober, D. Foresti, and J. A. Lewis, "Active mixing of complex fluids at the microscale," *Proceedings of the National Academy of Sciences*, vol. 112, no. 40, pp. 12293–12298, 2015.

[165] P. Mueller and J.-L. Thiffeault, "Fluid transport and mixing by an unsteady microswimmer," *Phys. Rev. Fluids*, vol. 2, no. 1, p. 013103, 2017.

[166] E. A. Codling, M. J. Plank, and S. Benhamou, "Random walk models in biology," *Journal of the Royal Society Interface*, vol. 5, no. 25, pp. 813–834, 2008.

[167] G. Jékely, "Evolution of phototaxis," *Philos Trans R Soc Lond B Biol Sci*, vol. 364, no. 1531, p. 2795, 2009.

[168] D. Takagi, J. Palacci, A. B. Braunschweig, M. J. Shelley, and J. Zhang, "Hydrodynamic capture of microswimmers into sphere-bound orbits," *Soft Matter*, vol. 10, no. 11, pp. 1784–1789, 2014.

[169] S. E. Spagnolie, G. R. Moreno-Flores, D. Bartolo, and E. Lauga, "Geometric capture and escape of a microswimmer colliding with an obstacle," *Soft Matter*, vol. 11, no. 17, pp. 3396–3411, 2015.

[170] M. Mijalkov and G. Volpe, "Sorting of chiral microswimmers," *Soft Matter*, vol. 9, no. 28, pp. 6376–6381, 2013.

[171] S. E. Spagnolie, C. Wahl, J. Lukasik, and J.-L. Thiffeault, "Microorganism billiards," *Physica D: Nonlinear Phenomena*, vol. 341, pp. 33–44, 2017.

[172] M. Khatami, K. Wolff, O. Pohl, M. R. Ejtehadi, and H. Stark, "Active brownian particles and run-and-tumble particles separate inside a maze," *Scientific Reports*, vol. 6, no. 1, 2016.

[173] J. P. Hernandez-Ortiz, C. G. Stoltz, and M. D. Graham, "Transport and collective dynamics in suspensions of confined swimming particles," *Physical Review Letters*, vol. 95, no. 20, 2005.

[174] T. Ostapenko, F. J. Schwarzendahl, T. Böddeker, C. T. Kreis, J. Cammann, M. G. Mazza, and O. Bäumchen, "Curvature-guided motility of microalgae in geometric confinement," 2016.

[175] Z. Schuss, "The narrow escape problemtextemdasha short review of recent results," *Journal of Scientific Computing*, vol. 53, no. 1, pp. 194–210, 2012.

[176] J. W. S. Baron Rayleigh, *The theory of sound vol. 2.* Dover, New York, 1945.

[177] A. Singer, Z. Schuss, and D. Holcman, "Narrow escape, part ii: The circular disk," *Journal of Statistical Physics*, vol. 122, no. 3, pp. 465–489, 2006.

[178] E. G. Altmann, J. S. Portela, and T. Tél, "Leaking chaotic systems," *Reviews of Modern Physics*, vol. 85, no. 2, p. 869, 2013.

[179] W. C. Sabine and C. H. Dwight, "Collected papers on acoustics," *American Journal of Physics*, vol. 34, no. 4, pp. 370–371, 1966.

[180] W. B. Joyce, "Sabine's reverberation time and ergodic auditoriums," *The Journal of the Acoustical Society of America*, vol. 58, no. 3, pp. 643–655, 1975.

[181] O. G. Berg, R. B. Winter, and P. H. V. Hippel, "Diffusion-driven mechanisms of protein translocation on nucleic acids. 1. models and theory," *Biochemistry*, vol. 20, no. 24, pp. 6929–6948, 1981.

[182] K. M. Harris and J. K. Stevens, "Dendritic spines of rat cerebellar purkinje cells: serial electron microscopy with reference to their biophysical characteristics," *Journal of Neuroscience*, vol. 8, no. 12, pp. 4455–4469, 1988.

[183] D. Holcman, E. Korkotian, and M. Segal, "Calcium dynamics in dendritic spines, modeling and experiments," *Cell Calcium*, vol. 37, no. 5, pp. 467–475, 2005.

[184] Y. Chávez, M.-V. Vázquez, and L. Dagdug, "Unbiased diffusion through a linear porous media with periodic entropy barriers: a tube formed by contacting ellipses," *Journal of Chemistry*, vol. 2015, 2015.

[185] M. S. Krieger, "Microorganism billiards in closed plane curves," *ArXiv e-prints*, 2016.